Ville Pale

# Improving the optical properties of chlorophyll aggregates with supramolecular design.

**School of Electrical Engineering**

Thesis submitted for examination for the degree of Master of Science in Technology.

Espoo 12.9.2011

**Thesis supervisor:**

Prof. Ilkka Tittonen

**Thesis instructor:**

Dr Juho Helaja

Aalto University
School of Electrical
Engineering

AALTO UNIVERSITY
SCHOOL OF ELECTRICAL ENGINEERING

ABSTRACT OF THE
MASTER'S THESIS

Author: Ville Pale

Title: Improving the optical properties of chlorophyll aggregates with supramolecular design.

Date: 12.9.2011 Language: English Number of pages:10+70

Department of Micro- and Nanosciences

Professorship: Physics of micro technologies Code: S-129

Supervisor: Prof. Ilkka Tittonen

Instructor: Dr Juho Helaja

Chlorophyll molecules are the most efficient light-harvesting pigments found in nature. They also exhibit a remarkable ability to transfer the excitation energy to another chlorophyll molecule with a 90 % efficiency. In addition, they possess a very good fluorescence quantum yield opening a possibility as new optical materials.

To utilize this property could lead to new novel photonic materials or devices, *e.g.*, in energy harvesting or sensor applications. However, for most applications this requires integration of the chromophores into the semiconductor materials. Hence, a method to passivate and functionalize GaAs surface has been developed. Also, another goal of this thesis has been to find the optimal supramolecular architechture to improve the fluorescence of the chlorophylls.

The literature part is divided into three major parts. The first part contains information about the excitation dynamics of molecules. The second part is dedicated to explain the optical, chemical and aggregation properties of chlorophylls arising directly from the structural properties of these molecules. The third part investigates the resonance energy transfer, an important intermolecular interaction mechanisms present, *e.g.*, in plants, photosynthetic bacteria and conductive polymers.

The experimental part is divided into the two parts. First, a method to passivate and functionalize GaAs surface using thiol monolayer is investigated with continous wave and time-resolved photoluminescence spectroscopy. Second, the fluorescence between two different polymer-dye complexes and pure chlorophyll aggregates is studied. These samples are cast on a glass substrate using spin coating and the resulting films of are characterized by Uv-Vis absorption and fluorescence spectroscopy.

Keywords: gallium arsenide, chlorophyll, polymer-dye complexes, aggregate, FRET, photoluminescence, fluorescence

AALTO-YLIOPISTO
SÄHKÖTEKNIIKAN KORKEAKOULU

DIPLOMITYÖN
TIIVISTELMÄ

Tekijä: Ville Pale

Työn nimi: Klorofylliaggregaattien optisten ominaisuuksien parantaminen supramolekyläärisen suunnittelun avulla.

Päivämäärä: 12.9.2011 Kieli: Englanti Sivumäärä:10+70

Mikro- ja nanotekniikan laitos

Professuuri: Sähköfysiikka Koodi: S-129

Valvoja: Prof. Ilkka Tittonen

Ohjaaja: FT Juho Helaja

Klorofyllimolekyylit (lehtivihreä) ovat tehokkaimpia valoa keräämiä pigmenttejä, mitä luonnosta on löydetty. Niillä on myös uskomaton kyky siirtää viritysenergia toiseen klorofyllimolekyyliin jopa 90 % hyötysuhteella. Lisäksi niillä on erittäin hyvä fluoresenssin kvanttisaanto mahdollistaen niiden käytön uusissa optisissa materiaaleissa.
Tämän evoluution muovaaman ilmiön hyödyntäminen voi johtaa uusiin mullistaviin fotoniikan materiaaleihin tai laitesovelluksiin, kuten energian tuottamiseen tai sensorisovelluksiin. Ennen tätä pigmentit täytyy kuitenkin pystyä integroimaan puolijohdemateriaaleihin. Tästä johtuen työssä on kehitetty menetelmä GaAs pinnan passivoimiseksi ja funktionalisoimiseksi. Työn toisena tavoitteena on ollut optimoida klorofyllien fluoresenssia supramolekyläärisen arkkitehtuurin avulla.
Kirjallisuusosuus on jaettu kolmeen osaan. Ensimmäinen osa sisältää tietoa molekyylien viritysdynamiikasta. Toinen osa on omistettu klorofyllien optisten, kemiallisten ja aggregointi ominaisuuksien selittämiseen, jotka voidaan suoraan päätellä molekyylien rakenteen avulla. Viimeisessä osassa tutkitaan resonoivaa energiasiirtoa, joka on erittäin tärkeä molekyylien välinen vuorovaikutusmekanismi, joka on läsnä esimerkiksi kasveissa, yhteyttävissä bakteereissa ja johtavissa muoveissa.
Kokeellinen osuus on jaettu kahteen osaan. Ensimmäisessä osassa GaAs pinnan passivointiin ja funktionalisointiin käytetään tioliyhdisteitä. Syntynyttä atomikerroksen paksuisen päällysteen ominaisuuksia karakterisoidaan taajuus ja aikatasossa fotoluminesenssin avulla. Toisessa osassa tutkitaan fluoresenssin tehokkuutta kahden polymeeri-pigmentti kompleksin ja klorofylli aggregaattin välillä. Näytteet valmistetaan lasisubstraateille “spin coating”-menetelmän avulla ja karakterisoidaan Uv-Vis absorption ja fluoresenssispektroskopian avulla.

Avainsanat: galliumarsenidi, lehtivihreä, polymeeri-väriaine kompleksi, aggregaatti, FRET, fotoluminesenssi, fluoresenssi

# Preface

First, I want to thank Professor Ilkka Tittonen for his patience and offering me the possibility to work with this interesting subject. I would also want to express my gratitude for Ph.D. Juho Helaja and M.Sc. Taru Nikkonen from the University of Helsinki for the preparation of the samples and with the help concerning the chemistry of chlorophylls. My gratitude goes also to Päivi and Marco Mattila for their assistance with the photoluminescence measurements and help in general. In addition, I would like to thank Arri Priimagi for his help with the UV-Vis setup and the discussions concerning supramolecular chemistry and Jaana Vapaavuori for the help with fluorometric setup and teaching me to fabricate to the dye-polymer complexes.

Special thanks go for Ossi Kimmelma, Osmo Vänskä, Nikolai Chekurov, Mikhail Erdmanis and Mikko Ruoho for interesting discussions not to forget the rest of MQS personnel. Thanks go also for Alexander Kravchenko for keeping the working days interesting and refreshing. Furthermore, I thank my pupil, Jorma Selin, who I had the privilege to mentor. Your endless curiosity and questions gave me new ideas concerning this project. Also, I appreciate your help with the measurements during the summer.

Also I would like to thank my all my friends and especially Stigu, since you are probably one of the few people who has really read this thesis from front to cover. Finally, I would like to offer my biggest thanks for my dear family; Elina, Sofie, Jasmiini, Mom, Dad, Jyri and Granny for giving all this work a meaning.

Otaniemi, 19.8.2011

Ville Pale

# Contents

# Symbols and abbreviations

## Symbols

| | |
|---|---|
| $A$ | Acceptor |
| $A^*$ | Acceptor in excited state |
| $a_0$ | Bohr radius [m] |
| $a_{(1/2)u}$ | HOMO in Gouterman's four orbital model |
| $c$ | Speed of light in medium $c_0/n \approx 3 \cdot 10^8/n$ [m/s] |
| $D$ | Donor |
| $D^*$ | Donor in excited state |
| $E$ | Excitonic splitting term / Efficiency of the energy transfer |
| $e_{g(x/y)}$ | LUMO in Gouterman's four orbital model |
| $E_n$ | Energy of the n:th state |
| $E_0$ | Energy of the ground state |
| $f$ | Frequency [$s^{-1}$] |
| $F_D$ | Fluorescence intensity from a sample containing only donor |
| $F_{DA}$ | Fluorescence intensity from a sample containing donor and acceptor |
| $f_{\mathrm{OS}}$ | Oscillator strenght |
| $h$ | Planck's constant $\approx 4.135 \cdot 10^{-15}$ [eVs] |
| $\hbar$ | Reduced Planck's constant $h/2\pi \approx 6.582 \cdot 10^{-16}$ [eVs] |
| $J_{DA}$ | Overlap integral |
| $\mathbf{k}$ | Wave vector |
| $k_{\mathrm{F}}$ | Fluorescence rate constant |
| $k_{\mathrm{IC}}$ | Internal conversion rate constant |
| $k_{\mathrm{ISC}}$ | Intersystem crossing rate constant |
| $k_{\mathrm{P}}$ | Phosphorescence rate constant |
| $k_{\mathrm{RET}}$ | FRET rate constant |
| $n$ | Refractive index |
| $N_A$ | Avogadro constant $\approx 6.022 \cdot 10^{23}$ [$mol^{-1}$] |
| $\mathbf{R}$ | Distance vector between donor and acceptor |
| $R$ | Distance between donor and acceptor |
| $\mathbf{r}$ | Center-to-center position vector between two paraller molecules |
| $r$ | Center-to-center distance between two paraller molecules |
| $\mathbf{r}_{a_{(1/2)u}e_{g(x/y)}}$ | The transition dipole moment of the single-configuration transition |
| $\mathbf{r}_{B_{(x/y)}}$, $\mathbf{r}_{Q_{(x/y)}}$ | The spectrocopically observable transition dipole moments |
| $R_0$ | Förster length |
| $S_n$ | N:th electronic singlet state |
| $T_n$ | N:th electronic triplet state |
| $V$ | Quantization volume |
| $v$ | Vibrational quantum number |
| $\Delta E$ | Excitonic band splitting term |
| $\epsilon_A$ | Molar absorption coefficient of acceptor |
| $\epsilon_0$ | Vacuum permittivity $\approx 8.854 \cdot 10^{-12}$ [F/m] |

| | |
|---|---|
| $\theta$ | Inclination angle between two paraller transition dipole moments |
| $\lambda$ | Wavelength [m] |
| $\lambda\!\!\!^{-}$ | Reduced wavelength $\lambda/2\pi$ [m] |
| $\kappa$ | Förster orientation factor |
| $\boldsymbol{\mu}$ | Transition dipole moment vector |
| $\pi$ | Ground state of the $\pi$-orbital |
| $\pi^*$ | Excited state of the $\pi$-orbital |
| $\sigma$ | Absorption cross-section |
| $\tau_B$ | Bulk recombination lifetime |
| $\tau_{eff}$ | Effective lifetime of the minority carriers |
| $\tau_F$ | Surface recombination lifetime |
| $\tau_S$ | Effective lifetime of the minority carriers |
| $\Phi_{a_{(1/2)u}e_{g(x/y)}}$ | Single-configuration excitations in Gouterman's four orbital model |
| $\phi_D$ | Quantum yield of donor |
| $\phi_F$ | Fluorescence quantum yield |
| $\Psi_{B(x/y)}$, $\Psi_{Q(x/y)}$ | Spectrocopically observable excited states |

## Operators

| | |
|---|---|
| $\hat{a}_{\mathbf{k},\lambda}$ | Annihilation operator |
| $H_{\text{bath}}$ | Bath Hamiltonian |
| $\hat{a}^{\dagger}_{\mathbf{k},\lambda}$ | Creation operator |
| $\hat{\mu}$ | Electric dipole operator / Dipole moment operator |
| $\hat{d}_{\perp}$ | Displacement operator |
| $H$ | Hamiltonian operator |
| $H_{\text{int}}$ | Hamiltonian operator for the Coulumb interaction |
| $H_{\text{rad}}$ | Hamiltonian operator for the quantized radiation field |
| $H_{\text{mol}}$ | Molecular Hamiltonian operator |
| $\hat{e}_{\mathbf{k},\lambda}$ | Polarization operator |

## Abbreviations

| | |
|---|---|
| Abs | Absorption |
| ATP | Adenosine triphosphate |
| BChl | Bacteriochlorophyll |
| BIBO | Bismuth tribonate |
| Ca | Calcium |
| Car | Carotenoid |
| Chl | Chlorophyll |
| CWPL | Continuous-wave photoluminescence spectroscopy |
| CI | Configuration interaction |
| DCM | Dichloromethane |
| DFB | Distributed feedback |
| DSC | Dye-sensitized solar cell |
| Farn | Farnesyl |
| F | Fluorescence |
| FRET | Förster / Fluorescent resonant energy transfer |
| GaAs | Gallium arsenide |
| HOMO | Highest occupied molecular orbital |
| IC | Internal conversion |
| ISC | Intersystem crossing |
| IUPAC | International union of pure and applied chemistry |
| LED | Light-emitting diode |
| Li | Lithium |
| LUMO | Lowest unoccupied molecular orbital |
| K | Potassium |
| MS | Mass spectrometry |
| Na | Sodium |
| Nd:$YVO_4$ | Neodymium:Yttrium vanadate |
| NIR | Near-infrared |
| NR | Non-radiative |
| NMR | Nuclear magnetic resonance |
| Mg | Magnesium |
| PS | Photosystem |
| PDT | Photodynamic therapy |
| PMMA | Poly(methyl methacrylate) |
| Pyro a | Zn-methyl-*pyro*-pheophorbide *a* |
| P4VP | Poly(4-vinylpyridine) |
| OH-Pyro a | Zn-31-OH-methyl-*pyro*-pheophorbide *a* |
| OLED | Organic light-Emitting diode |
| Pheo | Pheophorbide |
| Phy | Phytyl |
| P | Phosphorescence |
| PL | Photoluminescence |

| | |
|---|---|
| RC | Reaction center |
| RET | Resonance energy transfer |
| ROS | Reactive oxygen species |
| THF | Tetrahydrofuran |
| TRPL | Time resolved photoluminesce spectroscopy |
| QD | Quantum dot |
| QED | Quantum electrodynamics |
| QW | Quantum well |
| SNOM | Scanning near-field optical microscope |
| STM | Scannning tunneling microscope |
| Uv-Vis | Ultraviolet-visible |
| VR | Vibrational relaxation |
| XPS | Photoelectron spectroscopy |
| Zn | Zinc |

# 1 Introduction

> "*Man cannot give a true reason for the grass under his feet why it should be green rather than red or any other color.*"
>
> Sir Walter Raleigh
> History of the world: Preface (1614)

The study of chlorophylls has attracted the attention of many bright scientists in the past. In 1844, F. Verdeil was the first person to suggest a relationship between green chlorophyll and red blood pigment, haem, which was known to contain iron. Shortly after this in 1880, Felix Hoppe-Seyler gave additional proof to this hypothesis by showing spectral resemblances between hematoporphyrin and an acid degration product of chlorophyll. After the work of Verdeil and Hoppe-Seyler, it was suggested that chlorophylls also contained iron. However, this erroneous belief was corrected by Richard Willstätter in 1913, who identified chlorophylls as water insoluble magnesium compound with ester groups of methyl and phytyl alcohol. In 1915, Richard Willstätter received a Nobel prize in chemistry "*for his researches on plant pigments, especially chlorophyll*". The final steps in the structural elucidations of chlorophyll molecules culminated in the work of Hans Fischer who showed that for two hydrogen atoms red would be green and only two more hydrogen atoms would have ensured blood to be blue. In 1930, Hans Fischer also received a Nobel prize in chemistry "*for his researches into the constitution of haemin and chlorophyll and especially for his synthesis of haemin*".

The structural similarity of heme (iron-porphyrin) and chlorophyll (Mg-phytochlorin) is not a coincidence. Through the evolutionary process, plants have utilized chlorophyll molecules in converting and storing the Sun's solar energy into chemical energy. Also for many organisms, the means by which oxygen is transported, stored, reduced and activated are mediated by the heme proteins. [1] Consequently, porphyrins and chlorins are the central molecules on this planet to which all lifeforms directly rely on.

Photosynthetic process is one of the vital processes that sustains life on earth. The process transforms carbon dioxide ($CO_2$) to sugars with the help of energy from the Sun. Organisms on earth that are capable of performing photosynthesis are plants, algae and some bacteria. [2] Sunlight on earth's surface has it's intensity maximum around the visible wavelengths (380-750 nm) of the electromagnetic spectrum. Also a significant contribution of radiation exists in the near infrared area (750-1000 nm) [3, 4]. To utilize this usable spectral band, the photosynthesizing organisms have developed a wide range of different light absorbing pigments. These pigments in plants are chlorophylls (Chl), carotenoids and bacteriochlorophylls (BChl) in bacteria. Naturally, earth contains a diverse collection of different chromophores and the aforementioned pigments cover only a small part from the total amount.

Chlorophyll molecules are the most sensitive and efficient light-capturing pigments found from nature. They perform the three important functions in photosynthetic process. First, they act as light-harvesting antennas that harvest light extremely

efficiently. Secondly, they transfer the excitation energy to the reaction center (RC) with high quantum efficiency via resonance energy transfer (RET), which is going to be discussed in more detail in Chapter 4. Third, they participate in the charge separation across photosynthetic membrane in the reaction center. [2]

In plants Chl molecules have a strong absorption in blue and yellow wavelengths, hence giving the green colour for the plant. Because of this distinct feature, the molecules have inherited their name from Greek words (*chloros* "green") and (*phyllos* "leaf"). However, bacteriochlorophylls (BChl) have a different colour than Chl, because they partially hydrogenated pyrrole rings that shift absorption to the near infrared region. Typically, plants and algae have two different chlorophyll molecules participating in the photosynthetic process; Chl *a* and Chl *b*. Chl *a* is found in the reaction centers and core antennas. On the other hand, Chl *b* is only found in outer antennas. Since Chl *b* has different absorption maxima from Chl *a*, it broadens the available spectral bandwidth for photosynthesis.

One of the promising applications that bears a striking similarity with the photosynthetic process is the Grätzel solar cell also called Dye-sensitized solar cell (DSC), which was published in Nature 1991 [5]. The inventors of DSC are Professor Michael Grätzel and Brian O'Regan. This invention also brought Prof. Grätzel the Millenium prize in 2010. The similarities of DSC with the plants lies in the manner, which the energy is created and also in the fact that both are able to create energy even without direct sunlight in cloudy conditions.

In addition to photosynthetic process and chlorophylls, another interesting aspect, which is not directly related to this thesis, but necessary concerning the future work with this subject lies in the realm of semiconductors. Quantum heterostructures (QHS) are artificially created semiconductor structures, which include Quantum Wells (QW), Quantum Wires and Quantum Dots (QD). The small size of these structures gives rise to quantum confinement leading to the formation of discrete energy levels that the charge carries can populate. More specifically, the quantum confinement decreases the density of states in these structures. Therefore, these structures behave more like atoms or molecules, but can still have a size much larger compared to atomic dimensions. QHS are especially important for optoelectronic devices, where they are used in the fabrication of short wavelength light-emitting diodes (LED), diode laser and high-efficiency solar cells. [6]

Devices that utilize RET and are composed of biological and inorganic semiconductor quantum heterostructures have been created previously. Usually these devices are formed of colloidal QDs instead of planar structures [7], but planar devices also exists [8]. Nonetheless, the research in this field is rich ranging from theoretical to applied approaches.

The first aim of this thesis is to develop a method to passivate and functionalize a semiconductor surface, which in this case is GaAs. Passivation is critical for the performance of the QHS device improving the long-term stability of the device and the quantum confinement of the QHS. With a stronger quantum confinement, the thickness of the barrier layer situated between the organic layer and the QHS can

be decreased, which in turn increases the coupling. In addition, it provides a selectively sensitized surface for the chlorophyll pigments. Secondly, to monitor the coupling and energy transfer from the organic layer to the inorganic matrix, a signal needs to be generated. The easiest way to achieve this goal is by spectroscopic measurements, and hence the organic layer is optimized to fluoresce. For this purpose, the fluorescence of PMMA-Chl, P4VP-Chl complexes and pure Chl aggregates are compared with each other to find the optimal configuration. The samples are spin coated on a glass substrates and characterized by different spectroscopic methods, *e.g.*, UV-Vis absorption, continous wave and time-resolved photoluminescence and fluorescence spectoscopy.

The structure of the thesis is following: Chapter 2 provides the basic aspects related to excitation dynamics of molecules that are required later on this thesis. Chapter 3 is devoted for the properties of different chlorophyll molecules. The most important content lies in the optical properties and the aggregation of chlorophylls. Chapter 4 presents the principles needed to undestand the phenomena called Resonance Energy Transfer (RET). Also in this chapter a unified theory of RET is presented. Chapters 5 and 6 will be covering the experimental techniques and preparation of samples. Finally, the last two chapters present the results and the conclusions.

# 2 Light induced processes in molecules

This Chapter presents some important details and aspects involved in the interactions between light and molecules. Also the influences of the molecular environments to the excited state dynamics of molecules will be discussed.

Figure 2.2 shows a simplified Jablonski diagram of a fluorescent molecule. In the diagram various energy states of the molecule are presented. Also the different transitions related to the formation and relaxation of the excited states are shown. The electronic states are marked with letter $S$ and $T$, where they stand for "singlet" and "triplet". In a singlet state, all the spins are paired and the spin multiplicity of the system is zero. In a triplet state, the system has a spin multiplicity of one. This kind of system can be achieved if one of the pairs becomes unpaired. [9] Figure 2.1 shows examples with singlet and triplet configurations. In isolated molecules, a

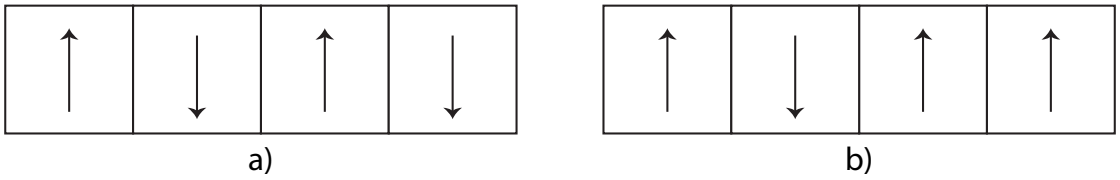


Figure 2.1: A system consisting of (a) four paired electrons (b) two paired electrons and two unpaired electrons.

triplet state is generally lower in energy than the singlet state of the same configuration. This is because the unpaired electrons are farther apart according to Pauli exclusion principle, which results in lower repulsion energy.

The electronic state $S_0$ is the ground state of the molecule and while the others $(S_1, S_2, T_1, T_2)$ are excited states. The electronic states contain also vibrational or rotational sublevels. Hence, in the diagram the energy levels consist of bands and not single lines. The vibrational substates are denoted by the vibrational quantum numbers $v = 0, 1, 2, 3 \ldots$ (with increasing energy). The rotational sublevels are very small in magnitude and therefore only appear as a broadening of the vibrational sublevels. [10]

At room temperature a molecule can be approximated to populate the lowest vibrational level of the ground state $S_0$. A photon, with frequency $f$, can be absorbed by the molecule, only if the photon energy is exactly equal to the energy difference of the ground and excited state as in

$$hf = E_n - E_0\,, \tag{2.1}$$

where $E_n$ and $E_0$ denote energy of the excited and the ground state. Absorption of a photon produces a rapid excitation from the ground singlet state $S_0$ to an excited

state $S_n$ that changes the electronic structure of the molecule. The time scale of this transformation is $10^{-15}$ s. Since the atomic nuclei vibrate on a time scale of $10^{-12}$ s, their positions are unaffected by the absorption. As shown in Fig. 2.2, the molecule can absorb photons with a range of different wavelengths resultig from the vibrational sublevels. This causes broadening of the peaks in the absorption spectra.

After the absorption of a photon, two different things can happen depending on the environment of the molecule. In dilute media, the only way for a molecule to lose vibrational energy is to emit an infrared photon. However, this event has a lesser probability compared to direct $S_n \rightarrow S_0$ transition. Hence, one tends to see emissions from the higher vibrational states in dilute media spectra. In condensed media, the situation is different. The excess vibrational energy can relax very efficiently by a rapid decay (time scale $10^{-12}$ s) to the lowest vibrational level of the excited electronic state. Therefore, in a condensed media the excited species will always undergo vibrational relaxation, before any other relaxation process. [11]

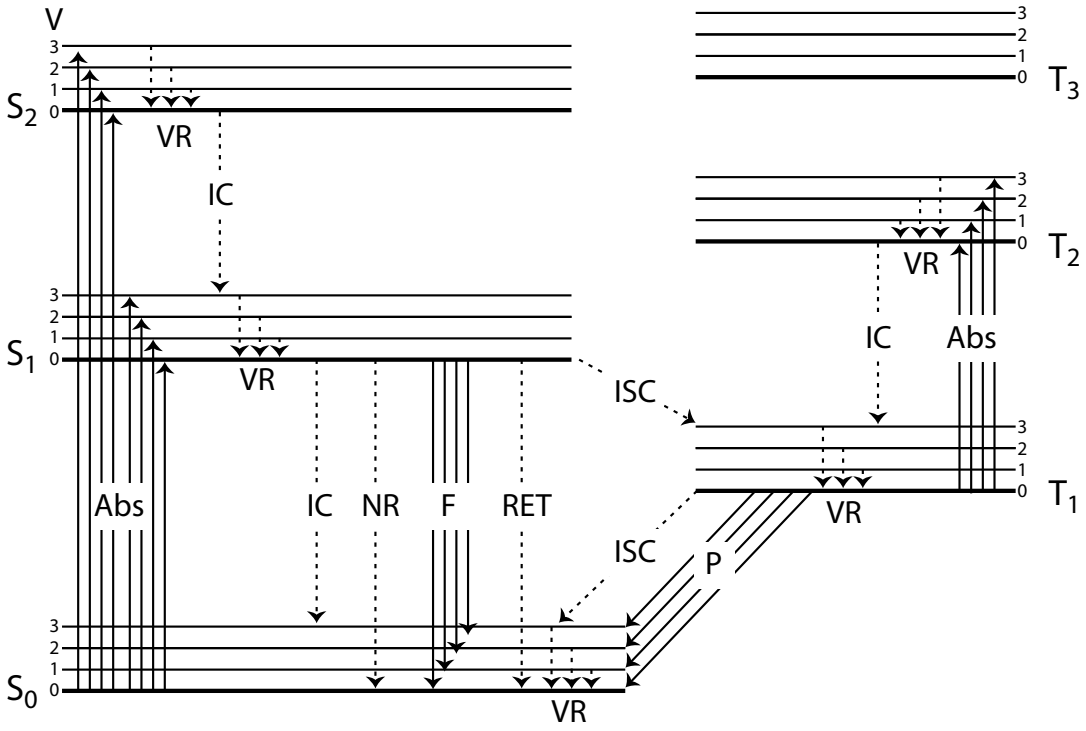


Figure 2.2: The electronic transitions involved in the excitation of a fluorophore in condensed media and pathways by which energy can be lost. Abbreviations: Abs: absorption, VR: vibrational relaxation, IC: internal conversion, F: fluorescence, RET: resonance energy transfer, NR: non-radiative, ISC: intersystem crossing, P: phosphorescence. Solid lines correspond to radiative transitions and dashed lines correspond to non-radiative transitions.

From this point on, the fluorophore can return to the ground state with several potential ways, which are characterized by the rate constants ($k$). These can be

divided roughly to two different distinct cases: intramolecular and intermolecular deactivation.

The intramolecular deactivation processes include radiative and non-radiative transitions. When the molecule returns from the lowest vibrational level of the excited state $S_n$ to the ground state $S_0$ by emitting a photon, it is called fluorescence ($k_{\mathrm{F}}$). When this transition occurs from the triplet state $T_n$ to the singlet ground state $S_0$ it is referred to as phosphorescence ($k_{\mathrm{P}}$). The lifetime of an excited singlet state is roughly $10^{-9}$ s, which also corresponds to the lifetime of the fluorescence.

Non-radiative mechanisms include internal conversion, intersystem crossing and photophysical processes. Internal conversion ($k_{\mathrm{IC}}$) occurs when a vibrational states of the excited and ground states are coupled together and the molecule relaxes to the ground state, while dissipating all excess energy as heat. Through intersystem crossing (ISC) ($k_{\mathrm{ISC}}$) the singlet state can be changed to the triplet manifold. This process involves a change in the spin multiplicity of the molecule. Therefore, ISC is quantum mechanically forbidded according to the selection rules for electronic transitions. This means that all transitions $S_0 \rightarrow T_n$ or $T_n \rightarrow S_0$ are highly unlikely, but still possible. The probability for ISC is increased if the excited state lifetime is long and in the presence of heavy atoms. Resulting from this phosphorescence lifetimes are also very long. [12] Finally, the excited state can be deactivated intramolecularly by photophysical processes that include photoisomerization and photobleaching. [9, 10]

Since immediately after the absorption the molecule undergoes vibrational relaxation, the emitted photon will have lower energy compared to the quanta absorbed. This shifts the maxima of the fluorescence spectrum to longer wavelengths relative to the absorption maxima. This phenomenon is termed as the Stokes shift. The maximum of the phosphorescence spectrum is located at even higher wavelengths, since phosphorescence originates from the non-vibronically excited $T_1$ state, which lower in energy than the excited $S_1$ state.

Intermolecular deactivation pathways include energy transfer to another molecule and quenching. The quenching can happen by molecular collision or by forming a complex. The long-range interaction between molecules is termed as Förster mechanism ($k_{\mathrm{RET}}$), which is discussed more in Chapter 4 and the short-range interaction energy transfer termed as Dexter mechanism ($k_{\mathrm{DEX}}$). Dexter mechanism requires a wavefunction overlap and therefore can only occur at distances of order $10 - 20$ Å. [13]

Each of the these processes can occur in parallel, and measuring the rate constants of one process can be used to determine the rate constants of other processes.

# 3 The chlorophylls

This section is divided in to four major parts. Section starts by introducing some basic properties of various chlorophyll (Chl) molecules and their natural occurrency. The next section contains some of the basic chemical and structural properties of Chls. Third part introduces the optical properties of chlorophylls, *e.g.*, absorption and emission. Since the optical properties arise from the intrinsic electronic structure of the molecules, the most popular physical models used in the description of the conjugated $\pi$-electron system are presented, concentrating especially in the four-orbital model. Last part is devoted to the examination of aggregation properties of Chl complexes. Special attention is given to the optical properties of Chl aggregates.

## 3.1 Natural occurrence and basic properties

The most abundant colouring pigments found in nature comprise from different pyrrole pigments (porphyrins, (bacterio)chlorohylls, haem, vitamin $B_{12}$, bile pigments) [14]. Chlorophylls and bacteriochlorophylls are the photosynthetic pigments that can be found only from plants, bacteria and algae. Chls are all chlorins with the exception of Chl *c*, which is a phytoporphyrin type. The different Chl *c*'s are photosynthetic pigments found from marine lifeforms. The most abundant Chls found in nature are Chl *a* and Chl *b*, which usually occur in ratio of 3:1 [2]. These two chromophores are the major photosynthetic pigments in the plant kingdom. Nearly 100 different Chls and BChls are known today. Majority of these pigments exist in anoxygenic bacteria [15]. The term 'anoxygenic' is used for bacteria that do not produce oxygen in the photosynthetic process. Bacteria that belong to this group are purple bacteria, green sulphur bacteria and heliobacteria.

A second very important pigment found in photosynthetic organisms is the carotenoid molecule. Carotenoids absorb light ranging from blue to orange and also take part in light-harvesting. In addition, another important function of carotenoid molecules is in removing harmful triplets created by the long-lived excited states of Chl and BChl molecules. These triplet states are very lethal to living organisms, since they react with available oxygen and produce singlet oxygen, which is a very strong free radical. Interfering with this mechanism is the basis of many herbicides. This form of oxygen is called reactive oxygen species (ROS). [2]

Because of this Chls offer a tempting possibility in photodynamic therapy (PDT). PDT is used in the therapy of cancer to kill cancer cells. The strong absorption of Chls at long wavelengths is particularly beneficial, since at the wavelengths 650 - 850 nm the light penetration into living tissue is maximixed. Unfortunately most natural Chl molecules are water-insoluble and very unstable in the presence of light. However, chemically modified Chl molecules usually show better stability and tunability for the needs of PDT. Hence Chl derivates are used as sensitizers in photodynamic therapy. Chl derivatives can also be applied as natural biocides utilizing the same principles as used in PDT. [16]

Chemically, Chls are unstable in the presence both acids and bases. Also oxidation and light can degrade the Chl molecules. They have a significant tendency for aggregation and interaction with their molecular environments. Their optical properties are characterized by long-lived excited states and intense absorption in the spectral range of 330 - 800 nm. In aggregates or *in vivo* this range can be extended to 1020 nm [2].

The structure of Chl molecules and their derivates is very often investigated by X-ray diffraction [17], nuclear magnetic resonance (NMR) spectroscopy [18, 19] and mass spectroscopy (MS). Especially a combination of NMR and MS is usefull in determining the structural information. From the optical techniques, UV-Vis absorption gives qualitative information about aggregation degree of the samples and also identification of the chromophores. Photoluminescence measurements can be used to probe the electronical structure of chromophores. Circular dichroism spectroscopy can yield additional information about the stereochemistry of Chls in solutions and aggregates.

## 3.2 Structure

Chlorophylls belong to the family of molecules called porphyrins. Porphyrin molecules are aromatic heterocyclic macrocycles composed of four pyrrole molecules connected together with methine bridges (=CH−). Figure 3.1a-b shows the pyrrole and porphine molecules. Porphine molecule is rarely met in this form, but it functions as a simplified model, *e.g.*, in *ab initio* calculations of molecular orbitals.

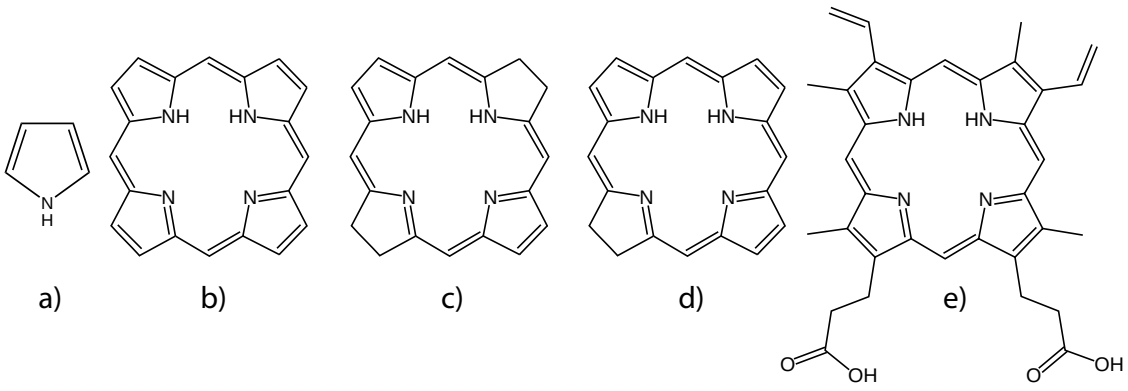


Figure 3.1: (a) Pyrrole. (b) Porphine. (c) Chlorin. (d) Bacteriochlorin. (e) Protoporphyrin IX.

In porphyrins, when the double bond between C-17 and C-18 is saturated, *i.e.*, the double bond is reduced to a single bond, chlorin macrocycle is formed. Here the letter C stands for asymmetric carbon and the numbering is performed according to Fig. 3.2. Furthermore, the saturation of the bond between C-7 and C-8 forms

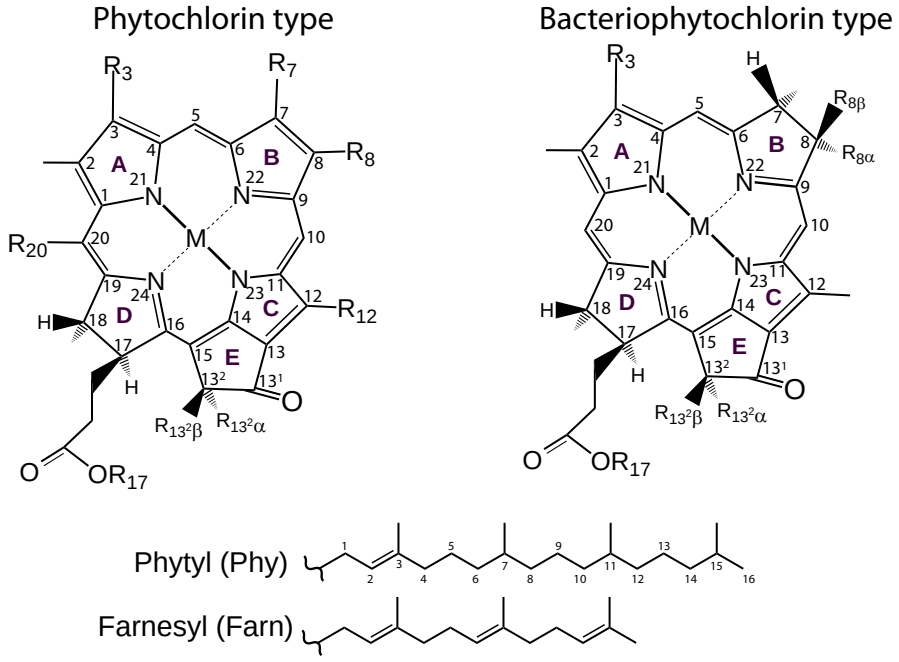


Figure 3.2: Molecule on the left shows a phytochlorin type of molecule and on the right side is the bacteriophytochlorin. On the bottom of the figure two of the most common "tails" are shown connecting to the position $R_{17}$. The structural variants of different chlorohyll molecules are presented in Table 3.1. Numbering according to IUPAC-UIB nomenclature (1988).

the bacteriochlorin macrocycle. Chlorin and bacterichlorin macrocycles are shown in Fig. 3.1c and d. These three different macrocycles form the basis of the variety of the chlorophyll molecules found in the nature. Figure 3.1e shows a protoporphyrin IX molecule that is very close to another important organic molecule haem, responsible for the oxygen binding properties of blood and also its distinctive red colour. As the prefix "proto" implies, protoporhyrin IX is also the prototype form, from which the variety of different (B)Chl molecules are formed. Furthermore, the IUPAC-IUB nomenclature in Fig. 3.2 emphasizes the fact that the isocyclic ring E in phytochlorin and bacteriophytochlorin types is derived from the C-13 propionic acid side chain of protoporphyrin IX.

Chlorophylls are chlorin derivates, where a fifth isocyclic pyrrole molecule is fused into the porphine structure. This additional pyrrole molecule gives the prefix "phyto" for porphyrin and chlorin type of molecules. Hence they are called phytoporphyrin and phytochlorin. For example, Chl *c* has phytoporhyrin macrocycle and Chl *a* and Chl *b* have a phytochlorin macrocycle. Occasionally, phytochlorin is referred to as phorbin by some authors, but this name will not be used in this thesis. Chls generally have Mg as the central metal and sesqui- ($C_{15}$) or di-terpenoid ($C_{20}$) alcohol esterified to the C-17 propionic acid chain, but there exist exceptions to both of these characteristics. For example, Pheophytin *a*, which is involved in the electron

transfer in the type II reaction centers, does not have the central metal. In other aspects, Pheo *a* is exactly like Chl *a*.

Table 3.1: Various peripheral substituents of chlorophyll and bacteriochlorophyll molecules corresponding to Fig. 3.2. Data taken from [2].

| **Pigment** | $\mathbf{R_3}$ | $\mathbf{R_7}$ | $\mathbf{R_8}$ ( $\mathbf{R_{8\alpha/8\beta}}$)[a] | $\mathbf{R_{12}}$ | $\mathbf{R_{13^2\alpha/13^2\beta}}$ | $\mathbf{R_{17}}$ | $\mathbf{R_{20}}$ | **M** |
|---|---|---|---|---|---|---|---|---|
| Chl *a* | $C_2H_3$ | $CH_3$ | $C_2H_5$ | $CH_3$ | $COOCH_3$/H | Phy | H | Mg |
| Chl *b* | $C_2H_3$ | CHO | $C_2H_5$ | $CH_3$ | $COOCH_3$/H | Phy | H | Mg |
| Chl $c_1$[b] | - | $CH_3$ | $C_2H_5$ | - | - | H | H | Mg |
| Chl *d* | CHO | $CH_3$ | $C_2H_5$ | $CH_3$ | $COOCH_3$/H | Phy | H | Mg |
| Pheo *a*[c] | $C_2H_3$ | $CH_3$ | $C_2H_5$ | $CH_3$ | $COOCH_3$/H | Phy | H | $H_2$ |
| BChl *a*[d] | $COCH_3$ | - | H/$C_2H_5$ | - | $COOCH_3$/H | Phy | - | Mg |
| BChl *b* | $COCH_3$ | - | -/=CH−$CH_3$ | - | $COOCH_3$/H | Phy | - | Mg |
| BChl *c* | $CHOHCH_3$ | $CH_3$ | $CH_2CH_n(CH_3)_{3-n}$[e] | $CH_3$/ $C_2H_5$[d] | H/H | Farn | $CH_3$ | Mg |
| BChl *f* | $CHOHCH_3$ | CHO | $CH_2CH_n(CH_3)_{3-n}$[d] | $CH_3$/ $C_2H_5$[e] | H/H | Farn | H | Mg |

[a] Phytochlorin type has only $R_8$-coordination, but bacteriochlorin type has two different branches emerging from $R_8$ denoted as $\alpha$ and $\beta$.
[b] Chl *c* has a phytoporphyrin macrocycle. Chl *c* are also called as chlorophyllides (Chlides), where the "-ide" ending denotes an unesterified acid side chain at C-17.
[c] Pheo a stands for Pheophytin *a*. It has the same structure as Chl *a*, but is missing the central metal.
[d] BChl stands for bacteriochlorophyll.
[e] Complex mixture of pigments with varying substituents at $C_8$ and $C_{12}$.

Phytochlorins contain four asymmetric (chiral) centers, which are located in C-$13^2$, C-17, C-18 and in the central metal. The phytol chain contains two asymmetric centers in C-7 and C-11 (notice different numbering in phytyl tail and phytochlorin macrocycle), which results in six asymmetric centers in phytochlorins containing phytyl chains. Bacteriophytochlorins have additional asymmetric centers in C-7 and C-8, hence giving it eight chiral centers with phytyl tails. [20]

### 3.2.1 The macrocycle and the electronic structure

The large macrocycle is the basis for both optical and redox chemistry of Chls. The electronic structure in porphyrins and (bacterio)chlorins is based on a planar macrocycle of 20 carbon atoms surrounding a central core of four nitrogen atoms. This configuration supports highly stable conjugated $\pi$-orbital electronic structure, which has alternating single and double bonds between the carbon atoms. The planarity of the macrocycle ensures a maximum overlap between the adjacent $\pi$-orbitals. Therefore, the $\pi$-electrons are free to move to neighboring $\pi$-orbital resulting in the delocalization of the $\pi$-electrons around the whole macrocycle.

The planarity of the macrocycle and the delocalization of $\pi$-electrons are the two classical criteria found in organic chemistry for aromacity. Consequently, since porphyrin and (bacterio)chlorin macrocycles are aromatic they naturally follow Hückel's rule. Hückel's rule state that aromatic molecule must have $4n+2$ $\pi$-electrons, where $n$ is zero or an integer. When placed in to external magnetic field, these delocalized $\pi$-electrons induce global ring currents that circulate around the whole macrocycle. In porphine, there exists many different bifurcations in the circulation of the ring currents since the pyrrole subunits remain unsaturated. However, in chlorins and bacteriochlorins the pyrrole subunits are saturated, which in turn limits the possible pathways for the ring currents. Figure 3.3a shows the tradional $18\pi$-[18]annulene aromatic pathway for a porphine macrocycle. This delocalization pathway can also be applied in chlorins and bacteriochlorins [21]. However, recent studies suggest that in reality all the $\pi$-electrons in the macrocycle participate in the aromatic delocalization, and the total delocalization pathway is a linear combination of all possible $(4n + 2)$ pathways [22].

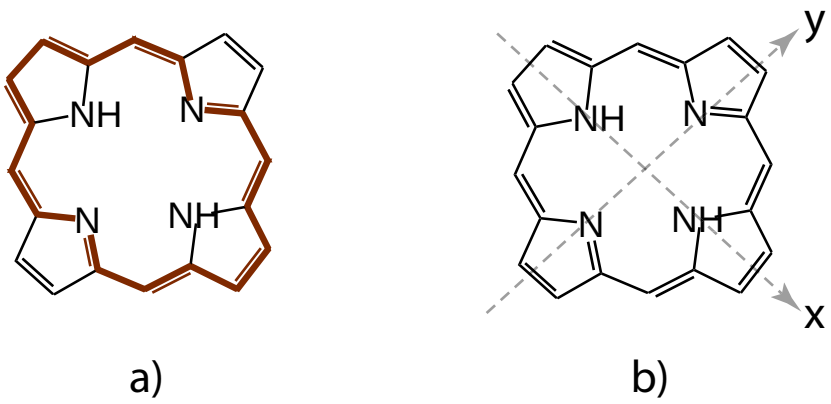


Figure 3.3: A porphine macrocycle showing (a) the the traditional $18\pi$-[18]annulene delocalization pathway in porphyrins and chlorins (b) the diagonal arrows as the two orthogonal symmetry axes denoted as x and y.

Many quantum mechanical models from a simple quantum wire model to more detailed models exist to explain the electronic properties of porphyrins and (bacterio)chlorins. However, the first model to give a satisfactory picture of the optical properties of porphyrins and chlorins was the four-orbital model developed by Gouterman [23, 24]. In addition, the four-orbital model has provided the basis for the theoretical work concerning the electronic and spectroscopic properties of the porphyrin molecules. [2]. In spite of the problems in Gouterman's model according to the newest research [25, 26], it still provides a reasonably realistic picture of the oscillator strengths and transition energies. In Gouterman's four-orbital model only the two highest occupied molecular orbitals (HOMO-1, HOMO) and two lowest unoccupied molecular orbitals (LUMO and LUMO+1 ) are considered. As an example, these orbitals are shown shown in Fig. 3.4 for a porphine macrocycle. The HOMOs

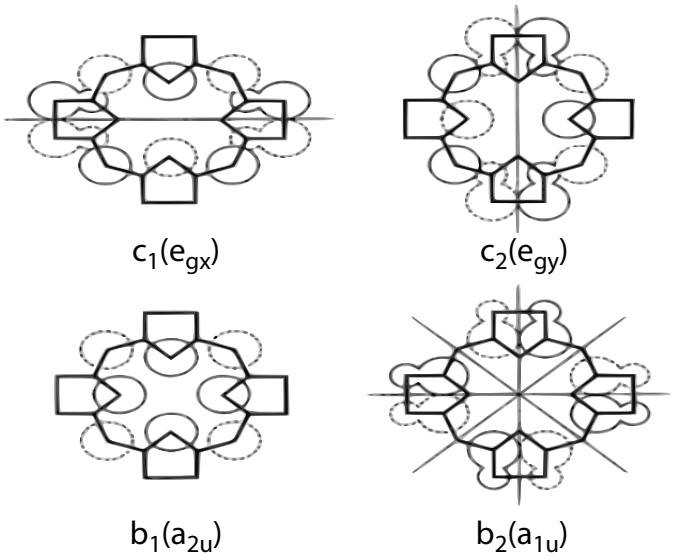


Figure 3.4: The HOMOs ($b_1$ and $b_2$) and LUMOs ($c_1$ and $c_2$) of a porphine macrocycle used in the Gouterman's four-orbital model. Solid and dashed circles indicate the sign. Symmetry nodes drawn in heavy lines. Picture taken from [27].

are labeled as $b_1$, $b_2$ and LUMOs $c_1$,$c_2$ to allow them to be followed into systems with less than $D_{4h}$ symmetry. Furthermore, the two LUMOs are divided from each other by using the two orthogonal symmetry axes defined in Fig. 3.3b and denoted as $e_{gx}$ and $e_{gy}$.

The structure of the macrocycle contribute substantially to the degeneracy and the energy of the orbitals. For example, a free-base porphine has $D_{2h}$ symmetry according to the Schönflies notation and the LUMO levels are almost degenerate. The introduction of a metal in the porphine macrocycle increases the symmetry and hence metalloporphyrin macrocycle has $D_{4h}$ symmetry. Resulting from this the LUMOs are exactly degenerate, but $a_{1u}$ is shifted to lower energy. However in chlorins, the saturation one of the pyrrole subunits reduces the symmetry of the molecule and chlorin macrocycles have $C_{2v}$ symmetry. This causes the LUMO and HOMO energy levels to spread apart.

Figure 3.5 shows the energy levels for the two HOMOs and LUMOs for a (a) free-base porphine, (b) metalloporphyrin and (c) chlorin macrocycle respectively. The arrows in Fig. 3.5 represent all the allowed electric-dipole transitions between the HOMO and the LUMO [2, 28]. In molecular theory, the electronic spectrum is interpreted in terms of single-electron transitions from occupied to unoccupied orbitals. Thus according to Fig. 3.5, the single-configuration excitations are described by transitions

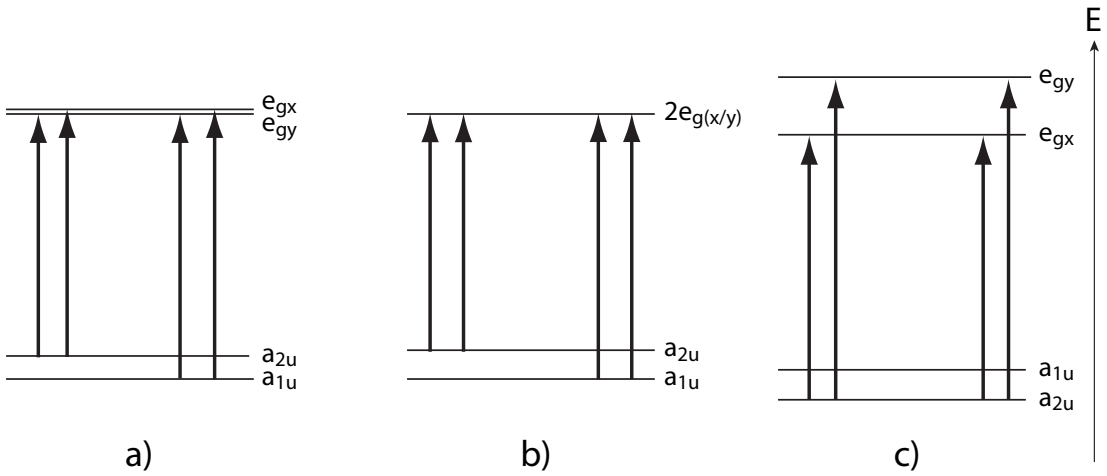


Figure 3.5: The energy levels for the HOMOs ($a_{2u}$ and $a_{1u}$,) and the LUMOs ($e_{gx}$ and $e_{gy}$), of a (a) metalloporphyrin macrocycle (b) metallochlorin macrocycle (c) chlorin macrocycle.

$a_{1u} \rightarrow e_{g(x/y)}$ or $a_{2u} \rightarrow e_{g(x/y)}$ as in Fig. 3.5 and are

$$\Phi_{a_{2u}e_{g(x/y)}} = a_{2u} - e_{g(x/y)} \tag{3.1}$$

$$\Phi_{a_{1u}e_{g(x/y)}} = a_{1u} - e_{g(x/y)}\,. \tag{3.2}$$

However, for porphyrins these single-configuration excitations do not provide realistic picture for the observed electronic spectrum. Hence, In 1960, Gouterman observed that a more accurate description of the excited states is obtained by configuration interaction (CI), where each state is a two orbital configuration formed from of the single-configuration excitations $\Phi_{a_{2u}e_{gx}}$, $\Phi_{a_{2u}e_{gy}}$, $\Phi_{a_{1u}e_{gx}}$ and $\Phi_{a_{1u}e_{gy}}$ [28]. These "four-orbitals" form the basis of Gouterman's theory and the spectroscopically observable states are obtained as the linear combinations of the single-configuration excitations as in

$$\begin{aligned}\Psi_{By} &= \frac{1}{\sqrt{2}}\left(\Phi_{a_{2u}e_{gy}} + \Phi_{a_{1u}e_{gx}}\right)\\ \Psi_{Bx} &= \frac{1}{\sqrt{2}}\left(\Phi_{a_{2u}e_{gx}} + \Phi_{a_{1u}e_{gy}}\right)\end{aligned} \tag{3.3}$$

$$\begin{aligned}\Psi_{Qy} &= \frac{1}{\sqrt{2}}\left(\Phi_{a_{2u}e_{gy}} - \Phi_{a_{1u}e_{gx}}\right)\\ \Psi_{Qx} &= \frac{1}{\sqrt{2}}\left(\Phi_{a_{2u}e_{gx}} - \Phi_{a_{1u}e_{gy}}\right)\,.\end{aligned} \tag{3.4}$$

The transition dipoles $\mathbf{r}$ of the $\Psi_{B(x/y)}$ and $\Psi_{Q(x/y)}$ states are formed by the reinforcement and cancellation of the transition dipoles of the single-configurations as in

$$\begin{aligned}\mathbf{r}_{B_{(x/y)}} &= \frac{1}{\sqrt{2}}\left(\mathbf{r}_{a_{2u}e_{g(x/y)}} + \mathbf{r}_{a_{1u}e_{g(y/x)}}\right) \\ \mathbf{r}_{Q_{(x/y)}} &= \frac{1}{\sqrt{2}}\left(\mathbf{r}_{a_{2u}e_{g(x/y)}} - \mathbf{r}_{a_{1u}e_{g(y/x)}}\right) \ . \end{aligned} \tag{3.5}$$

The transition dipole moments of the single-configuration transitions are given by

$$\mathbf{r}_{a_{(1/2)u}e_{g(x/y)}} = \langle a_{(1/2)u}|\hat{\mu}e_{g(x/y)}\rangle \ , \tag{3.6}$$

where $\hat{\mu}$ is the dipole moment operator. The oscillator strength f is proportional to the square of the transion dipole moment

$$f_{\mathrm{OS}} \propto |\ \mathbf{r}_{a_{(1/2)u}e_{g(x/y)}}\ |^2 \ . \tag{3.7}$$

In the case of macrocycle with $D_{4h}$ symmetry, the absolute values of the single-configuration transition dipoles are almost the same. Hence, $\mathbf{r_B}$ is very large ( 2 Å) and $\mathbf{r_Q}$ almost vanishes. Therefore, $\mathbf{r_Q}$ is said to be "forbidden by parity". This is fact is also supported by the experimental data of metalloporphyrins. [20, 28]

### 3.2.2 The peripheral substituents

By altering the peripheral substituents located around the macrocycle, considerable variations in the properties of the Chls are possible, *e.g.*, aggregation and optical properties. In fact, for most of Chls the only difference lies in the peripheral substituents, since the central metal and esterifying alcohol are the same. Regardless, only a minor change in the macrocycle is sufficient to create clearly observable differences between the different Chls.

Also in general, significant variations of substituents are possible with rings A and B without impairing the physiological and binding functions. Nonetheless, variations in ring D and especially in ring E are critical [29]. Another important effect that can be introduced by the peripheral substituents is steric hindrance by which the macrocycle comes distorted. For example, this can be realized by $CH_3$ in position C-20. The significance of the ever-present peripheral carbonyl substituent in C-$13^1$ is largely unknown, but some important facts are known. Cyclization renders this C=O group at C-$13^1$ coplanar with the macrocycle, which creates a pronounced red-shift. It may also give additional stiffness for the macrocycle, which reduces the probability of ISC of excited states and thereby decreases the losses in photosynthesis. H-bonding in the $13^1$ CO group is recognized as an important factor in different

interaction with proteins. [2]

### 3.2.3 The central metal

The most important aspect of chlorophyll type of molecules is their metal-binding ability [14]. It has decisive influence on the excited state kinetics, and this in turn affects how they perform in the photosynthetic process. Through the evolutionary process, nature has selected Mg as the central metal. This maximizes the excited state lifetime, while still maintaining low intersystem crossing to the triplet state. Transition metals with open d-shells and heavy metals would exhibit a large intersystem crossing probability, hence they would not function properly. Other metals like K, Na, Li and Ca can form unstable complexes, while trivalent metals introduce an extra charge. Thus, the only possible metals that remain are $Mg^{++}$, $Zn^{++}$ and $2H^{+}$, and in fact they are the only possible central metals found in nature. [2]. The most common bound metals that are found in nature are magnesium and iron, which gives additional selectional advantage for Mg. Other reason why Mg is preferred over Zn in photosynthetic systems could originate from the lower mass of Mg, which in turn lowers the probability for radionless relaxation by ISC. However, in other aspects Zn-Chls seem to be very similar to Mg-Chls, and Zn-Chls can replace Mg-Chls in all complexes [30, 31].

### 3.2.4 The esterifying alcohol

The esterifying alcohol is located in C-17 as shown in Fig. 3.2. For most (B)Chls this is phytyl or farnesyl, but other alcohols also exist. Phytyl and farnesyl chains are presented in Fig. 3.2. Of all the structural features, least is known about the functional significance of this long-chain esterifying alcohol. The influence of alcohol in the electronic structure of the molecule is negligible, since the macrocycle and central metal are mainly responsible for the properties [25]. In mono-disperse solutions, it has a very minor effect in the absorption properties.

Nevertheless, the alcohol moiety has a considerable effect in the interactions between the Chl molecules and its environment including the apo-protein, other Chls, carotenoids and lipids. For example, since the phytyl chain is hydrophobic it makes Chl *a* (and other Chls containing phytyl-chain) water insoluble. It is also noteworthy to mention that the alcohol chain has a considerable influence in the aggregation properties of Chls, especially in micellar systems [32]. Alcohol is also an important packing factor determining the spacing and orientation of Chls with respect to each other. This is a remarkably important aspect in photosynthetic systems where the distance and orientation between chromophores influence the efficiency of the energy transfer. All available structures determined by X-ray diffraction measurements support the spacing function created by the alcohol moiety [33].

## 3.3 Optical properties

Conjugated molecules usually exhibit strong absorption in the wavelength range of 220-1500 nm [10] and Chls are not exceptions in this sense. The absorption spectrum

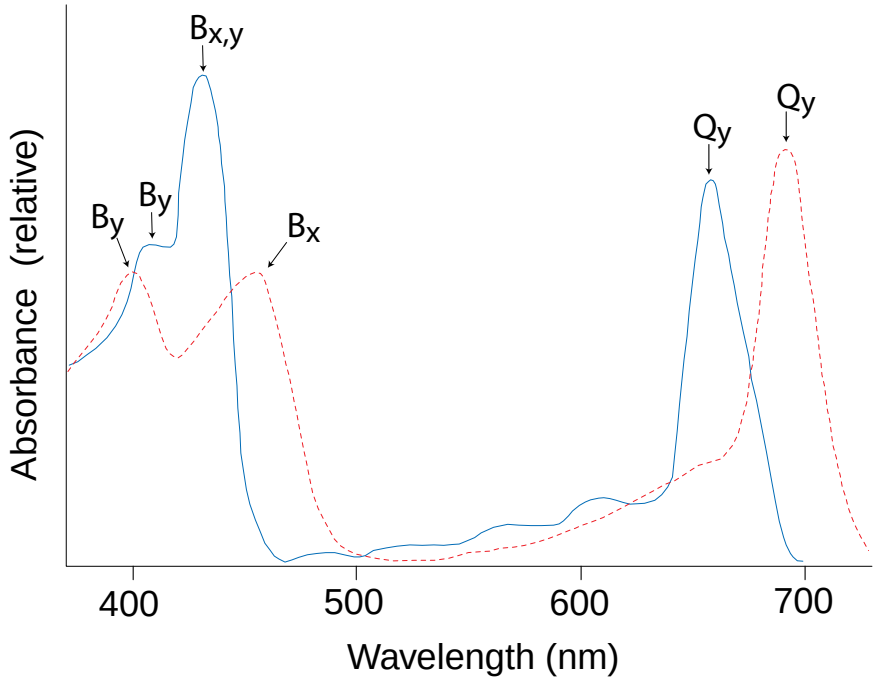


Figure 3.6: The absorption spectra of Chl *a* (blue-solid line) and Chl *d* (red-dashed line). Picture taken from [34].

of Chls can be described by characteristic absorption maximas. The absorption peaks in the blue-violet region of the electromagnetic spectrum are called the Soret or B-band. The red-infrared region absorption band is called the $Q$ band. Both B and Q bands arise from the $\pi \rightarrow \pi^*$ transitions, where $\pi^*$ denotes the excited state. In addition to these $\pi \rightarrow \pi^*$ transitions, electrons can also be excited to the HOMO from orbitals lower than LUMO, *e.g.*, $n \rightarrow \pi^*$ transitions. These states originate from the excitation of electrons from the nonbonded nitrogen orbitals of the pyrrole subunits to the excited $\pi^*$ orbitals of the macrocycle. This type of transitions are relatively weak in chlorins, but can be important in bacteriochlorins. Figure 3.6 shows a typical absorption spectra of Chl *a* and Chl *d*. The distinct Soret bands are divided in Chl *d* into two peaks, whereas the Soret band of Chl *a* is doubly degenerate exhibiting only single peak.

Porphyrins exhibits intense absorption in the blue region, but only adequate absorption in the visible. The introduction of the fift isocyclic ring reduces the symmetry in the porphinecyclic $\pi$-system forming phytoporphyrin. This doubles the absorption in the visible region and causes a minor red-shift in the absorption, which is characteristic for all Chls [28]. When the 17,18-double bond in ring D is reduced,

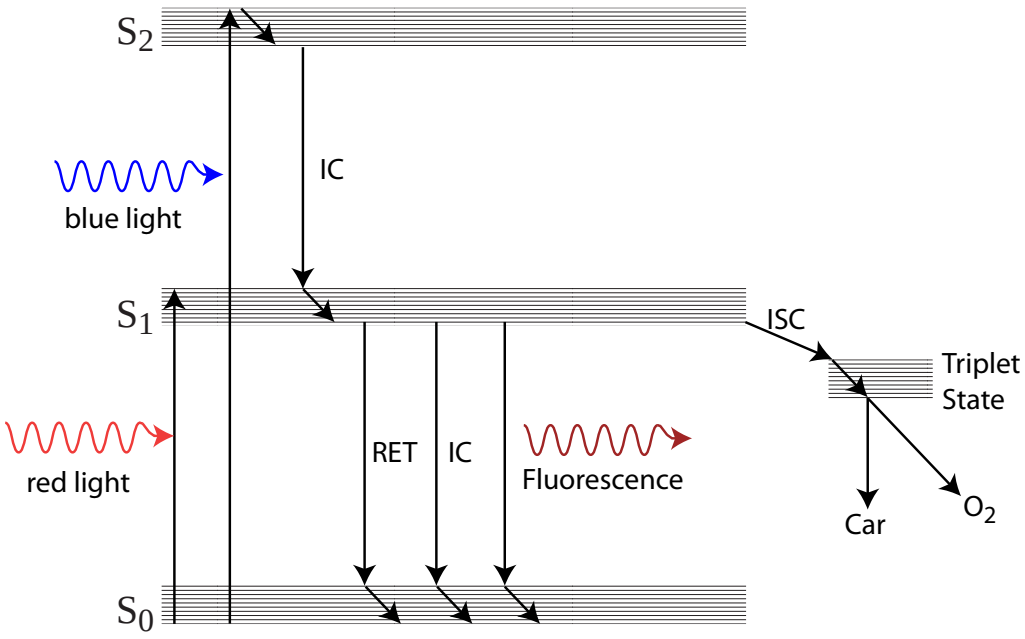


Figure 3.7: A simplified Jablonski diagram illustrating the possible excitations and relaxation mechanism of a chlorophyll molecule.

Table 3.2: Lifetimes of Chl *a* and Chl *b* *in vitro* and *in vivo*. Values obtained from [35].

| **Pigment** | **Fluorescence lifetime $\tau_F$ (ns)** |
|---|---|
| Chl *a* in *in vitro* | |
| benzene | 7,8 |
| ethyl ether | 5,1 |
| methanol | 6,9 |
| Chl *a* *in vivo* | |
| *Chlorella* | 1,6 |
| *Porphyridium* | 1,5 |
| *Anacystis* | 1,2 |
| Chl *b* in *in vitro* | |
| benzene | 6,3 |
| ethyl ether | 3,9 |
| methanol | 5,9 |

these effects become even more pronounced as is the case for Chl *a* and Chl *b*. The further reduction on 7,8-double bond in BChls can increase the absorption in the Vis and NIR range even two-three-fold. In addition, the available spectral range is nearly doubled, without the need of any additional help from protein interactions.

In Fig. 3.7 a schematical presentation of the chlorophyll energy levels and excita-

tion and relaxation dynamics is shown.The Figure shows that only two dominant excitation wavelengths exist corresponding to the Soret ($S_0 \rightarrow S_2$) and $Q$ ($S_0 \rightarrow S_1$) absorption bands. Once the electron is excited from the ground state $S_0$ either to the first $S_1$ or the second $S_2$ energy level, a part of the energy can be released by VR to the lowest vibrational level within the excited state or by IC to a lower energy state. From the first energy level $S_1$ electron has many possible pathways to the ground state, which are IC, fluorescence, FRET to another molecule or a triplet state via ISC. This triplet state produces reactive oxygen species or may be deactivated by a carotenoid molecule. Also only the transition between the levels $S_1$-$S_0$ can be used in photosynthesis. The reason for this is that the charge transfer performed by the photosystem can be realized only at wavelengths 680 nm (PSII) or 700 nm (PSI) [36].

Table 3.3: Absorption and fluorescence spectra maximas of photosynthetic pigments in different solvents. Values obtained from [2].

| **Pigment** | **Absorption in situ** | **Absorption in solution** $\lambda_{\mathbf{max}}(\epsilon)$**[solvent]**[a] | **Emission in solution** $\lambda_{\mathbf{max}}$**[solvent]** |
|---|---|---|---|
| Chl *a* | ∼440, 670-720 | 430, 662(78.8)[A]<br>430, 662(90)[D] | 668[A]<br>666[D] |
| Chl *b* | ∼460, 630-680 | 457, 646(46.6)[A]<br>454, 644(56.3)[D] | 652[A]<br>646[D] |
| Chl *d* | ∼440, ∼690 | 447, 668(98.3)[D]<br>454, 644(56.3)[D] | 695[D]<br>646[D] |
| Pheo *a* | ∼680 | 408, 505, 534, 667(55.2)[D] | 673[D] |
| BChl *a* | ∼440, ∼690, 800 -960 | 357, 391, 573, 772(91)[D]<br>365, 608, 772(60)[M] | 800 |
| BChl *b* | <400, ∼600, 800 -1020 | 368, 408, 579, 794(106)[D]<br>368, 407, 582, 795[A] | 810 |
| BChl *c* | ∼460, 730-760 | 432, 622, 660(92.7)[D]<br>435, 620, 670(70.9)[M] | 667[D] |

[a] $\lambda_{\max}$ in nm, $\epsilon$ in $\mathrm{cm^{-1}mM^{-1}}$, solvent abbreaviations: A = acetone, D = diethylether and M= methanol.

According the Fig. 3.7, the fluorescence quantum yield can be expressed using the rate constants as [37]

$$\phi_F = \frac{k_{\mathrm{F}}}{k_{\mathrm{F}} + k_{\mathrm{IC}} + k_{\mathrm{ISC}} + k_{\mathrm{RET}}}\,, \tag{3.8}$$

where $k_{\mathrm{F}}$ is the probability for spontaneous emission $S_1 \rightarrow S_0$, $k_{\mathrm{IC}}$ is the probablity for non-radiative transition $S_1 \rightarrow S_0$, $k_{\mathrm{ISC}}$ is the probability for transition $S_1 \rightarrow T_1$ and $k_{\mathrm{RET}}$ is the probability for energy transfer to another molecule. For example,

when two molecules are brought close to each other, $k_{\mathrm{RET}}$ and $k_{\mathrm{ISC}}$ are increased, which in turn decreases $\phi_F$ according to Eq. 3.8.

Hence, the optical properties of (B)Chls are exceptionally sensitive to the molecular environments [38]. In Table 3.2 the lifetimes of Chl *a* and Chl *b* *in vivo* and *in vitro* are listed. As can be seen from the values, the lifetimes are order of nanosecond even *in vivo*. These long lifetimes of the excited singlet state give rise to a high probability for ISC. Therefore, singlet to triplet transitions and ROS pose a problem when using Chls. In addition, the smaller fluorescence lifetimes *in vivo* is a clear indication of an efficient energy transfer between the Chl molecules (Eq. 3.8) [39]. Table 3.3 demonstrates the differences in the absorption and fluorescence spectra in different molecular envinroments. Even more pronounced variations can be induced by a direct protein-pigment or pigment-pigment interactions [40].

## 3.4 Aggregation

In nature, Chls are found in both aggregated forms and in protein-pigments complexes. In protein-pigment complexes, the protein matrix acts as the supporting structure for the Chls. It also ensures an optimal distance and orientation between the chromophores, since dense packing of chromophores has a danger called concentration quenching. This phenomena can be understood as a statistical process. There is always a chance that the pigment molecule is defective in such a way that the excited state of the molecule is short lived and relaxes by rapid internal conversion into ground state. If this defective molecule is isolated, then this process is negligible. But when this molecule is coupled to other molecules, they can act as a sink, which degrades the excitations of the light-harvesting unit to heat [20].

However, again, an exception can be found from the green photosynthetic bacteria, which grow in low light intensity envinroments. The light-harvesting organelle of these bacterias, called “chlorosome”, is most efficient natural antenna system formed by the self-assembly of BChls. It has developed to increase the light absorption per unit volume and to decrease the amount of protein per chromophore thus saving resources for the bacteria [41]. Similar kind of tubular structures have been synthetically fabricated *in vitro* by simply utilizing the self-assembling properties of BChls [42].

Resulting from their molecular architecture, Chls can very easily function as a building blocks for supramolecular interactions. These interactions have a non-covalent nature and the strongest of interactions is the metal ligation. For a long time it was known that Mg binds the extra ligands so strongly that it is practically never four coordinate. Removal of the extra ligand in unpolar solvents gives rise to increased aggregation where another Chl is donating a ligand. The central metal is also involved in the interactions between Chls and their apo-proteins [28]. In the crystal structures formed by Chl molecules, a variety of ligands have been identified: in more than 50% of known binding sites the ligand is histidine, but glutamine, asparagine, C=O groups and even water are known to be ligated [33,43]. These interactions may

be considered very important in the self-organized assembly of Chl molecules especially in hydrophobic environments. Ligand interactions are also known to change the electron density of the macrocycle and hence the properties of the molecule [44].

Second strongest bonding in the hierarchy of the supramolecular interactions is the hydrogen bonding. In the presence of multiple of hydrogen bonds, a very strong and directional bonding can be induced. Also nearly all (B)Chls carry a carbonyl group (C=O) in the C-$13^1$ and C-$13^2$ position, which can act as acceptor group for the hydrogen bonding.

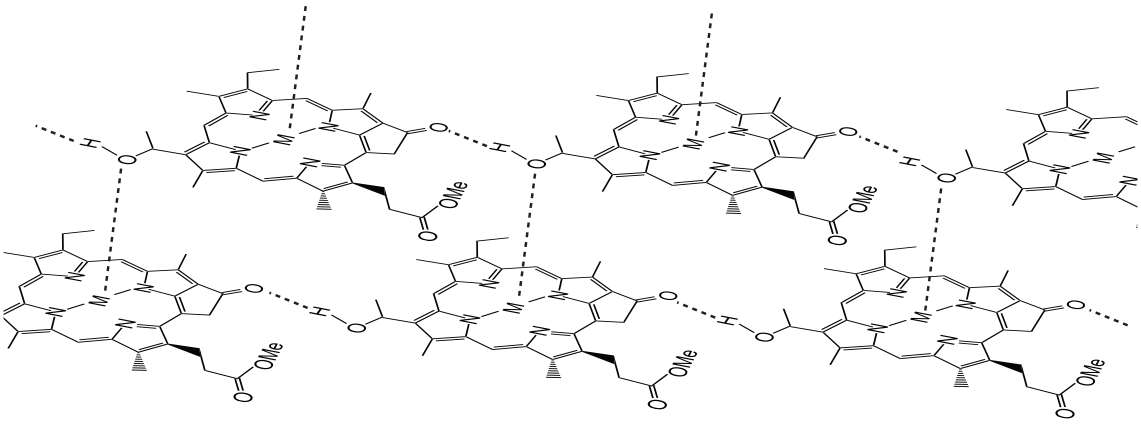

Figure 3.8: Stack of paraller oriented Chls with the phytyl tail replaced by a methyl group. The $3^1$-OH group can ligate with the central metal (M) and function as a hydrogen bond donor. The carboxyl group may function as a hydrogen bond acceptor.

The aromatic macrocycle is also an important reason for the pronounced tendency of aggregation of Chls via $\pi$-$\pi$ interactions also referred to as $\pi$-$\pi$-stacking. $\pi$-$\pi$-interactions arise from the intermolecular overlapping of the $\pi$-orbitals in the aromatic moieties. This type of bonding is strong and $\pi$-$\pi$ interactions play a substantial role in the interactions between Chls and proteins in photosynthetic complexes [20, 45].

Since all of these interaction mechanisms are simultaneouslya ctive, the stabilized supramolecular assembly can be much more stable in comparison with individual non-covalent interactions [46]. Figure 3.8 shows one possible set of Chl-Chl aggregation when the chromophores are aligned paraller to each other.

Chlorophyll aggregates usually show diminished fluorescence and shortening of the excited state lifetimes compared to monomeric moieties. [20] The decrease in fluorescence can be explained with efficient energy transfer between the molecules and with concentration quenching, but a more thorough inspection requires the help of excitonic theory of molecular crystals developed by Davydov in 1946. [47] According to the theory, the aggregation also increases the probability for ISC and thus enhances the lowest triplet state excitation in certain cases. [48] Generally, the degree

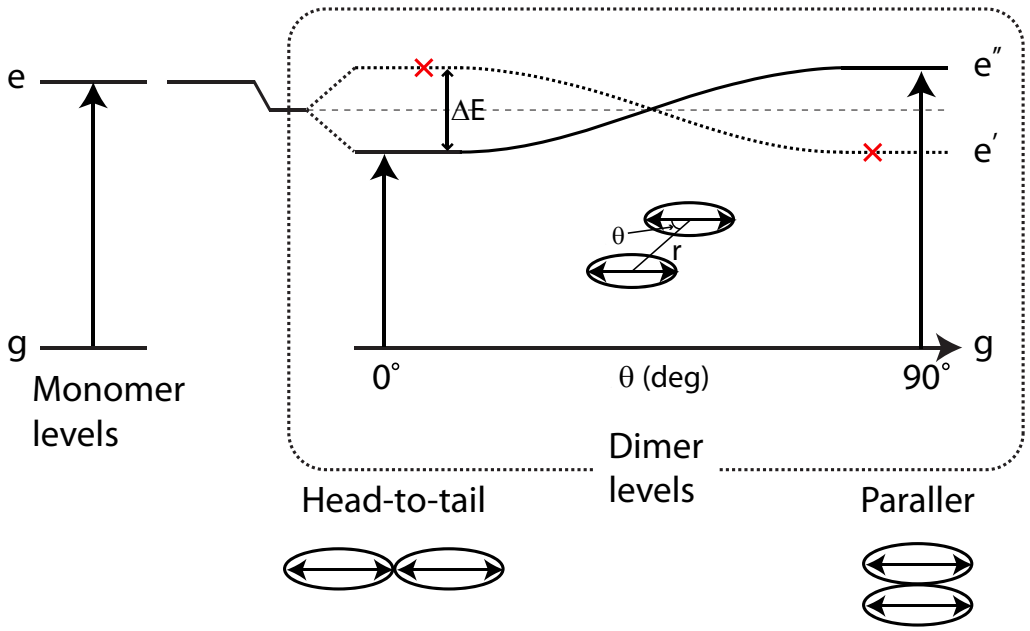


Figure 3.9: A schematic presentation of a exciton energy band for a dimer or identical molecules with paraller transition dipoles. The dashed line with the red crosses corresponds to the forbidden out-of-phase dipole arrangement. Adapter from [48].

of aggregation is observed from the spectral shifts in the absorption spectra. These spectral shifts can be qualitively explained by the exciton model applied for molecular spectroscopy introduced by Kasha *et al* [48]. In this approach, the Coulumbic interactions between the closely-packed chromohopres induce excitonic splitting of the excites states with different transition energies and oscillator strenghts. For example, a dimer with paraller transition dipole moments the excitonic splitting term in the point-dipole point-dipole approximation is given by

$$E = \frac{\boldsymbol{\mu}_u \cdot \boldsymbol{\mu}_v}{r^3} - 3\frac{(\boldsymbol{\mu}_u \cdot \mathbf{r})\,(\boldsymbol{\mu}_v \cdot \mathbf{r})}{r^5}\,, \tag{3.9}$$

where $\boldsymbol{\mu}_{u/v}$ is the transition dipole moment of the molecule $u/v$ and $\mathbf{r}$ is center-to-center position vector between the molecules, when $u$ is placed in the origin. When the dimer composes of identical chromophores the use of Eq. 3.9 yields the excitonic band splitting term:

$$\Delta E = \frac{2 \mid \boldsymbol{\mu}_{ge} \mid^2}{r^3}\left(1 - 3\cos^2\theta\right)\,, \tag{3.10}$$

where $\theta$ is the inclination angle between the molecules. This situation is illustrated in Fig. 3.9, where the effect of the excitonic interaction to the dimer energy levels is presented. The orientation of the chromophore dipole moments determines whether the excitonic coupling results in a higher (H-type) or lower (J-type) transition energy

compared to monomeric moeities. Also, Fig. 3.9 shows that the transition between the H-aggregate and the J-aggregate takes place at an angle $\theta = 54.7°$. At this angle the band splitting is zero no matter what the separation between the chromophores might be.

Furthermore, the difference in the optical behaviour of H-type and J-type aggregates is not limited to absorption spectra. For example, H-aggregates exhibit fluorescence quenching [48], which can be disadvantageous for optical systems, whereas J-aggregates may show even improved fluorescence compared to monomeric species. [49] Nevertheless, above models are only good approximations, since the aggregates are bound to exist in many different forms (dimers, trimers, oligomers) and orientations. Hence, the spectral shifts can be only used to detect the onset of aggregation, but do not allow for a quantitative inspection of the molecular structure.

# 4 Resonance energy transfer

Fluorescence or Förster resonance energy transfer (FRET, RET) is a process, where energy is transferred between atoms or molecules over distances that are longer than atomic (or moleculer) radii. In the near field that ranges from less than 10 Å to 100 Å, the transfer is radiationless and characterized by the inverse sixth-power depence. In the far field the transfer is radiative and is characterized by the inverse square law.

In 1920 it was known that fluorescence polarization started to decrease from solutions, when the concentration of fluorophores reached a critical value. Jean Perrin was the first to explain this effect by a Coulomb dipole-dipole interaction between the molecules [50]. This theory helped to undestand how the energy could be transferred to another molecule across some gap, even when there was not any wavefunction overlap between the molecules. However, Perrin made an error in his calculations, by assuming sharp resonances absortion and emission spectra. It took some years before Theodor Förster formulated the correct results taking into account the broadening of the spectra [51, 52]. He also derived the current form of the theory and also verified it by experimental data. [53]

RET is a widely used technique in medical, biological and physical sciences. Using RET, researchers have created colloidal QDs for chemical sensors [7, 54, 55], *in situ* monitoring of proteins in a living cell [56] and molecular rules for biological applications [57]. Artificial reaction centers have been created using cascading QD structures, where the funnel-like band gap profiles guide the exciton efficiently to the lowest band gap QD [58].

In section 4.1 the basic principles about RET are explained. Section 4.2 deals about the unified theory of RET, which can be derived using quantum electrodynamics (QED), which connects both the near- and far field regimes. Section 4.3 deals with orientational aspects between chromophores that affect the effiency of the RET.

## 4.1 Basic considerations

Resonance energy transfer requires two probes, a fluorescent donor ($D$) and an acceptor ($A$), which does not need to be fluorescent. When the donor is irradiated with appropriate energy, this creates an oscillating dipole, which can resonate with the acceptor in the near field. This resonating dipole-dipole interaction negotiates the energy from the donor to the acceptor. These interacting chromophores are treated as point dipoles, but more accurate models also exist. [59] The elementray RET process can be summarized with the following reaction formula

$$D^* + A \rightarrow D + A^* \,, \tag{4.1}$$

where the donor, which was initially in an excited state $D^*$, undergoes a transition to the electronic ground state, while the acceptor is promoted from its ground state

to an excited state $A^*$.

For an effective energy transfer to occur in the near field some requirements have to be fulfilled. First, the fluorescence spectrum of D and the absorbtion spectrum of A should adequately overlap. Also the quantum yield of donor ($\phi_D$) and the molar absorption coefficient of acceptor ($\epsilon_A \geq 1000$) have to be large enough. Thirdly, the transition dipole vector have to be favorably oriented to each other. [59, 60]

The most common formulae found in literature associated with RET are the efficiency of the energy transfer and rate constant ($k_{\mathrm{RET}}$). These formulae can be derived using classical approach with the Coulombic multipolar expansion, but with this approach they only apply in the near field. [61–63]

The efficiency of the energy transfer is a measure how much energy is transferred from $D$ to $A$. It is essentially a quantum yield of the energy transfer, which is defined as

$$E = \frac{\text{The number of quanta transferred from D to A}}{\text{The number of quanta absorbed by D}} \,. \tag{4.2}$$

$E$ can be measured in many ways including steady-state or time-resolved methods. However, the most popular method is the use of steady-state measurements and measuring the fluorescence intensity from a sample containing only $D$ ($F_D$) and fluorescence intensity of $A$ from a sample containing both $D$ and $A$. Using the fluorescent intensities Eq. 4.2 can be defined as

$$E = 1 - \frac{F_{DA}}{F_D} \,. \tag{4.3}$$

If the values $F_D$ and $F_A$ are normalized to their respective concentration of D, Eq. 4.3 can also be expressed as [59]

$$E = \frac{1}{1 + (R/R_0)^6} \,. \tag{4.4}$$

where $R_0$ is the Förster length, which relates to the donor-acceptor distance when the efficiency given by Eq. 4.4 is 50 %. Förster length can also be defined as

$$R_0^6 = \frac{9000 \ln(10)}{128 \pi^5 N_A} \kappa^2 n^{-4} \phi_D J_{DA} \,, \tag{4.5}$$

where $N_A \approx 6,022 \cdot 10^{23}\,\mathrm{mol}^{-1}$ is the Avogadro constant, $\kappa^2$ is the Förster orientation factor, $\phi_D$ is the quantum efficiency of $D$, n is refractive index of the material (which is usually assumed isotropic and non-dispersive) and $J_{DA}$ is the overlap of the $D$ fluorescence spectrum with the $A$ absorption spectrum. The Förster orientation

factor is defined as [59]

$$\kappa = \vec{n}_A \cdot \vec{n}_D - 3(\vec{n}_R \cdot \vec{n}_D)(\vec{n}_R \cdot \vec{n}_R)\,, \tag{4.6}$$

where $\vec{n}_{D,A} = \boldsymbol{\mu}_{\mathbf{D,A}} / \mid \mu_{D,A} \mid$ are the corresponding unit vectors of the acceptor and donor transition dipole moments and $\vec{n}_D$ is the unit vector pointing from donor to acceptor. The effect of $\kappa$ will be discussed in more detail in Chapter 4.3.

The overlap integral is defined as

$$J_{DA} = \int_0^\infty F_D(\lambda)\epsilon_A(\lambda)\lambda^4\, d\lambda / \int_0^\infty F_D(\lambda) d\omega \quad (\mathrm{M}^{-1}\mathrm{cm}^3)\,, \tag{4.7}$$

where $F_D(\omega)$ is the donor fluorescence per unit wavelength interval and $\epsilon_A(\lambda)$ is the acceptor molar absorption coefficient at waveleght $\lambda$. Usually the donor fluorescence is normalized to unity, which simplifies the overlap integral to

$$J_{DA} = \int_0^\infty F_D(\lambda)\epsilon_A(\lambda)\lambda^4\, d\lambda \quad (\mathrm{M}^{-1}\mathrm{cm}^3)\,. \tag{4.8}$$

The constant in the Eq. 4.5 depends on the used units. For example, the acceptor absorption spectrum can be expressed with the molar absorption coefficient $\epsilon$ or as the absorption cross-section $\sigma$, which are connected by

$$\sigma = 1000 \ln(10) \frac{\epsilon}{N_A} \qquad (\mathrm{M}^{-1}\mathrm{cm}^2)\,. \tag{4.9}$$

In Fig. 4.1, a plot of RET efficiency ($E$) is presented as a function of distance $R$. The efficiency has been calculated with Eq. 4.4. The different $R_0$ values are taken from Ref. [64]. From the graph one can see that when the distance is $\leq 0.5\, R_0$ the curve becomes flat. Also the maximum efficiency in this relationship is reached more abruptly than its minimum. Because of this, longer distances may be determined slightly more accurately than shorter distances.

The second commonly used formula is the rate of the energy transfer, which is given by

$$k_{\mathrm{RET}} = \frac{1}{\tau_D} \left( \frac{R_0}{R} \right)^6 . \tag{4.10}$$

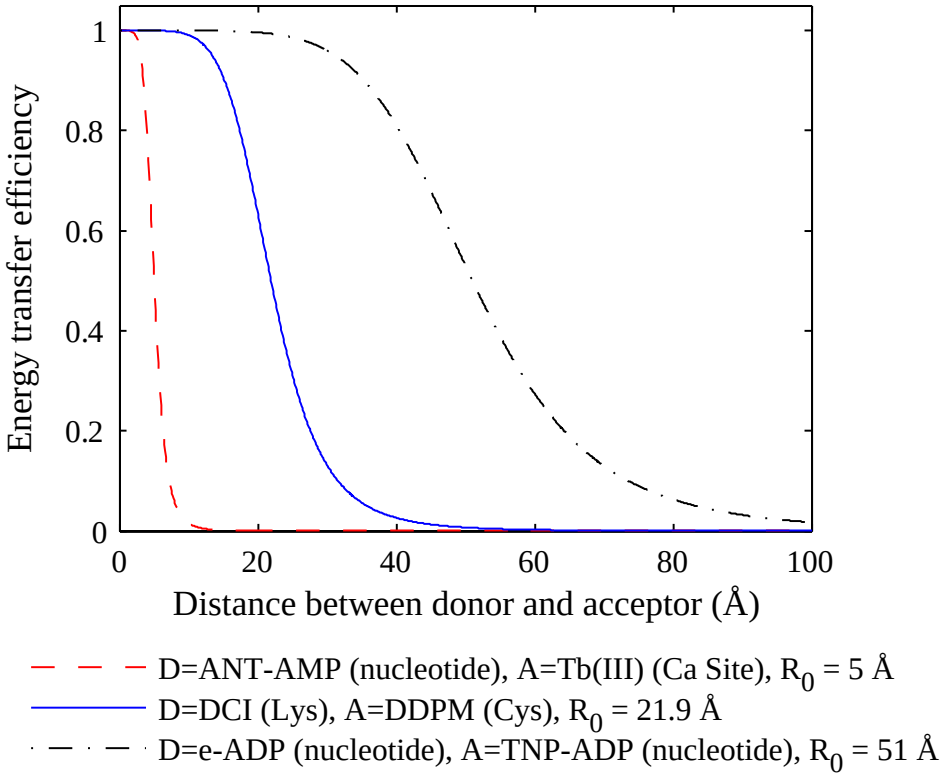


Figure 4.1: The energy efficiency of three different donor and acceptor pairs as a function of distance $R_{DA}$.

When $R_0$ from Eq. 4.5 is placed into 4.10, one obtains

$$k_{\mathrm{RET}} = \frac{9000\ln(10)\phi_D\kappa^2}{128\pi^5 n^4 \tau_D R^6 N_A}\int_0^\infty F_D(\lambda)\epsilon_A(\lambda)\lambda^4\,d\lambda\,. \tag{4.11}$$

If we use the acceptor absorption cross-section instead of the molar absorption coefficient and $\omega$ instead of $\lambda$, the transfer rate takes following form

$$k_{RET} = \frac{9c^4\phi_D\kappa^2}{8\pi n^4\tau_D R^6}\int_0^\infty \frac{F_D(\omega)\sigma_A(\omega)}{\omega^4}\,d\omega\,. \tag{4.12}$$

As can be seen from Eq. 4.12 the transfer rate has a characteristic $R^{-6}$ dependency. As a result, the distance between the donor and acceptor is a key factor in determining the efficiency of the energy transfer. Another key factor lies in the molecular environments, in which the donor and acceptor are situated. The influence of the molecular environment is described in Eq. 4.12 using the refractive index, which has

$n^{-4}$ dependency. Naturally, if other molecules are in the vicinity of donor and acceptor, they induce losses or alternative pathways for energy transfer and thus decrease the transfer rate between donor and acceptor. It is also noteworthy to state that Eq. 4.11 is more practical when chemical information about the fluorescent species is known and Eq. 4.12 is more usable when spectroscopic data is available. However, all of the variables used in both equations can be determined with relative ease using proper equipment.

## 4.2 Quantum electrodynamical inspection of RET

Using the semiclassical inspection of the phenomenom does not not fully solve the problem, since it only applies for the near field. Hence, the semiclassical theory is only an approximation. Using Quantum Electrodynamics (QED) theory, where both the matter and photons are quantized, one can obtain a unified theory for the radiative and radiationless energy transfer. With this theory, the different near- and far field behaviours are the limiting cases for a more general mechanism that operates over all distances. In classical theories, radiationless energy transfer contains an assumption that energy is transferred instantaneously from D to A, but this is justified only in the near zone, *i.e.*, when the distance between the donor and the acceptor is less than the reduced wavelength $\lambda\!\!\!^{-} = \lambda/2\pi$, where $\lambda$ is the wavelength corresponding to the energy transfer.

Usually the molecules that participate in the energy transfer are surrounded by other molecules. Naturally, this affects the transfer dynamics. This formulation uses the common multipolar (Power-Zienau-Woolley) form of QED. The key point of this theory is the cancellation of all longitudinal Coulumbic interactions [65]. When using this formulation any interaction between electronically neutral species invokes the creation and annihilation of photons.

To examine the energy transfer between two selected molecules $D$ and $A$, the whole system is divided into two parts. One subsystem consists of the selected molecule pair of $D$ and $A$. The other subsystem consists of quantized radiation field and the remaining molecules that are situated in the surrounding medium, which is referred to as the "polariton bath". In this formulation the interaction between $D$ and $A$ is mediated by the bath polaritons.

When the system is unperturbed, it is desribed by the zeroth-order Hamiltonian ($H^0$). The excitation of the system can be treated as a perturbation of system, which is given by the interaction term ($V$). Using these notations the total Hamiltonian is [59, 65]

$$H = H^0 + V\,, \tag{4.13}$$

where

$$H^0 = H_{\text{bath}} + H_{\text{mol}}(D) + H_{\text{mol}}(A) \tag{4.14}$$
$$V = H_{\text{int}}(D) + H_{\text{int}}(A)\,. \tag{4.15}$$

$H_{\text{bath}}$ is the "bath" Hamiltonian that contains the radiation Hamiltonian and the contributions of all other molecules except $D$ and $A$. It is given by

$$H_{\text{bath}} = H_{\text{rad}} + \sum_{\xi \neq D,A} \left(H_{\text{mol}}(\xi) + H_{\text{int}}(\xi)\right)\,, \tag{4.16}$$

where $\xi$ denotes the molecule $\xi$. For the sake of simplicity, only the energy transfer between donor-acceptor pair in vacuum will be examinded, since the mathematical treatment is simpler. However, the examination of the effect of dielectric medium surrounding the molecular pair follows the same logic as *in vacuo*. The only difference is that the energy is not mediated by the bath polaritons, but virtual photons. The photons are deemed virtual, since at small distances between D and A their lifetime is short according to the uncertainty principle. However, when the interaction-pair separation is increased this uncertainty is reduced and photons gain a real character, which is characterized by the radiative transfer in the far zone. When examining the transfer dynamics *in vacuo*, the effects of surrounding molecules are discarded in Eq. 4.16 and the zeroth-order Hamiltonian is reduced to

$$H^0 = H_{\text{rad}} + H_{\text{mol}}(D) + H_{\text{mol}}(A) + V\,. \tag{4.17}$$

Since the interaction term $V$ in Eq. 4.15 stays the same, the total Hamiltonian is given by

$$H = H_{\text{rad}} + H_{\text{mol}}(D) + H_{\text{mol}}(A) + H_{\text{int}}(D) + H_{\text{int}}(A)\,. \tag{4.18}$$

The Hamiltonian for the quantized radiation field, which can be expressed using the creation- and annihilation operators ($\hat{a}^\dagger_{\mathbf{k},\lambda}$, $\hat{a}_{\mathbf{k},\lambda}$) corresponding to wavevector $\mathbf{k}$ and polarization state of a photon $\lambda$ ($\lambda = 1, 2$) [65, 66]

$$H_{\text{rad}} = \sum_{\mathbf{k},\lambda} \hbar c k \left(\hat{a}^\dagger_{\mathbf{k},\lambda}\hat{a}_{\mathbf{k},\lambda}1 + e_{vac}\right)\,, \tag{4.19}$$

where $\sum_{\mathbf{k},\lambda}$ is a shorthand notation of $\sum_{\mathbf{k}}\sum_{\lambda}$, $\hat{a}_{\mathbf{k},\lambda}$ is a shorthand notation of $\hat{a}^\lambda(\mathbf{k})$ and $e_{vac}$ is the vacuum energy (usually $e_{vac} = 1/2$). The creation- and annihilation

operators obay the following relations

$$[\hat{a}_{\mathbf{k},\lambda}, \hat{a}^{\dagger}_{\mathbf{k}',\lambda'}] = \delta_{\mathbf{k},\mathbf{k}'}\delta_{\lambda,\lambda'}, \qquad \hat{n}_{\mathbf{k},\lambda} = \hat{a}^{\dagger}_{\mathbf{k},\lambda}\hat{a}_{\mathbf{k},\lambda} \tag{4.20}$$

$$\hat{a}^{\dagger}_{\mathbf{k},\lambda}\hat{a}_{\mathbf{k},\lambda} = n\,|n_{\mathbf{k},\lambda}\rangle\,, \qquad n = 0, 1, 2, \ldots \tag{4.21}$$

$$\begin{aligned} &\hat{a}_{\mathbf{k},\lambda} = \sqrt{n}\,|n-1\rangle\,, \qquad n = 1, 2, 3, \ldots \\ &\hat{a}_{\mathbf{k},\lambda}\,|0\rangle = 0 \end{aligned} \tag{4.22}$$

$$\hat{a}_{\mathbf{k},\lambda}\,|n\rangle = \sqrt{n+1}\,|n+1\rangle\,, \qquad n = 0, 1, 2, \ldots \tag{4.23}$$

where $|0\rangle$ is the vacuum state, *i.e.*, a state without photons.

The interaction Hamiltonian describes the interaction between the quantized radiation field and the molecule $\xi$. When the dipole-dipole coupling (E1-E1 coupling) is allowed, the electric dipole approximation of the interaction Hamiltonian is sufficient. The reason for this is that the higher-order electric coupling and magnetic multipolar couplings are comparatively small. Nevertheless, one example when this approximation is not valid can be found in plants. Coupling between two chromophores in plants, carotenoid and chlorophyll molecules, is not E1-E1 allowed. In such cases higher-order multipole coupling have to be taken into consideration. [67, 68] Again for simplicity, processes are assumed to be E1-E1 allowed, and within this approximation the electric dipole interaction Hamiltonian is

$$H_{\text{int}} = -\epsilon_0^{-1}\hat{\mu}(\xi)\cdot\hat{d}^{\perp}(R_{\xi})\,, \tag{4.24}$$

where $\hat{d}^{\perp}(R_{\xi})$ is the electric displacement operator of molecule $\xi$ positioned at place $R_{\xi}$ and $\hat{\mu}$ is the electric dipole operator of molecule $\xi$. Displacement operator can be written as the mode expansion [65]

$$\hat{d}^{\perp}(R) = i\sum_{\mathbf{k},\lambda}\left(\frac{\hbar ck\epsilon_0}{2V}\right)\left(\hat{e}_{\mathbf{k},\lambda}\hat{a}_{\mathbf{k},\lambda}e^{i\mathbf{k}\cdot\mathbf{R}} - \hat{e}^{-}_{\mathbf{k},\lambda}\hat{a}^{\dagger}_{\mathbf{k},\lambda}e^{-i\mathbf{k}\cdot\mathbf{R}}\right)\,, \tag{4.25}$$

where the sum has been taken over radiation modes characterized by the wave-vector $\mathbf{k}$ and polarization $\lambda$, $\hat{e}_{\mathbf{k},\lambda}$ is the polarization vector, $\hat{e}^{-}_{\mathbf{k},\lambda}$ is the complex conjugate of the polarization vector, V is an arbitrary quantization volume and R is the position of the molecule.

With the help of Eq. 4.1, the transfer process can be split into initial and final states, which consists of three state vectors: donor, acceptor and the radiation field. The initial state of the system is described by the state vector $|I\rangle$. In the initial state, the

donor is excited and the acceptor is in the ground state. The final state is described by the state vector $|F\rangle$ D being in the ground state and A excited. Radiation field is in both cases in the ground state, since the virtual photon that mediates energy exists only between these states. Hence the radiation field is described by the vacuum state $|0\rangle$. State vectors of donor and acceptor are assumed to implicitly contain the vibrational contributions, which are separable from the electronic states on the basis of the Born-Oppenheimer principle as

$$|D\rangle = |D_{\mathrm{el}}\rangle\,|\varphi_D^{(n)}\rangle\,, \qquad |D^*\rangle = |D_{\mathrm{el}}^*\rangle\,|\varphi_{D^*}^{(r)}\rangle \tag{4.26}$$

$$|A\rangle = |A_{\mathrm{el}}\rangle\,|\varphi_A^{(m)}\rangle\,, \qquad |A^*\rangle = |A_{\mathrm{el}}^*\rangle\,|\varphi_{A^*}^{(p)}\rangle\ , \tag{4.27}$$

where subscript "el" refers to the electronic part of the state vectors, indices $n$, $r$, $m$ and $p$ specifying the vibrational, rotational or other sublevels of D or A.

The initial ($|I\rangle$) and final ($|F\rangle$) states of the whole system (molecules plus radiation) can be presented as the product wavefuntion

$$|I\rangle = |D^*\rangle\,|A\rangle\,|0\rangle\,, \qquad |F\rangle = |D\rangle\,|A^*\rangle\,|0\rangle\ , \tag{4.28}$$

with corresponding energies

$$E_I = e_{D^*} + e_A + e_{vac}, \qquad E_F = e_D + e_{A^*} + e_{vac}\,. \tag{4.29}$$

Since the energy transferred has to satisfy the energy convervation, *i.e.*, initial and final states have to have the same energy, the total energy transferred in the process is $E_I = E_F = \hbar cK$. In the presence of a surrounding medium, this would not necessarily be the case, since the presence of other molecules could induce losses.

The energy transfer is a second-order process, where the energy is mediated by the virtual photons as discussed before. This process is presented in Fig. 4.2. According to Fig. 4.2, two intermediate states are possible in the energy transfer. Figure 4.2a corresponds to the situation ($q = 1$), where the transition $D^* \to D$ precedes the transition $A \to A^*$, when in the the second case ($q = 2$) the order is opposite, as in Fig. 4.2b. The latter process presents a rather anomalous situation, where the transition $A \to A^*$ produces a virtual photon and the annilation of the photon induces a downward transition of D. Nevertheless, both processes must be taken into account when using the time-dependent perturbation theory. First order processes are the absorption of a photon and the emission of a photon, which are shown in Fig. 4.3. First order prosesses can be described with first order perturbation theory, but they do not contribute to the transfer process and can be neglected. The rate of the transfer of excitation energy from the donor to the acceptor is given by the

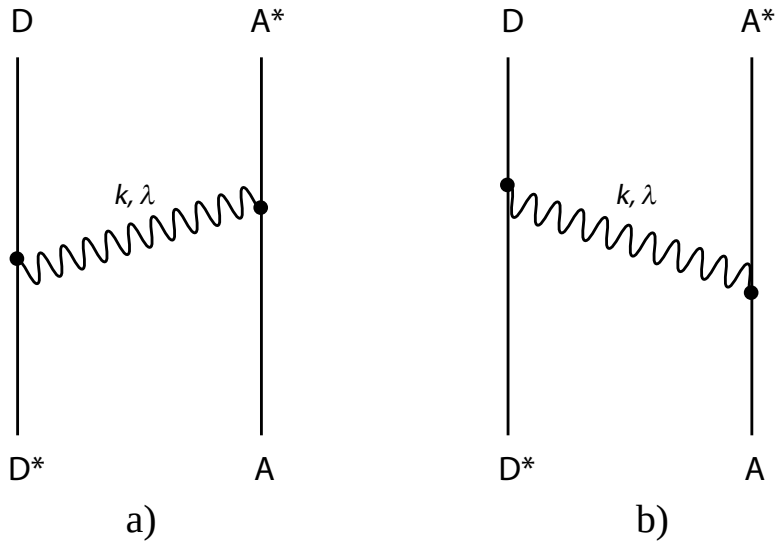


Figure 4.2: Time-ordered Feynman diagrams for the resonant energy transfer, where time is progressing upward. In both cases a virtual photon labeled $\mathbf{k}, \lambda$ transfers energy from the initially excited donor $D^*$ to the acceptor $A$.

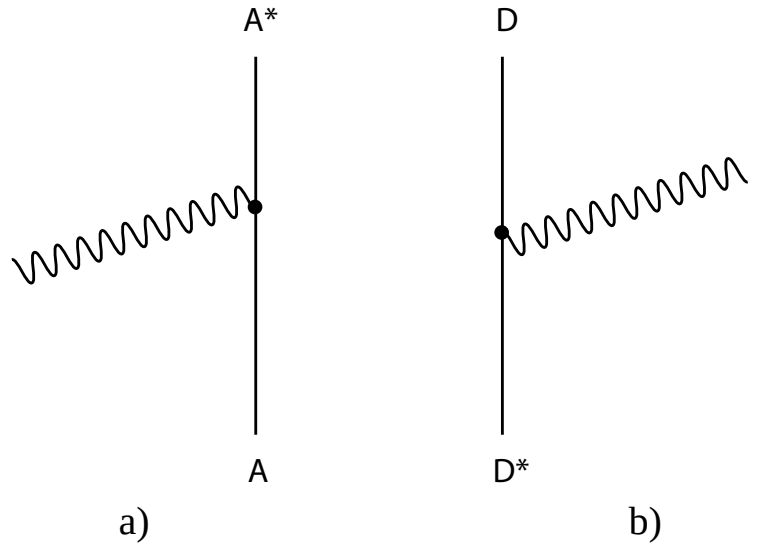


Figure 4.3: Time-ordered Feynman diagrams for a) photoabsorption and b) photoemission. Again time progressing upwards.

Fermi's Golden Rule [66]

$$\Gamma_{FI} = \frac{2\pi}{\rho}\hbar \mid \langle F| V |I\rangle \mid^2 \delta(E_I - E_F)\,, \tag{4.30}$$

where $\rho$ is the density of final states. The matrix element $\langle F|\, V\, |I\rangle$ can be defined using second order perturbation theory as follows [69, 70]

$$\begin{aligned}\langle F|\, V\, |I\rangle &= \sum_{q=1}^{2} \frac{\langle F|\, V\, |M_q\rangle \langle M_q|\, V\, |I\rangle}{E_I - E_q} \\ &= \frac{\langle F|\, H_{\rm int}\, |M_1\rangle \langle M_1|\, H_{\rm int}\, |I\rangle}{\underbrace{e_{D^*} - e_D}_{\hbar cK} - \hbar ck} + \frac{\langle F|\, H_{\rm int}\, |M_2\rangle \langle M_2|\, H_{\rm int}\, |I\rangle}{\underbrace{e_A - e_{A^*}}_{-\hbar cK} - \hbar ck}\,, \end{aligned} \tag{4.31}$$

where $M_1$ and $M_2$ correspond to intermediate states, in which either both donor and acceptor are in ground ($q = 1$) or excited ($q = 2$) state. In both states a virtual photon with energy $\hbar ck$ exists. The energies corresponding to these states are given by

$$E_1 = e_D + e_A + \hbar ck, \qquad E_2 = e_{D^*} + e_{A^*} + \hbar ck \tag{4.32}$$

and the state vectors

$$|M_1\rangle = |D\rangle\, |A\rangle\, |1\rangle \tag{4.33}$$

and

$$|M_2\rangle = |D^*\rangle\, |A^*\rangle\, |1\rangle\ , \tag{4.34}$$

where

$$|1\rangle = a^\dagger_{\mathbf{k},\lambda}\, |0\rangle\ , \tag{4.35}$$

is the radiation field promoted to one photon state.
Since solving of the matrix elements defined in Eq. 4.30 requires some extensive calculations, the derivation is presented in Appendix A. The result is

$$\langle F|\, V\, |I\rangle = \mu_i^{\rm full}(D) V_{ij}(K, \mathbf{R}) \mu_j^{\rm full}(A)\,, \tag{4.36}$$

where $V_{ij}$ is the retarded dipole-dipole coupling tensor between the donor and acceptor. In the presence of other molecules, the only difference would be in $V_{ij}$, but otherwise the derivation would be the same.

$$V_{ij}(K, \mathbf{R}) = \frac{K^3 e^{iKR}}{4\pi\epsilon_0} \left[ \left(\delta_{ij} - 3\vec{R}_i\vec{R}_j\right) \left( \frac{1}{K^3R^3} - \frac{i}{K^2R^2} \right) - (\delta_{ij} - \vec{R}_i\vec{R}_j) \frac{1}{KR} \right], \tag{4.37}$$

where $\vec{R} = \mathbf{R}/R$. The above electromagnetic tensor contains the $R^{-3}$ term characteristic for the near zone, $R^{-1}$ for the far zone and also $R^{-2}$ term for the intermediate distances between near and far zone. Notice that the orientational factors of near and far field are different leading to range dependence in fluorescence anisotropy.

Inserting the full transition dipoles from Eqs. A.4 and A.5 back to the matrix element defined in Eq. 4.36, and performing averaging over the initial molecular states and summing over the final molecular states in Eq. 4.30, the transfer rate is

$$\begin{aligned}\Gamma_{DA} &= \frac{2\pi}{\hbar}\left|\mu_i^{\text{full}}(D)V_{ij}(K,\mathbf{R})\mu_j^{\text{full}}(A)\right|^2\delta(E_I-E_F)\\ &= \frac{2\pi}{\hbar}\sum_{n,m,p,r}\rho_{D^*}^{(n)}\rho_A^{(m)}\mid\langle\varphi_D^{(r)}|\varphi_{D^*}^{(n)}\rangle\mid^2\mid\langle\varphi_{A^*}^{(p)}|\varphi_A^{(m)}\rangle\mid^2\mid\mu_i(A)\mu_j(D)\mid^2\ldots\\ \ldots &\quad \mid V_{ij}(K,\mathbf{R})\mid^2\delta(e_{D_n^*}+e_{A_m}-e_{D_r}-e_{A_p^*}),\end{aligned}\tag{4.38}$$

where $\rho_{D^*}$ and $\rho_A$ are the population distribution functions of the initial vibrational states of the donor and acceptor. The connection between Eq. 4.38 and with the Förster formula Eq. 4.12 can be expressed in terms of the overlap integral between donor and acceptor spectra. First $\mid V_{ij}(K,\mathbf{R})\mid^2$ must be calculated. We start by setting $K=\omega/c$ and $\kappa_q=\delta_{ij}-q(\vec{R}_i\vec{R}_j)$, where $q=1,3$, and obtain

$$\begin{aligned}\mid V_{ij}(K,\mathbf{R})\mid^2 &= \frac{\omega^6}{16c^6\pi^2\epsilon_0^2}\left|\kappa_3\left(\frac{c^3}{\omega^3R^3}-\frac{ic^2}{\omega^2R^2}\right)-\frac{\kappa_1 c}{\omega R}\right|^2\\ &= \frac{\omega^6}{16c^6\pi^2\epsilon_0^2}\left(\kappa_3^2\frac{c^6}{\omega^6R^6}+(\kappa_3^2-2\kappa_1\kappa_3)\frac{c^4}{\omega^4R^4}+\kappa_1^2\frac{c^2}{\omega^2R^2}\right)\\ &= \frac{\omega^6}{16c^6\pi^2\epsilon_0^2}g(\omega,\mathbf{R}),\end{aligned}\tag{4.39}$$

where $g(\omega,\mathbf{R})$ is denoted as the excitation transfer function. The transition rate obtained using the QED formulation from Eq 4.38 is set equal with a general formula from Förster theory [71] to determine the proper normalization constants

$$\begin{aligned}\int_0^\infty\frac{\omega^6}{8c^6\hbar\pi\epsilon_0^2}\Psi_D(\omega)\Psi_A(\omega)g(\omega,\mathbf{R})d\omega &= \frac{9}{8\pi c^2\tau_D}\int_0^\infty f_D(\omega)f_A(\omega)\omega^2g(\omega,\mathbf{R})d\omega\\ \int_0^\infty\underbrace{\frac{\omega^4}{9c^4\hbar\pi\epsilon_0^2}}_{A(\omega)}\underbrace{\tau_D\Psi_D(\omega)}_{F_D(\omega)}\underbrace{\Psi_A(\omega)}_{\sigma_A(\omega)}g(\omega,\mathbf{R})d\omega &= \int_0^\infty f_D(\omega)f_A(\omega)g(\omega,\mathbf{R})d\omega,\end{aligned}\tag{4.40}$$

where $\Psi_D(\omega)$ and $\Psi_A(\omega)$ are corresponding contributions of donor and acceptor in Eq. 4.38. Now the donor emission spectrum and acceptor absorption cross-section

can be defined as

$$\sigma_A(\omega) = \frac{\omega^2 \mu_A^2}{3\epsilon_0 c^2 \sqrt{\pi\hbar}} \sum_{m,p} \rho_A^{(m)} \mid \langle \varphi_{A^*}^{(p)} | \varphi_A^{(m)} \rangle \mid^2 \delta(e_{A_M} - e_{A_p^*} + \hbar\omega) \tag{4.41}$$

$$F_D(\omega) = \frac{\omega^2 \mu_D^2}{3\epsilon_0 c^2 \sqrt{\pi\hbar}} \sum_{n,r} \rho_D^{(m)} \mid \langle \varphi_D^{(r)} | \varphi_{D^*}^{(n)} \rangle \mid^2 \delta(e_{D_n^*} - e_{D_r} - \hbar\omega)\,. \tag{4.42}$$

The entities $\langle \varphi_{A^*}^{(p)} | \varphi_A^{(m)} \rangle$ and $\langle \varphi_D^{(r)} | \varphi_{D^*}^{(n)} \rangle$ can be identified as the Frank-Condon factors of the acceptor and donor respectively. With the defined variables, the transfer rate is

$$\Gamma_{DA} = \frac{9}{8\pi c^2 \tau_D} \int_0^\infty F_D(\omega) \sigma_A(\omega) \omega^2 g(\omega, \mathbf{R}) d\omega\,. \tag{4.43}$$

If we examine the energy transfer in the near zone ($KR \ll 1$), the excitation transfer function in Eq. 4.39 becomes

$$\begin{aligned} g(\omega, \mathbf{R}) &= \left( \kappa_3^2 \frac{c^6}{\omega^6 R^6} + (\kappa_3^2 - 2\kappa_1\kappa_3) \frac{c^4}{\omega^4 R^4} + \kappa_1^2 \frac{c^2}{\omega^2 R^2} \right) \\ &\approx \kappa_3^2 \frac{c^6}{\omega^6 R^6}\,, \end{aligned} \tag{4.44}$$

and Eq. 4.43 is reduced to

$$\Gamma_{DA} = \frac{9 c^4 \kappa_3^2}{8\pi \tau_D R^6} \int_0^\infty \frac{F_D(\omega)\sigma_A(\omega)}{\omega^4} d\omega\,. \tag{4.45}$$

This is exactly the same equation as Eq. 4.12, which was obtained by the classical treatment in vacuum, i.e, $n \approx 1$. In the far field ($KR \gg 1$) the excitation transfer function in Eq. 4.39 becomes

$$g(\omega, \mathbf{R}) \approx \kappa_1^2 \frac{c^2}{\omega^2 R^2}\,, \tag{4.46}$$

and Eq. 4.43 is reduced to

$$\Gamma_{DA} = \frac{9\kappa_1^2}{8\pi \tau_D R^2} \int_0^\infty F_D(\omega) \sigma_A(\omega) d\omega\,. \tag{4.47}$$

With the help of QED a unified theory of energy transfer can be developed. The results given by QED prove that the radiationless and the radiative processes are based exactly on the same physical process. The only difference between these processes lies in the interaction distance between the donor and acceptor. Furthermore, different interaction distances are enough to yield totally different orientational behaviour in near and farfield.

Another interesting phenomenon associated in the resonance energy transfer is called the surface energy transfer (SET), in which either the donor or acceptor is a surface, *e.g.*, a quantum well. In this case the donor-to-acceptor separation distance has a inverse 4th power dependence, hence enabling much longer interaction distances between the donor and acceptor. [57]

Altogether, resonance energy transfer is a crucial intermolecular excitation transfer mechanism in biological and synthetic systems. For example, it plays a substantial role as a conduction mechanism in conductive polymers, which are used to fabricate organic light emitting diodes (OLED) or polymer solar cells. [10]

## 4.3 Orientational aspects

As found out in the previous sections, the energy transfer depends also from the orientational factor $\kappa$, which is dependent on three variables. These variables were defined previously in the Förster orientation factor from Eq. 4.6 as

$$\kappa = \vec{n}_A \cdot \vec{n}_D - 3(\vec{n}_R \cdot \vec{n}_D)(\vec{n}_R \cdot \vec{n}_R)\,,$$

where $\vec{n}_D$ is the unit vector along the emission transition moment of the donor, $\vec{n}_A$ is the unit vector along the absorption transition moment of the acceptor and $\vec{n}_r$ is the unit vector along a line, which is a line drawn from the centers of $D$ to $A$. This is further illustrated in Fig. 4.4.

As seen in the Section 4.2, the orientational factors are different in the near, intermediate and far zones. This leads to a completely different fluorescence depolarization behaviour in these three cases. For the Förster energy transfer, the transfer depends only weakly on the average mutual orientation of the donor and acceptor. This is the reason for the considerable reduction (1/25) of fluorescence anisotrophy following the energy transfer in isotropic or randomly oriented systems. Photon reabsorption is even seven times greater in the raditionless case, when compared to the raditiative transfer. Instead in the far zone, the energy transfer between molecules with parallel transition dipoles is preferred leading to a smaller loss of polarization in a randomly oriented system. [71]

There exists three common ways to express $\kappa^2$ as a function of various angles related

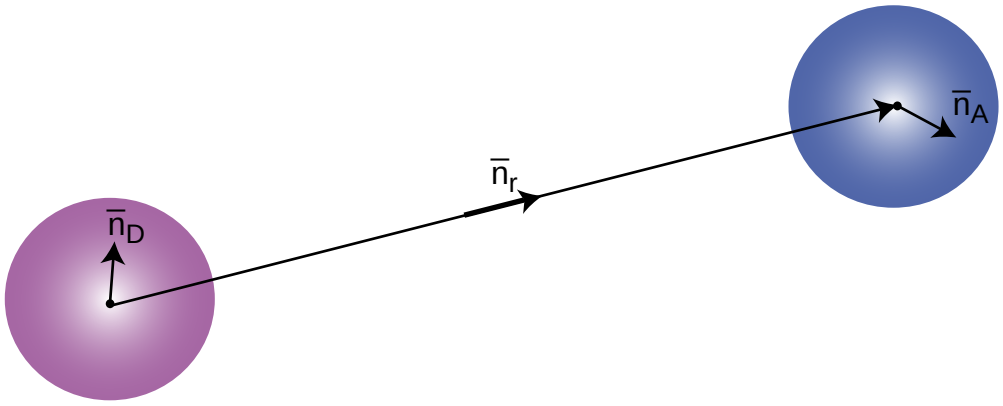


Figure 4.4: The three unit vectors $\vec{n}_D$, $\vec{n}_A$ and $\vec{n}_r$.

to the orientation of the molecules further illustrated in Fig. 4.5:

$$\kappa^2 = \big(\cos(\theta_T) - 3\cos(\theta_D)\cos(\theta_A)\big)^2 \tag{4.48}$$

$$\kappa^2 = \big(\sin(\theta_D)\sin(\theta_A)\cos(\varphi) - 2\cos(\theta_D)\cos(\theta_A)\big)^2 \tag{4.49}$$

$$\kappa^2 = \cos^2(\omega)\big(1 + 3\cos^2(\theta_D)\big)^2 . \tag{4.50}$$

The angle between $\vec{n}_D$ and $\vec{n}_r$ is $\theta_D$ and the same logic applies to the angle $\theta_A$. $\theta_T$ corresponds to the angle between $\vec{n}_D$ and $\vec{n}_A$. $\varphi$ is the angle between the projections of $\vec{n}_D$ and $\vec{n}_A$ on a plane perpendicular to $\vec{n}_r$. $\omega$ is the angle between $\vec{n}_A$ and the electric dipole field induced by the donor transition moment. These vectors and their angles are further illustrated in Fig. 4.5. The highest value that $\kappa^2$ can attain

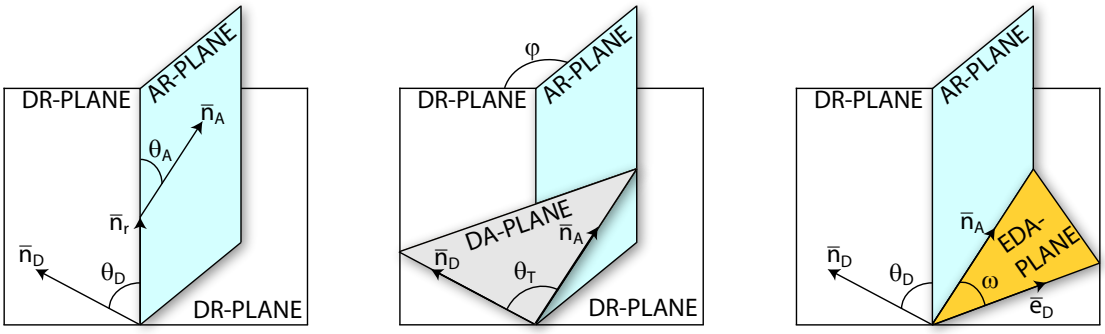


Figure 4.5: A figure illustrating the different polar angles and planes associated in RET. Picture modified from [59].

is 4, which occurs if both $\vec{n}_D$ and $\vec{n}_A$ are paraller or antiparaller to $\vec{n}_r$. The lowest value is 0, which corresponds to a situation, where $\vec{n}_A$ is perpendicular to the electric field produced by the donor (or vice versa). The case $\kappa^2 = 4$ can only occur in a

few ways, but $\kappa^2 = 0$ can be realized in an infinite number of ways. Straighforward calculation of the rotational average from the Eq. 4.50 yields the value 2/3, since the average value of $\cos^2$ taken from a polar angle is 1/3.

That is often the reason why $\kappa^2$ is replaced by the value of 2/3 in scientific studies, but this is justified only when the chromophores are spherical, or behave like a sphere because they rapidly diffuse through all possible orientations. If the chromophores are not rapidly diffusing or diffusing through a limited set of orientations, this approximation can lead to significant errors. [72]

# 5 Methods

## 5.1 Ultraviolet-visible spectroscopy

Ultraviolet-visible (UV-Vis) spectroscopy refers to a technique to measure absorption in the ultraviolet-visible-near infrared (UV-Vis-NIR) spectral range. This is a standard technique widely used in chemistry and material science. The principle of this method is very straightforward. As the light propagates through the sample it attenuates, which is then measured. The attenuation can be described with the help of the Beer-Lambert law, which states that the absorptivity of the sample can be expressed as

$$A = \epsilon c l \,, \tag{5.1}$$

where $\epsilon$ is the molar absorption coefficient, $c$ is the concentration and $l$ is the optical path of the light within the sample.

Figure 5.1 shows a schematic presentation of a two beam UV-Vis spectrometer used to measure the samples. In the absorption measurements a commercial UV-Vis spectrometer Lambda 950 manufactured by Perkin-Elmer was employed. As

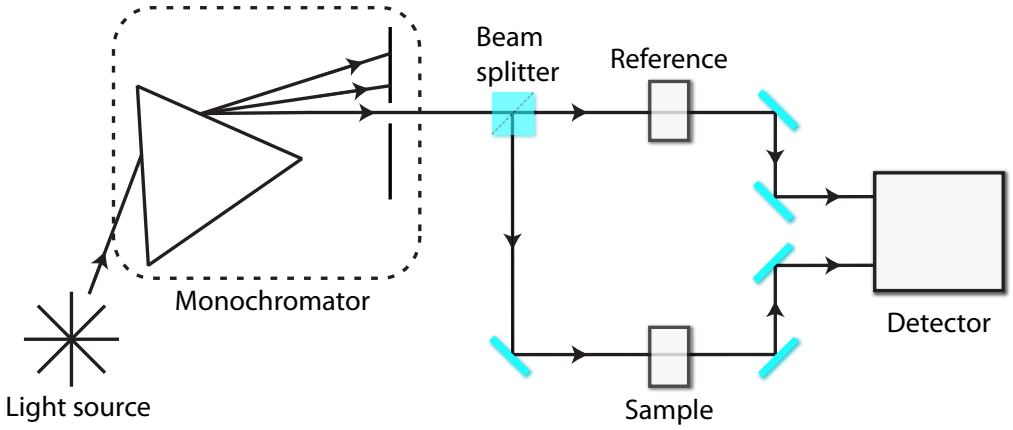


Figure 5.1: A schematic presentation of a two beam UV-Vis spectrometer used in this thesis.

the light source, Lambda 950 spectrometer uses deuterium and tungsten-halogen lamps that are prealigned and focused. These two lamps cover the wavelength range between 175 - 3300 nm. The deuterium lamp is used in the UV range and tungsten-halogen in the Vis-NIR range. The light from the lamps is directed to a holographic grating monochromator, which has 1440 lines/mm for UV/Vis and 360 lines/mm for NIR. The light emerging from the monochromator is shaped and split into two beams. One of the beams is directed to the sample and another one to the reference. The spectrometer has two detectors for enhanced sensitivity in different wavelength ranges. A photomultiplier tube (PMT) is used for the entire UV/Vis

wavelength range and a Peltier-cooled PbS detector for the NIR wavelength range. The full intensity and dark baselines were measured before the actual measurements and used to calibrate and correct the measured data.

The absorption was measured from solution and solid-state samples. As the reference sample, a quartz cuvette filled with solvent and a cleaned microscope glass slide were employed in the measurements.

## 5.2 Photoluminescence spectroscopy

Photoluminesce spectroscopy (PL) is a widely used non-invasive, non-destructive optical characterization method especially suitable for semiconductors. PL spectroscopy is qualitive measurement technique, and thus does not provide exact information. In PL the sample is irradiated by a light beam (usually a laser), which is used to excite electrons in the sample. For PL to yield useful information about the sample electrons should return from the excited state to the ground state radiatively, *e.g.*, by emitting a photon. Electrons can also return to the ground state non-raditiatively, in which case the information is lost. If the sample undergoes internal transitions before emitting the photon, the resulting signal is termed as fluorescence (see Chapter 2).

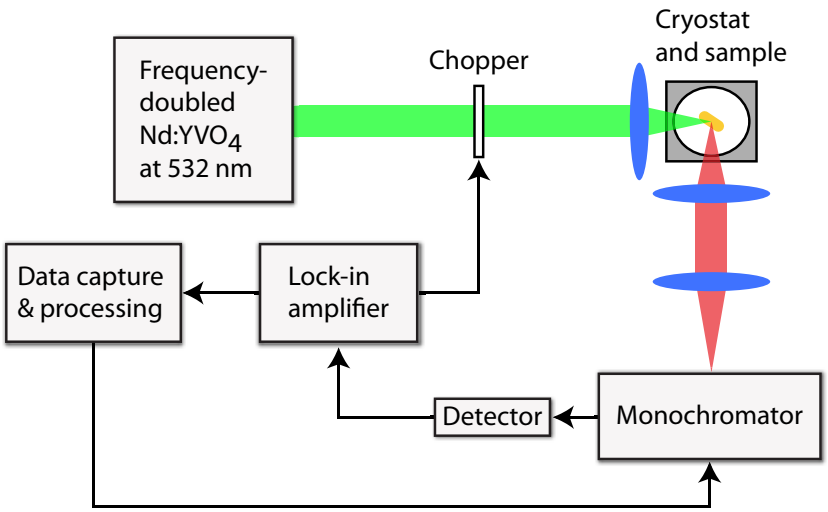


Figure 5.2: Schematic diagram of the setup used in CW measurements.

PL measurements can be done in continuous wave (CW) or time-resolved (TR) arrangements. CW measurements provide luminescence spectra, which can yield detailed information about the magnitude of the band gap, structure of the energy levels, quality of the crystalline structure and concentration and identification of impurity atoms. TR measurements use pulses of light to probe the sample providing information about the relaxation dynamics of the material. TRPL is extremely useful to determine the lifetimes of the minority carriers. [78]

The fluorescence of the polymer-dye complexes was measured with a commercial fluorometer Varian Cary Ecplipse. The fluorometer uses a preligned and focused Xenon flash lamp and as a detector a PMT. The PMT voltage was 800 V and the monochromator entrance and exit slits were 5 nm in all the measurements. For the passivation and the functionalization measurements different equipment was used and this is described in more detail below.

Figure 5.2 shows a schematic diagram of the CW measurement setup utilized in this thesis. As a light source, a 532 nm frequency-doubled Nd:$YVO_4$ laser was used to irridiate the sample. A chopper connected to the lock-in amplifier was placed in front of the sample to reduce noise of the PL signal. The germanium detector was cooled down using liquid nitrogen for the same reason. For data capture standard lock-in techniques were utilized. Focusing optics were used to focuse the incident light to the sample. The PL signal obtained from the sample was collimated using collection optics and dispersed using a monochromator. A typical power used to irradiate the sample was ca. 5 mW.

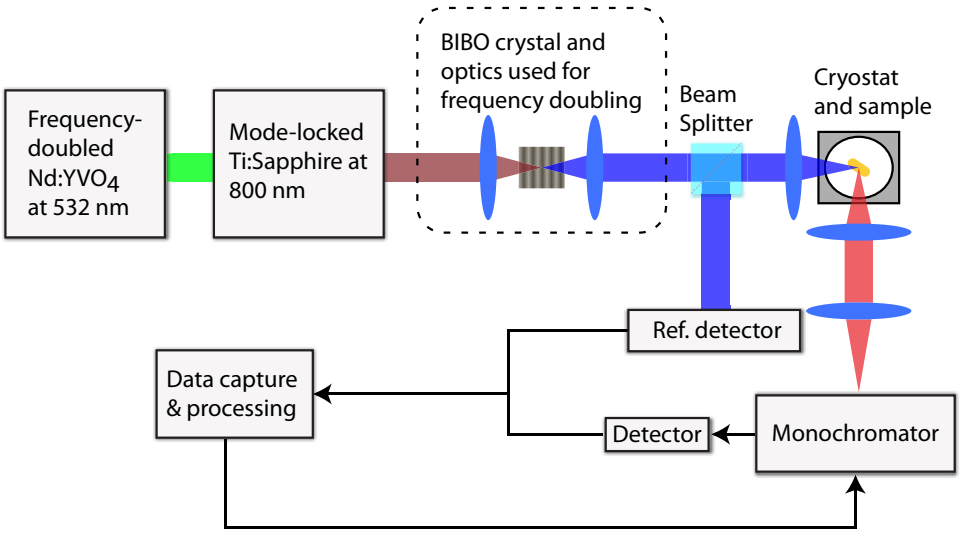


Figure 5.3: Schematic diagram of the setup used in time-resolved photoluminesce measurements.

The schematic diagram used in the time-resolved PL (TRPL) measurements is shown in Fig. 5.3. The 532 nm wavelength from the frequency doubled Nd:$YVO_4$ laser was used to pump the mode-locked Ti:Sapphire laser. 800 nm pulses generated by the Ti:Sapphire were frequency-doubled to 400 nm using an optically nonlinear bismuth triborate (BIBO) crystal. 400 nm wavelength corresponds relatively well to the Soret absorption band of Chls. The pulse repetition rate of the Ti:Sapphire was 76 MHz. The sample was placed inside a closed-cycle helium cryostat, which had temperature range of 9-350 K. Also as in the CW setup, similar collection optics were used to obtain the TRPL signal from the sample.

# 6 Materials

## 6.1 The fabrication of Zn-$3^1$-OH-*pyro a*

The process starts by extracting chlorophyll molecules from sprirulina algae, which contains only Chl *a*. Extraction can also be done from other various plants, *e.g.*, spinach, but these sources can also contain Chl *b*. The extraction is done in a 1:1 solution of acetone ($(CH_3)_2CO$) and methanol ($CH_3OH$ or MeOH), which is left to react for 3 days. This will destroy the cellular-wall and elutes Chl *a* into the organic solvent. Also the central metal Mg is lost in this process. The end product will be filtered through a glass-sinter couple of times, which removes most of the extra organic material, but preserves the Chl molecules. The remaining solvent is vaporized by a rotary evaporator. In Fig. 6.1 this procedure stands for step 1.

Step 2 consists of transesterification and purifying procedures. In the transesterification process the phytol tail is removed and replaced by a methylesther. This can be achieved by diluting the isolated Chl *a* in a 5% solution of sulphuric acid ($H_2SO_4$) and methanol. The solution is left in dark for two days. After the trans-

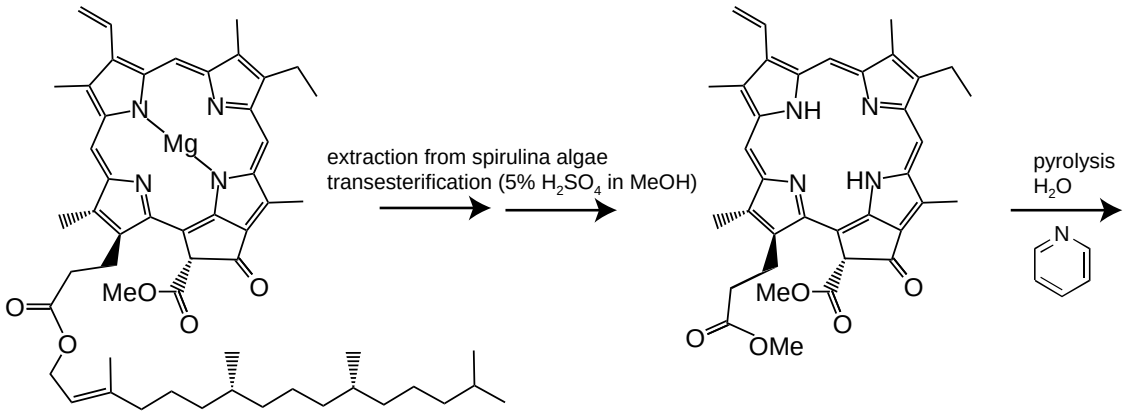


Figure 6.1: A schematic illustration of the Chl *a* extraction, transesterification and purifying to create Pheo *a* from spirulina algae using steps 1 and 2. The abbreviation and name of the compound are found below the corresponding molecule.

esterification, the solution is diluted with distilled water and then neutralized with saturated sodium bicarbonate ($NaHCO_3$). Resulting solution is then eluated to dichloromethane ($CH_2Cl_2$ or DCM) to form an organic phase, which is then washed with water and saturated sodium chloride (NaCl) solution. This procedure is repeated a couple of times. The solution is dried by using sodium sulfate ($Na_2SO_4$), which efficiently absorbs water from the solution. Sodium sulfate is left to absorb water for roughly an hour. After that, sodium sulfate is filtered off from the solution and remaining solvents evaporated. Next, all unwanted organic material

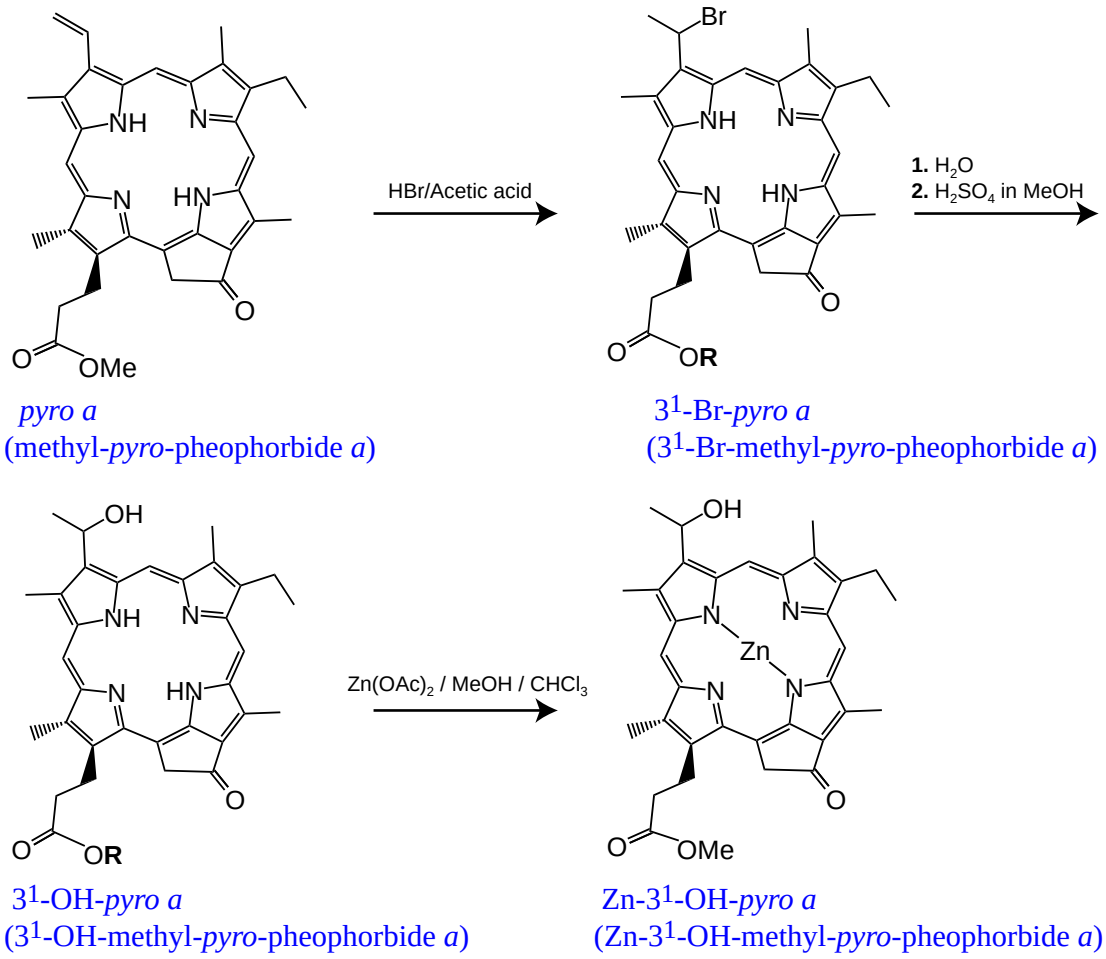


Figure 6.2: The schematic illustration of modification of peripheral substituents and bonding of Zn central metal using steps 3,4,5 and 6. The abbreviation and name of the compound are found below the corresponding molecule

(carotenoids, lipids) are filtered away from the solution. This is achieved using flash column chromatography, where the material is dissolved into DCM and then precipitated with hexane ($C_6H_{14}$). This process is repeated as many times as required to achieve wanted purity. At this point, the solution should contain only Pheo *a* and the purity of the solution was analyzed using NMR spectroscopy. So as a summary, in step 2 transesterification, neutralization and purification are performed, which results in Pheo *a* presented in Fig. 6.1.

The purpose of steps 3,4 and 5 is to modify the peripheral substituents. Bonding of Zn as the central metal is performed in step 6. The modifying process starts with the third step, which is called pyrolysis. Here $COOCH_3$ in C-$13^2\beta$ is completely removed. This is achieved using water and pyridine solution.

In the fourth step the vinyl group $-CH{=}CH_2$ in C-3 is modified making it two branched. These new branches are named as C-$3^1$ and C-$3^2$. This is achieved

by a solution of hydrobromic acid (HBr) and acetic acid known as ethanoic acid ($CH_3COOH$). As a consequence, a bromine atom is attached to the position C-3[1] as shown in Fig. 6.2. Since HBr is very poisonous and gases out easily, this reaction has to be done under argon atmosphere. Another reason for the use of argon is to remove the possibility of water contaminating the sample. The solution is warmed using a external heater and enveloped in aluminum foil to reduce the exposure for light. Naturally, after this reaction a neutralization is required. Furthermore, this step also affects the methane in position R-17. From NMR data, it was noticed that the group in C-17 can be either methane or hydrogen. Hence the group in R-17 is marked as **R** as in Fig. 6.2 .

Step 5 consists of two processes. In the first process, the bromine is removed from position C-3[1] and replaced by the hydroxyl group OH. This can be achieved easily by water, and can be done after the neutralization process. The next process is to remove the hydrogen from the position C-17 and replace it with methane. This is attained by using sulphuric acid and methanol. After this the solution has to be neutralized and the solution vaporized. In step 6, a solution of zinc acetate ($Zn(OA)_2$), MeOH and DCM is used to bond Zn as the central metal.

## 6.2 Passivation and functionalization of GaAs surface

Gallium arsenide (GaAs) has a native oxide ranging from $20 - 30$ Å. This oxide is formed spontaneously and relatively fast, when GaAs surface is in contact with atmospheric oxygen [73]. Althought the oxide protects the GaAs surface from additional oxidation and contaminants, it also promotes high density of surface states. These surface states pin the surface Fermi level near the middle of the bandgap providing a pathway for the minority carries to non-radiatively relaxate. [74] To prevent these adverse effects passivation of the surface is required.

A relatively easy method to passivate the GaAs surface can be achieved chemically by sulphur or with thiols (R−SH). In both cases the passivation occurs when sulphur is covelently bonded with either As or Ga atoms thus reducing the amount of dangling bonds. In addition to sulphur passivated surfaces, thiols also give the possibility to functionalize surface. Functionalized surfaces can be used, *e.g.*, to immobilize target species onto the surface. [75–77] In our experiments ⟨100⟩ ori-

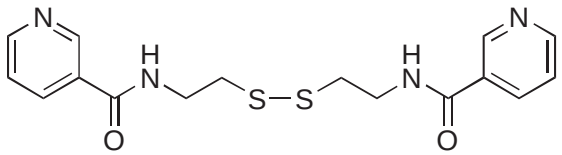


Figure 6.3: N,N'-(2,2'-disulfanediylbis(ethane-2,1-diyl))dinicotinamide.

ented GaAs substrates were employed. This type of surface is terminated either with Ga or As atoms. The procedure starts by removing the native oxide in a bath

of hydrochloric acid (HCl) for 3 minutes. The substrate is then washed two times in distilled water to remove the acid residues. After this, the etched substrate is immersed into a thiolate solution containing nicotine acid derivate shown in Fig. 6.3. In the solution, the S−S-bonds in the nicotine acid break down allowing the thiols to bond with the Ga/As atoms. Figure 6.4 shows a schematical presentation of the thiol functionalized GaAs surface.

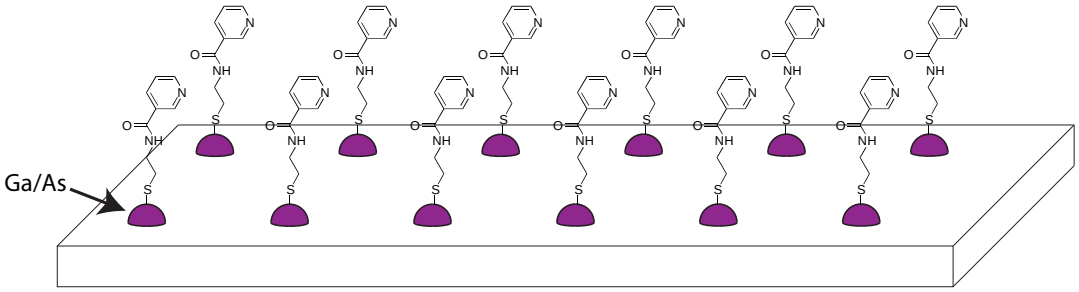


Figure 6.4: The surface after the immersion into the thiolate solution. The sulphur atom covalently bonds the Ga or As atoms in the surface, while pyridine efficiently coordinates with the Zn-3$^1$-OH-*pyro a* .

The quality of the passivation is observed using PL spectroscopy. The PL signal is generated from the radiative recombinations of the minority carriers. Recombination of the minority carriers can be roughly divided into bulk and surface recombinations. A succesfull passivation decreases the amount of surface states. This in turn decreases the rate of surface recombinations, which increases the lifetime of the minority carriers. The effective lifetime of the minority carriers can be described by [78]

$$\frac{1}{\tau_{eff}} = \frac{1}{\tau_B} + \frac{1}{\tau_S}\,, \tag{6.1}$$

where $\tau_{eff}$ is observed lifetime, $\tau_B$ is the bulk recombination lifetime and $\tau_S$ the surface recombination lifetime.

## 6.3 Preparation of the polymer-dye complexes

The materials used in this thesis are shown in Fig. 6.5. As the host materials two polymers, Poly(4-vinylpyridine) (P4VP, Polysciences, $M_w$ = 5100) and poly(methyl methacrylate) (PMMA, Polysciences, $M_w$ = 5000), were used. As the guest molecules two zinc tetrapyrroles synthesized from Chl *a* were used. Also solvents dichrolomethane (DCM, Fluka, ≥0.99) and tetrahydrofuran (THF, Fluka, ≥0.99) were employed.

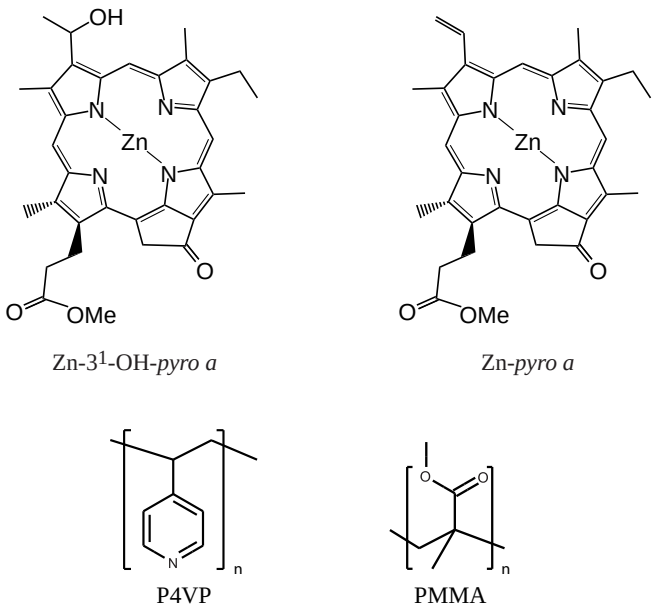


Figure 6.5: The chemical structures of the Zn-31-OH-*pyro a* and Zn-*pyro a* as well the polymers P4VP and PMMA

The fabrication steps of the Zn tetrapyrroles are presented in the Section 6.1. The only difference between these two chromophores is the missing hydroxyl group in position C-3$^1$ and thus the preparation of the Zn-*pyro a* (Pyro a) requires fewer steps than Zn-31-OH-*pyro a* (OH-Pyro a). Both chromophores were synthesized in Helsinki University by J. Helaja's group and used without additional purification.

In the fabrication of the polymer-dye complexes, the polymer and the dye were mixed together in solution. The samples were left to react for 24 hours in a dark room, while constantly stirring. The nomenclature used to name these complexes is polymer(dye)$_x$, where $x$ is the molar ratio between the one monomeric unit of a polymer and a dye molecule as in

$$\frac{n_{\text{polymer}}}{n_{\text{dye}}} = x\,. \tag{6.2}$$

This quantity is referred to as the complexation ratio.

Two series of samples were prepared. The first series included only P4VP(OH-Pyro a) complexes prepared in THF with the molar ratios of $x = 0.5$, $x = 0.1$, $x = 0.05$ and $x = 0.01$. The corresponding weight percents are presented in Table 6.1. The fabrication process started by diluting P4VP into THF to make a 5 wt. % stock solution. From this stock solution 1 wt. % and 0.5 wt. % solutions were made in order to facilitate the mixing process of the materials. The OH-Pyro a was diluted to a 0.1 wt. % stock solution.

Table 6.1: Series 1 - P4VP(OH-Pyro a)$_x$ complexes in THF. The complexation ratios and corresponding weight percent of the dye.

| **x** | Weight percent (wt. %) |
|---|---|
| 0.5 | 75.9 |
| 0.1 | 38.6 |
| 0.05 | 23 |
| 0.01 | 5.5 |

In the second series, PMMA(Pyro a) and P4VP(Pyro a) complexes were prepared in order to study the effect of the host material in the fluorescence properties of the dye. The second series had in total 14 samples that composed of following weight percents 1%, 2%, 4%, 6%, 8%, 10% and 12%. As the solvent DCM was used instead of THF, since PMMA is insoluble in THF. First, both the polymers were diluted in DCM to prepare a 5 wt. % stock solution. The dye, Pyro a was diluted in DCM to prepare 0.1 wt. % stock solution.

All samples were cast on a glass substrate by spin coating, where a two step program was utilized. In the first step, material was applied to the substrate and spinned with a rotation speed of 500/1000 revolutions per minute (rpm) for 40 seconds. The second step consisted of drying the solvent with a rotation speed of 5000 rpm for 30 seconds. In the first series the samples were spinned using two different rotation speeds to study the relationship between the rotation speed and the film quality and thickness. In the second series the samples were spinned only with 1000 rpm rotation speed. The thicknesses of the spinned films were analyzed by a Veeco Dektak 6M surface profilometer.

# 7 Results

## 7.1 Surface functionalization and passivation

The surface was functionalized with the procedure presented in Section 6.2. The effectivity of the passivation was observed via continuous wave and time resolved photoluminesce measurements. The setup employed in the measurements is presented in Section 5.2.

The results obtained for the continous wave measurements are shown in Figure 7.1. The maximum intensity for these graphs can be found in ca. 871 nm, which corresponds very well for the forbidden bandgap value for the GaAs ($E_g = 1.43$ eV).

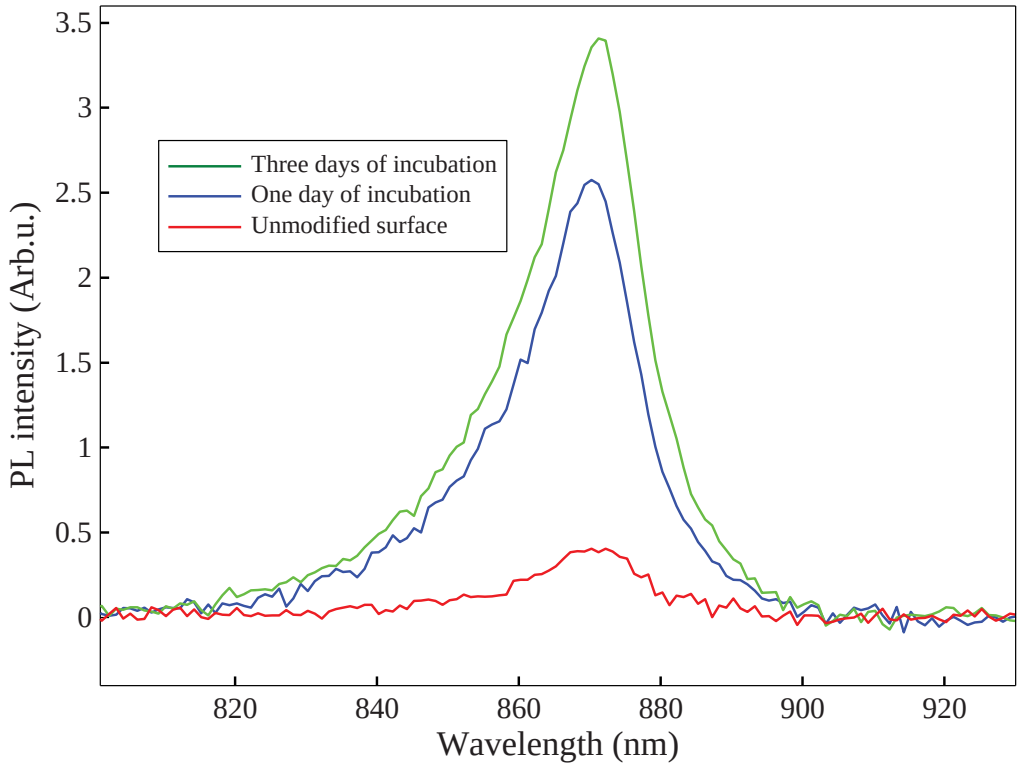


Figure 7.1: Continous wave photoluminescence measurement data for two surface passivated samples and one unmodified sample as a reference. Excitation wavelength was 532 nm.

For the unmodified surface the photoluminescence intensity is weak indicating that the non-radiative recombinations are the most prominent pathway in the relaxation process. However, the situation is radically changed after the passivation. This change can be clearly seen from Fig. 7.1, where the PL intensity is substantially increased in comparison to the unmodified surface. In addition, a notable difference

between the one and three day graphs can be distinguished. This could be an indication that one day of incubation is not enough to entirely passivate the whole surface, thus leaving non-bonded surface atoms after the incubation process. Moreover, the bond between the surface and the sulphur atoms has a covalent nature making the passivation very stable and resistant for most solvents.

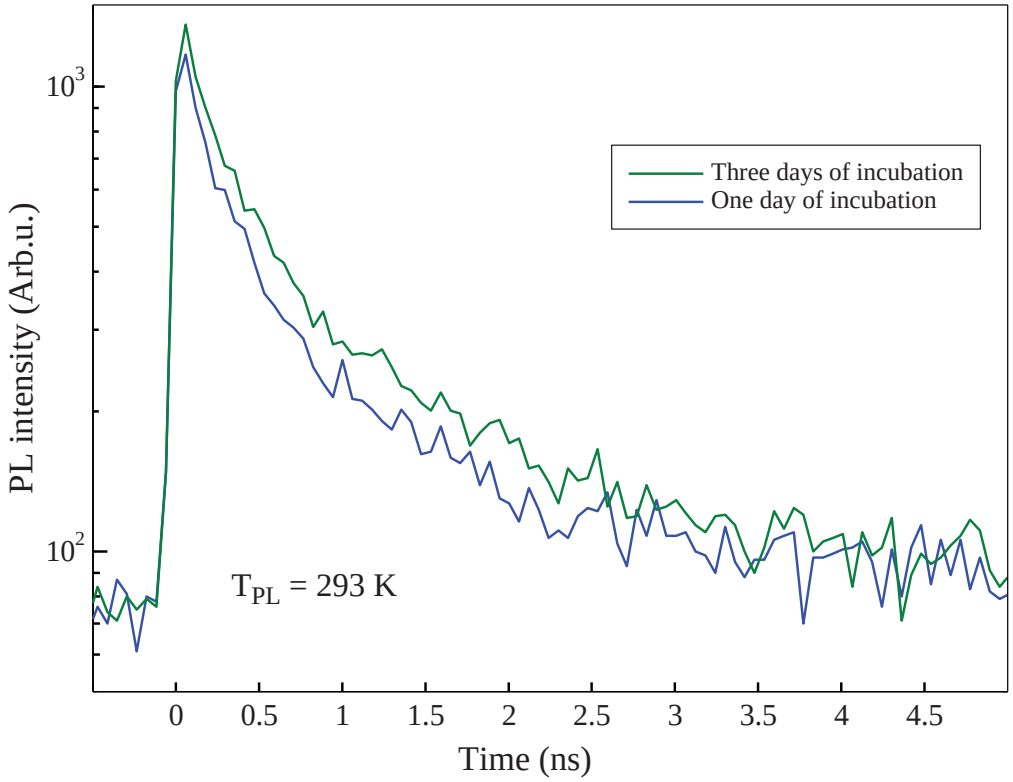


Figure 7.2: Room temperature time-resolved photoluminescence measurement data for two modified samples. The excitation wavelength was 532 nm and the PMT voltage was 2.5 kV.

The PL decay dynamics of the passivated surfaces were also investigated using time resolved photoluminescence measurements. These results are presented in Fig. 7.2. To analyze the time resolved data a double-exponential function was utilized and fitted to the measured data. The used double-expotential function was defined as

$$n(t) = A \exp\left(-\frac{t}{\tau_1}\right) + B \exp\left(-\frac{t}{\tau_2}\right) + C\,, \tag{7.1}$$

where A, B, and C are constants, whereas $\tau_1$ and $\tau_2$ are the fitting parameteres. The values of $\tau_1$ and $\tau_2$ given by the curve fitting procedure are listed in Table 7.1.

In accordance with the previous results, the improved performance of the surface can be detected also in the time-resolved measurements. The unmodified surface

gave no detectable signal when using 2.5 kV PMT voltage. Only for the treated surfaces a signal was detected. Again, the lifetimes of the minority carriers increase as a function of the incubation time. Therefore, it suffices to say that both of the continous wave and time-resolved measurements provide a thorough proof for a efficient passivation of the surface.

Table 7.1: Lifetimes obtained from the TRPL measurements of the surface functionalized samples.

| $\tau_1$ (ns) | $\tau_2$ (ns) |
|---|---|
| 0,6 | 4,9 |
| 0,3 | 3,4 |

## 7.2 OH-Pyro a aggregate

The optical properties of pure OH-Pyro a aggregates was studied in order to compare the results with the polymer-dye complexes. The samples were spin coated on top of a glass substrate from a 0.5 wt. % stock solution and characterized by UV-Vis absorption and photoluminescence measurements.

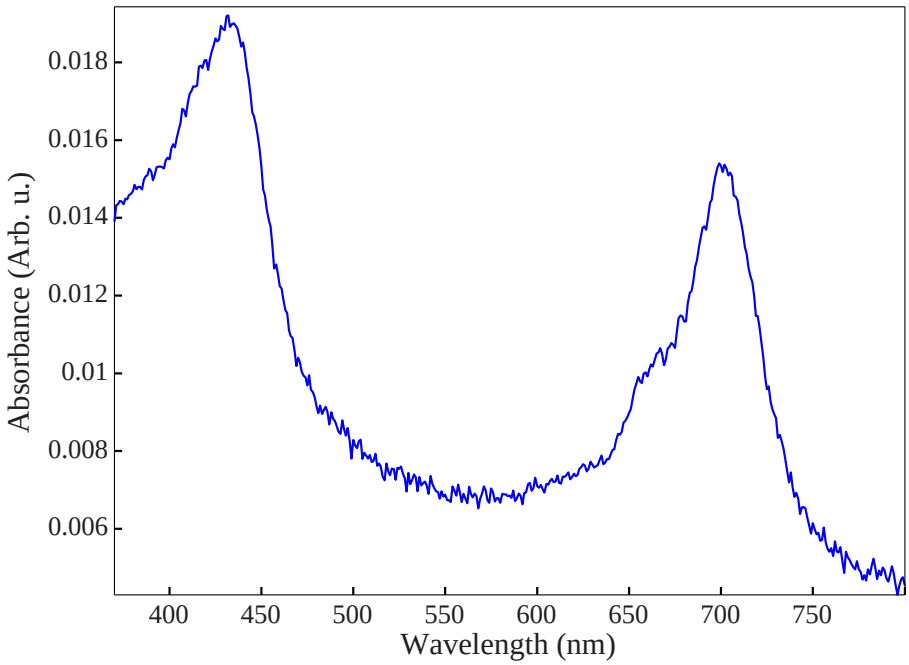


Figure 7.3: The absorption spectra of 0.5 wt. % OH-Pyro a spin coated on a glass substrate.

Figure 7.3 shows the absorption spectra of the OH-Pyro a aggregate spinned on a glass substrate. From the first glance one can notice that the peaks are broadened

enveloping the smaller details under them. Another important detail is a very strong red shift of the Q band. This peak has shifted to ca. 710 nm, whereas the monomer Q band peak lies in 660 nm. All of these details reveal that the OH-Pyro a molecules are in aggregated form and also that the aggregate is in amorphous state [41].

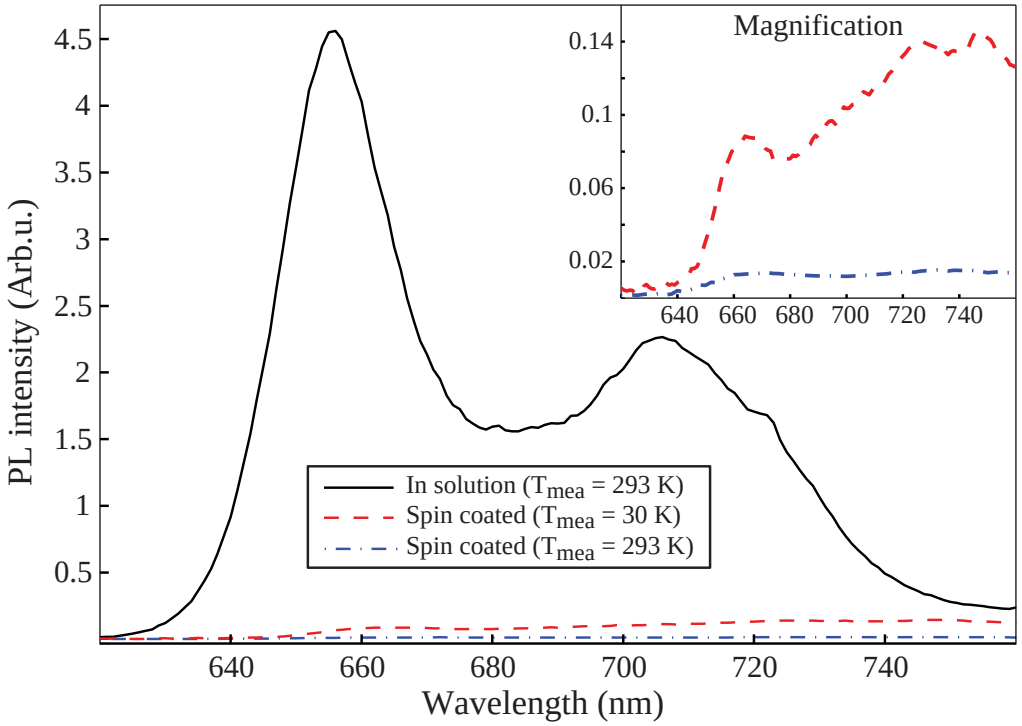


Figure 7.4: The photoluminescence spectra of 0.5 wt. % OH-Pyro a in THF solution and spin coated on a glass substrate. Excitation wavelength was 400 nm.

Figure 7.4 shows the results obtained from the photoluminescence measuremets. The CWPL measurements were done for two different samples: OH-Pyro a in solution and spin coated films on glass. In addition, the spin coated sample was measured in room temperature ($T_{\text{mea}}$ = 293 K) and in cryo temperature ($T_{\text{mea}}$ = 30 K). In Fig. 7.4, the spin coated sample exhibit insignificant fluorescence in comparison to molecules in a solution. Nevertheless, a magnified view of the graphs reveals two distinct peaks in the sample when measured in a cryo temperature. The values of these peaks are ca. 660 nm and 710-760 nm. The 660 nm peak corresponds to the $S_1 \rightarrow S_0$ transition and the broader peak around 710-760 nm could correspond to the aggregate enhanced $T_1 \rightarrow S_0$ transition. These same features are also observable in the data measured in the room temperature both the signal to noise ratio is much more worse.

## 7.3 Series 1: P4VP(OH-Pyro a)

The P4VP(OH-Pyro a) complexes were prepared as in Section 6.3 and spin coated on a glass substrate. The main purpose of this Series was to determine, if P4VP could act as an efficient host material preventing the aggregation of the chromophores. Furthermore, as the fluorescence properties of the aggregate were poor, it was required to know if these complexes could fluoresce at all.

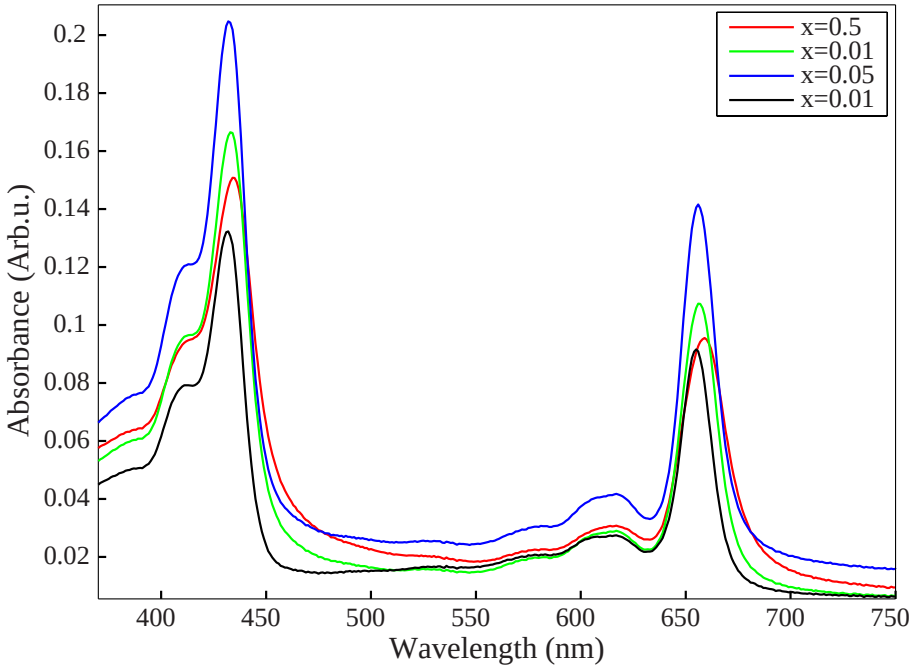


Figure 7.5: The absorption spectra of spin-coated P4VP(OH-Pyro a)$_x$-complexes. The spinner rotation speed was 500 rpm.

First, the samples were spinned using 500 rpm and 1000 rpm rotation speeds in order to study the resulting film thicknesses. The measured film thicknesses are shown in Table 7.2. Also, the absorption and fluorescence spectra were fitted using a fourth order Gaussian function given as

$$A(x) = \sum_{i=1}^{4} a_i \exp\left(-\frac{(x-b_1)^2}{c_1^2}\right) . \tag{7.2}$$

Using the first order derivative of Eq. 7.2 ($\frac{dA(x)}{dx}$), the emission and absorption frequencies were determined. These results are collected in the Table 7.2. However, for the weakest fluorescence signals the determination of the emission frequency proved to be impractical.

The absorption spectras are presented in Fig. 7.5 and Fig. 7.6. In all cases, the ab-

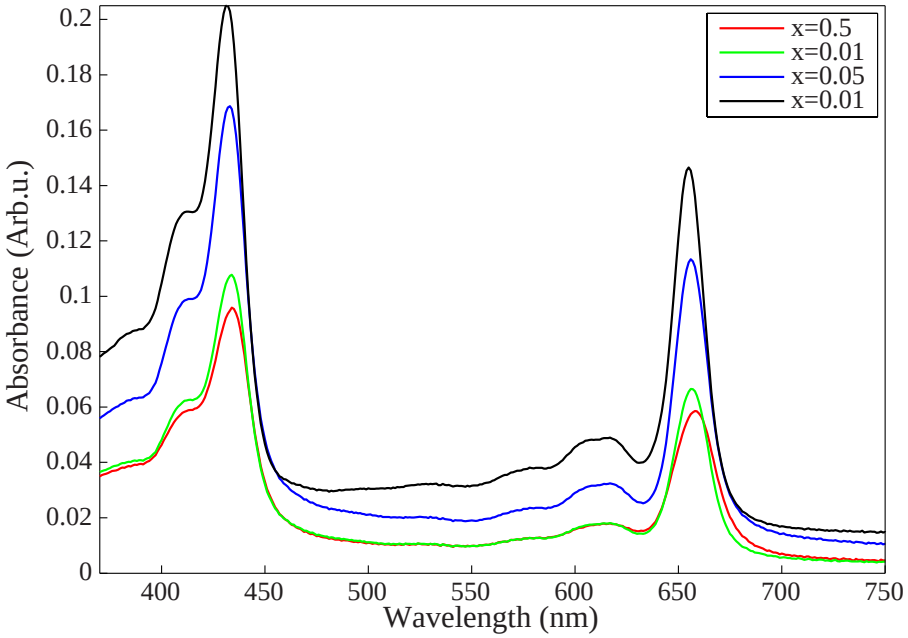


Figure 7.6: The absorption spectra of spin-coated P4VP(OH-Pyro a)$_x$-complexes. The spinner rotation speed was 1000 rpm.

Table 7.2: The measured physical and optical properties of the spin coated P4VP(OH-Pyro a) films.

| **Molar ratio** | **Thickness (nm)** | **Soret (nm)** | **Q (nm)** | **Emission (nm)** |
|---|---|---|---|---|
| **1000 rpm:** | | | | |
| 0.5 | 30 | 433.9 | 658.3 | - |
| 0.1 | 35 | 433.4 | 656.4 | 662 |
| 0.05 | 55 | 432.7 | 655.8 | 661.8 |
| 0.01 | 120 | 431.7 | 655 | 660.4 |
| **500 rpm:** | | | | |
| 0.5 | 20 | 434.5 | 658.9 | - |
| 0.1 | 37 | 433.3 | 656.5 | - |
| 0.05 | 125 | 432.3 | 655.9 | 663 |
| 0.01 | 205 | 431.4 | 655.0 | 660.2 |

sorption spectra resembles more monomeric than aggregate absorption. In addition, the aggregate peak around 710 nm is missing. These details demonstrate that P4VP efficiently coordinates with the OH-Pyro a molecules preventing aggregation. Furthermore, the absorption of the aggregate is much more weaker in comparison to the P4VP(OH-Pyro a) complexes, albeit the amount of absorbing chromophores lying in the light path is roughly equal. Therefore, this could indicate that the uncontrolled aggregation is also detrimental for the absorption properties of the substance.

From Table 7.2 it can be seen that the thickness of the film is increased as the dye concentration is decreased. Hence, the viscosity of the polymer-dye solution is proportional to the concentration of the dye. In most of the cases, the absorption is increased as the film thickness increases. The only exception for this case can be found in Fig. 7.5 for the $x = 0.01$, but a plausible result for this anomaly could originate from bad beam aligment in the measurement. Additionally, the films were thicker with 500 rpm rotation speed, but surprisingly the absorption was roughly the same. In addition, as the dye concentration decreases the peaks exhibit a

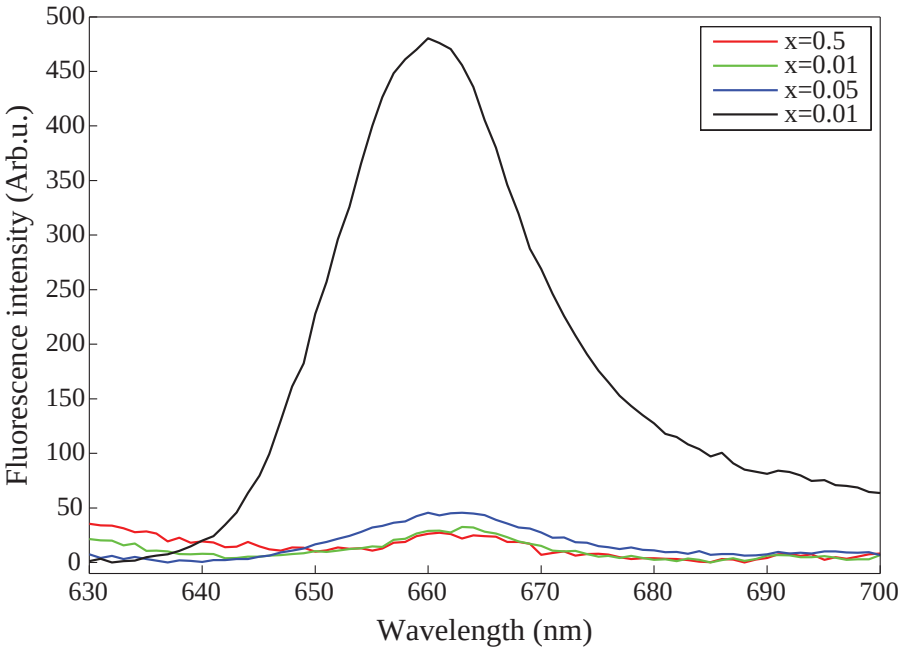


Figure 7.7: The fluorescence spectra of spin-coated P4VP(OH-Pyro a)$_x$-complexes. The spinner rotation speed was 500 rpm, excitation wavelength was 420 nm and PMT voltage 800 V.

blueshift indicating that the excitonic coupling between the chromophores weakens as depicted by Eq. 3.9. This is again very reasonable, since statistically the distance between the chromophores should increase with decreasing dye concentration.

Figure 7.7 and 7.8 show the measured fluorescence spectra of the spin coated samples. In the data a systematic error was present, which raised the signal bottom level. This was corrected by adjusting the zero level same for all the graphs. In both Figures, significant fluorescence signal can be detected only with the smallest dye concentration, *i.e.*, with $x = 0.01$. Other dye concentrations exhibit a minimal fluorescence signal, but this very small in comparison to the $x = 0.01$ case. In addition, the fluorescence signal detected from sample $x = 0.01$ is very strong compared to the values obtained in the literature [79,80]. These reported results utilize weight concentrations in the range of 0.5-2 wt. %. Therefore, P4VP(OH-Pyro a) complexes offer a very tempting possibility as a gain material for lasers.

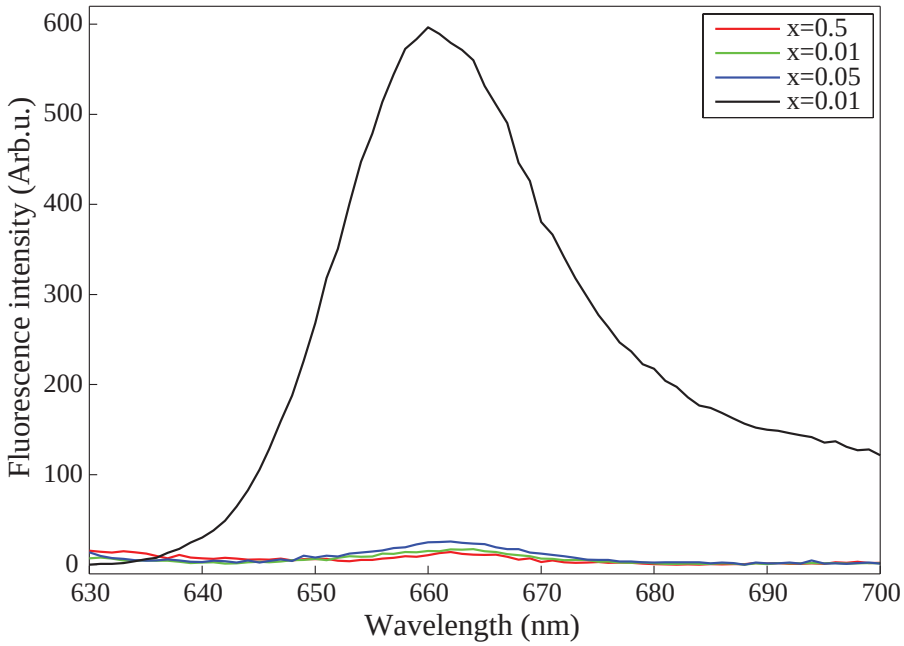


Figure 7.8: The fluorescence spectra of spin-coated P4VP(OH-Pyro a)$_x$-complexes. The spinner rotation speed was 1000 rpm, excitation wavelength was 420 nm and PMT voltage 800 V.

## 7.4 Series 2: P4VP(Pyro a) vs. PMMA(Pyro a)

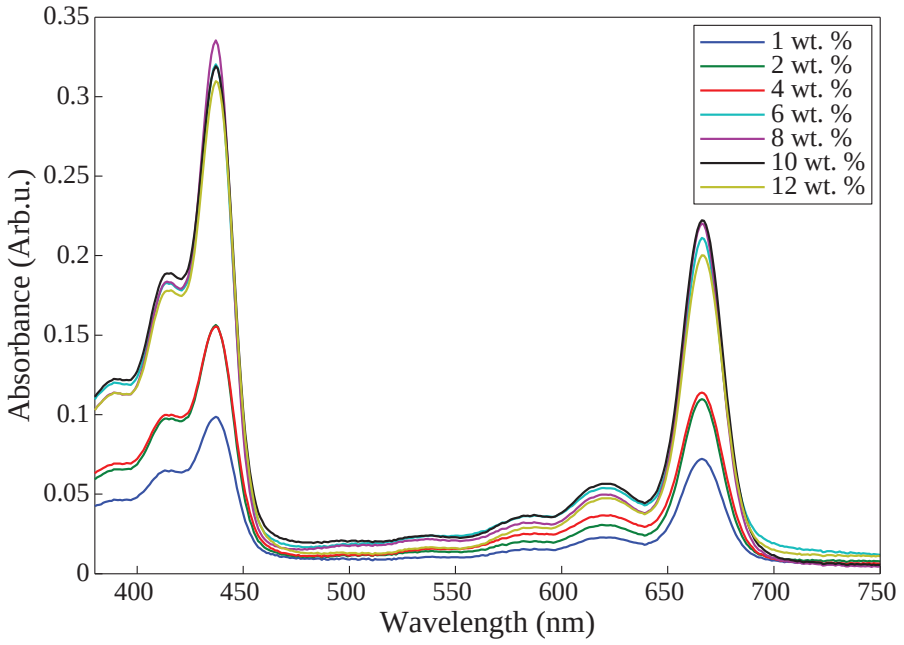


Figure 7.9: The absorption spectra of spin-coated P4VP(Pyro a)$_x$-complexes.

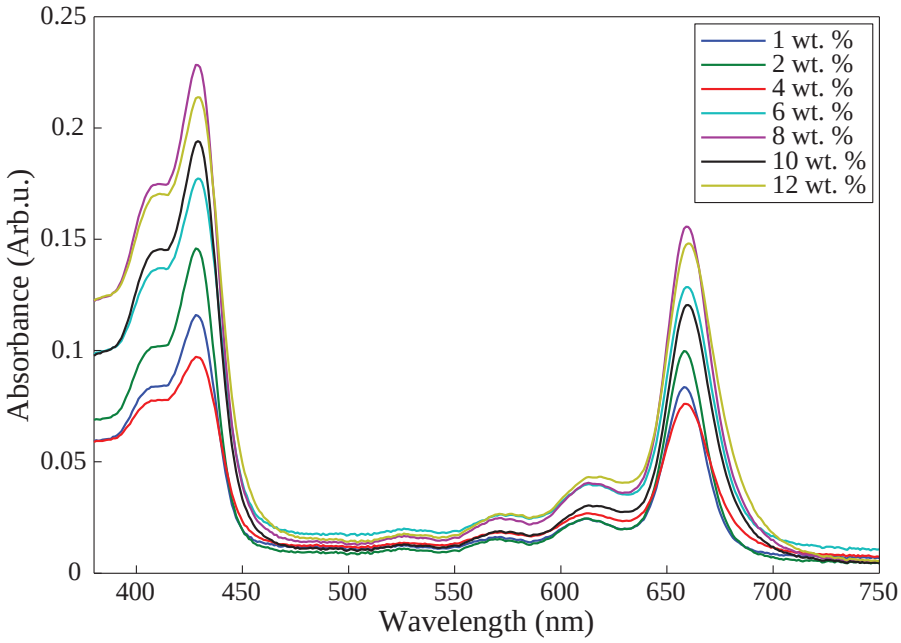


Figure 7.10: The absorption spectra of spin-coated PMMA(Pyro a)$_x$-complexes.

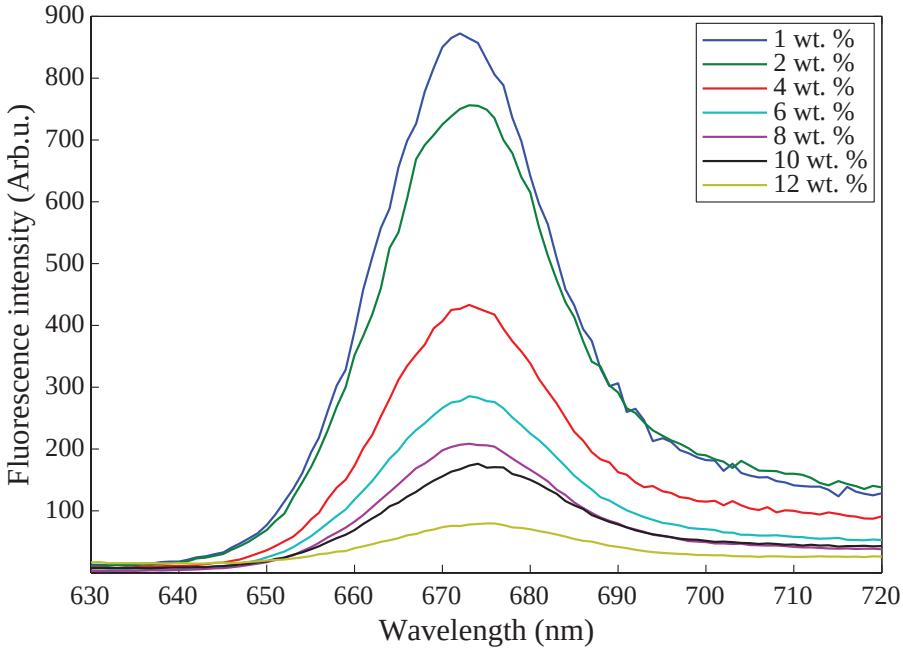


Figure 7.11: The fluorescence spectra of spin-coated P4VP(Pyro a)$_x$-complexes. Excitation wavelength was 435 nm and PMT voltage 800 V.

Both, PMMA and P4VP complexes were prepared as in Section 6.3 and spin coated on a glass substrate. The purpose of this Series was to compare the behaviour of

two different host materials. The hypothesis was that PMMA complexes should exhibit worse optical properties, since the coordination with the dye is more weaker. In addition, a different dye was utilized than in Series 1 in order to study, if the hydroxyl bond had any pronounced effect in the formation of the coordination bond between the dye and the molecule.

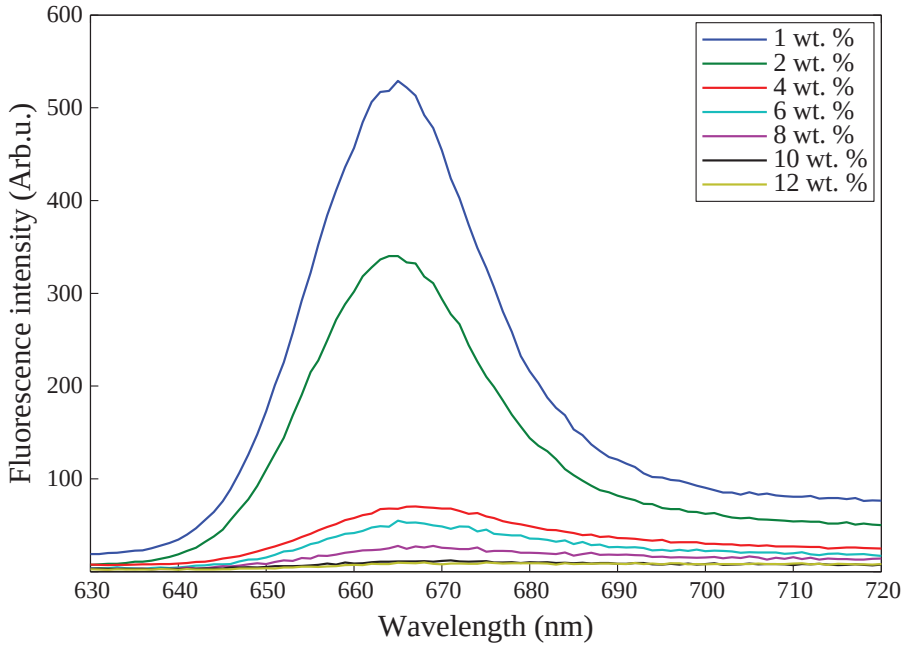


Figure 7.12: The fluorescence spectra of spin-coated PMMA(Pyro a)$_x$-complexes. Excitation wavelength was 435 nm and PMT voltage 800 V.

The absorption spectra of the P4VP(Pyro a) and PMMA(Pyro a) complexes is shown in Figs. 7.9 and 7.10 respectively. The Soret and Q absorption peaks were determined by fitting Eq. 7.2 as described earlier. Surprisingly, PMMA films do not exhibit any signs of aggregation. Somekind of sign of aggregation was expected, since the coordination bond between the carbonyl group of the polymer and the central metal of Pyro a is weak. However, the concentration of the dye is small, which could make the aggregation effects difficult to detect. Higher dye concentrations might be needed to demonstrate this effect.

Another interesting difference found in the P4VP absorption spectra in Fig. 7.9 is a very large (ca. 10 nm) redshift in comparison to PMMA(Pyro a) and P4VP(OH-Pyro a) complexes (Figs. 7.10, 7.5 and 7.6). Since position C-3[1] is situated relatively far from the macrocycle, removing the hydroxyl group should not have a large effect in the electronic properties of the molecule. This assumption is supported by the data obtained from the PMMA complexes, which do not exhibit any kind of red shift in comparison to P4VP(OH-Pyro a) complexes. The reason behind this redshift, could lie in the efficient coordination bond between the Zn and the

pyridine, since strong coordination of the central metal has been shown to affect the electronic structure of the macrocycle [20, 28]. To verify this a solvent spectra would be required. Also, additional measurements between OH-Pyro a and Pyro a chromophores could elucidate this phenomenon.

The fluorescence spectra of the P4VP(Pyro a) and PMMA(Pyro a) complexes are shown in Figs. 7.11 and 7.12 respectively. The fluorescence of the P4VP complexes is much stronger in all cases when compared to the PMMA complexes. Hence, even though the aggregation effects were not noticiable from the absorption spectra, fluorescence spectra clearly demonstrates the inferior performance of the PMMA as a host. Furtmermore, the observed redshift in the absorption spectra for the P4VP(Pyro a) complex, is also visible in the fluorescence spectra.

Table 7.3: Wavelengths of the absorption and emission peaks of the spinned P4VP(Pyro a) and PMMA(Pyro a) films.

| **Weight percent** | **Soret (nm)** | **Q (nm)** | **Emission (nm)** |
|---|---|---|---|
| **P4VP(Pyro a):** | | | |
| 1 wt. % | 436.9 | 666.1 | 672.3 |
| 2 wt. % | 437.2 | 666 | 673.6 |
| 4 wt. % | 437 | 666.1 | 673.1 |
| 6 wt. % | 436.9 | 666.3 | 673.7 |
| 8 wt. % | 437 | 666.1 | 673.3 |
| 10 wt. % | 437 | 666.4 | 674 |
| 12 wt. % | 437.3 | 666.6 | 674.3 |
| **PMMA(Pyro a):** | | | |
| 1 wt. % | 428.3 | 658.3 | 664.7 |
| 2 wt. % | 428.6 | 658.5 | 664.6 |
| 4 wt. % | 428.7 | 659 | 667.2 |
| 6 wt. % | 429.2 | 659.8 | 667.1 |
| 8 wt. % | 428.9 | 659.5 | 667.6 |
| 10 wt. % | 429 | 659.8 | 668.7 |
| 12 wt. % | 429.2 | 660.3 | - |

# 8 Conclusions

In this thesis, the first steps to integrate Zinc tetrapyrrole molecules with modern semiconductor devices are taken. This thesis introduces crucial concepts and properties required to understand the properties of molecular aggregates and guest-host materials. Also the underlying theory of energy transfer is presented. Althought, RET is a known phenomenon the information concerning the QED treatment is fragmented and obtaining a general view can be difficult. Hence, the author wanted to collect the available information and present it in a cohesive and understandable manner for others to study, and enjoy learning as much as I have.

The preliminary results demonstrated in this thesis appear promising. The envisioned device exploting the introduced concepts and results, could consist of AlGaAs/GaAs/AlGaAs quantum well with organic layer situated on top. Crucial factor in this device lies in the barrier thickess. Usually the barriers need to be atleast twice the thickness of the QW itself. If the barrier is not thick enough, the quantum confinement is not strong enough and tunneling of the electron out from the QW could occur. However, if the barrier is too thick, the coupling between the organic layer and the QW will not be sufficiently strong, since the energy transfer between a QW and a molecule has the characteristic $R^{-4}$ distance dependency. But with the developed passivation technique this problem might hopefully be circumvented, since it allows the fabrication of even thinner barriers exhibiting the same quantum confinement as the thicker counterparts.

The results from the passivation could be still investigated more thoroughly by scanning tunneling microscope (STM) or photoelectron spectroscopy (XPS). Especially, XPS could yield additional information about the bonding strenghts between the thiol and the Ga/As atoms. With the help of STM the pyridine molecules could be identified on top the surface. This could be used to identify the surface topography with an atomic resolution. In addition, the deposition of a Zn tetrapyrroles on to the functionalized surface appears to be intesting possibility, since the functionalized surface offers the possibility to deposit a monolayer of target molecules on top of the substrate. Therefore, this possibility will most likely be tested in future.

The fluorescence studies of the polymer-dye complexes could also be judged succesfull. With the help of supramolecular design, the optical properties of the chromophores can be drastically improved when compared to pure Zn tetrapyrrole aggregates. Hence, polymer-dye complexes seem to be the most prominent candidate in creating sufficient fluorescence in solid state. Furthermore, when comparing P4VP and PMMA with each other, P4VP is a much better host material for Zn tetrapyrroles. The underlying reason for this difference most probably lies in the efficient ligation between central metal and pyridine, which reduces the aggregation of the molecules.

PMMA is the most commonly used host material in solid state lasers and the rhodamine family molecules are the most employed fluorophores. However, as stated earlier the used dye concentrations are very small in comparison to the results ob-

tained in this thesis. Therefore, Zn tetrapyrroles and P4VP could offer new interesting possibilities in this area. In addition, the used Zn tetrapyrroles exhibit an ideal three-state system behaviour reducing the reabsorbtion effects present in rhodamine dyes. Furthermore, with a relative small modifications to the molecule the lasing wavelength can be changed offering the possibility for tailorability in the laser application. Finally, the fabrication process, *i.e.*, spin coating of the material on top of the substrate, is ideal for distributed feedback (DFB) lasers.

The pure aggregates exhibit peculiar and interesting properties, *e.g.*, self-assembly in larger supramolecular structures. These kind of assemblies could posses very rapid conduction mechanisms or even charge transfer as in their natural counterparts. In addition, combining these photosynthetic pigments with plasmonics could offer new sensor possibilities or waveguides. However, to monitor these effects requires a specilized tool, such as scanning near-field optical microscope (SNOM).

The results presented in this thesis will most likely be published in a peer reviewed journal, especially the work done with the fluorescent polymer-dye complexes. Next goal is to fabricate a proof of concept laser utilizing the earlier discussed benefits. The final aim of this reseach project is to developing a device, capable of collecting the excitation energy of the chromophores and transform it to electricity.

# A Derivation of the matrix element in the Fermi's Golden Rule

The one photon parts can be calculated using formulas 4.24, 4.25, 4.28, 4.33 and since $\langle D|\,\hat{\mu}(D)\,|D\rangle = 0$ and $\langle A|\,\hat{\mu}(A)\,|A\rangle = 0$, we obtain for $q = 1$

$$\begin{aligned}
\langle F|\,H_{\text{int}}\,|M_1\rangle &= \Big\langle\, |D\rangle\,|A^*\rangle\,|0\rangle \,\Big|\, -\epsilon_0^{-1}\hat{\mu}(A)\cdot\hat{d}^{\perp}(R_A) - \epsilon_0^{-1}\hat{\mu}(D)\cdot\hat{d}^{\perp}(R_D) \,\Big|\, |D\rangle\,|A\rangle\,|1\rangle \,\Big\rangle \\
&= -\epsilon_0^{-1}\,\langle A^*|\,\hat{\mu}(A)\,|A\rangle\cdot\langle 0|\,\hat{d}^{\perp}(R_A)\,|1\rangle \\
&= -i\sum_{\mathbf{k},\lambda}\left(\frac{\hbar ck}{2\epsilon_0 V}\right)^{1/2}\langle A^*|\,\hat{\mu}(A)\,|A\rangle\cdot\langle 0|\,\hat{e}_{\mathbf{k},\lambda}\hat{a}_{\mathbf{k},\lambda}e^{i\mathbf{k}\cdot\mathbf{R}} - \hat{e}^{-}_{\mathbf{k},\lambda}\hat{a}^{\dagger}_{\mathbf{k},\lambda}e^{-i\mathbf{k}\cdot\mathbf{R}}\,|1\rangle \\
&= -i\sum_{\mathbf{k},\lambda}\left(\frac{\hbar ck}{2\epsilon_0 V}\right)^{1/2}\langle A^*|\,\hat{\mu}(A)\,|A\rangle\,\Big(\langle 0|\,\hat{e}_{\mathbf{k},\lambda}\hat{a}_{\mathbf{k},\lambda}e^{i\mathbf{k}\cdot\mathbf{R_A}}\,|1\rangle - \langle 0|\,\hat{e}^{-}_{\mathbf{k},\lambda}\hat{a}^{\dagger}_{\mathbf{k},\lambda}e^{-i\mathbf{k}\cdot\mathbf{R_A}}\,|1\rangle\Big) \\
&= -i\sum_{\mathbf{k},\lambda}\left(\frac{\hbar ck}{2\epsilon_0 V}\right)^{1/2}\langle A^*|\,\hat{\mu}(A)\,|A\rangle\,\Big(\hat{e}_{\mathbf{k},\lambda}e^{i\mathbf{k}\cdot\mathbf{R_A}}\underbrace{\langle 0|\,\hat{a}_{\mathbf{k},\lambda}\,|1\rangle}_{\langle 0|0\rangle=1} - \hat{e}^{-}_{\mathbf{k},\lambda}e^{-i\mathbf{k}\cdot\mathbf{R_A}}\underbrace{\langle 0|\,\hat{a}^{\dagger}_{\mathbf{k},\lambda}\,|1\rangle}_{\langle 0|2\rangle=0}\Big) \\
&= -i\sum_{\mathbf{k},\lambda}\left(\frac{\hbar ck}{2\epsilon_0 V}\right)^{1/2}\mu_j^{\text{full}}(A)\hat{e}_{j,\mathbf{k},\lambda}e^{i\mathbf{k}\cdot\mathbf{R_A}}\,, \qquad\qquad (A.1)
\end{aligned}$$

and similarly

$$\begin{aligned}
\langle M_1|\,H_{\text{int}}\,|I\rangle &= \Big\langle\, |D\rangle\,|A\rangle\,|1\rangle \,\Big|\, -\epsilon_0^{-1}\hat{\mu}(A)\cdot\hat{d}^{\perp}(R_A) - \epsilon_0^{-1}\hat{\mu}(D)\cdot\hat{d}^{\perp}(R_D) \,\Big|\, |D^*\rangle\,|A\rangle\,|0\rangle \,\Big\rangle \\
&= -i\sum_{\mathbf{k},\lambda}\left(\frac{\hbar ck}{2\epsilon_0 V}\right)^{1/2}\langle D|\,\hat{\mu}(D)\,|D^*\rangle\,\Big(\langle 1|\,\hat{e}_{\mathbf{k},\lambda}\hat{a}_{\mathbf{k},\lambda}e^{i\mathbf{k}\cdot\mathbf{R_D}}\,|0\rangle - \langle 1|\,\hat{e}^{-}_{\mathbf{k},\lambda}\hat{a}^{\dagger}_{\mathbf{k},\lambda}e^{-i\mathbf{k}\cdot\mathbf{R_D}}\,|0\rangle\Big) \\
&= -i\sum_{\mathbf{k},\lambda}\left(\frac{\hbar ck}{2\epsilon_0 V}\right)^{1/2}\langle D|\,\hat{\mu}(D)\,|D^*\rangle\,\Big(\hat{e}_{\mathbf{k},\lambda}e^{i\mathbf{k}\cdot\mathbf{R_D}}\underbrace{\langle 1|\,\hat{a}_{\mathbf{k},\lambda}\,|0\rangle}_{\langle 1|0\rangle=0} - \hat{e}^{-}_{\mathbf{k},\lambda}e^{-i\mathbf{k}\cdot\mathbf{R_D}}\underbrace{\langle 1|\,\hat{a}^{\dagger}_{\mathbf{k},\lambda}\,|0\rangle}_{\langle 1|1\rangle=1}\Big) \\
&= i\sum_{\mathbf{k},\lambda}\left(\frac{\hbar ck}{2\epsilon_0 V}\right)^{1/2}\mu_i^{\text{full}}(D)\hat{e}^{-}_{i,\mathbf{k},\lambda}e^{-i\mathbf{k}\cdot\mathbf{R_D}}\,, \qquad\qquad (A.2)
\end{aligned}$$

where a following notation has been used

$$\mu^{\text{full}}(A) = \langle A^*|\,\hat{\mu}(A)\,|A\rangle\,, \qquad \mu^{\text{full}}(D) = \langle D|\,\hat{\mu}(D)\,|D^*\rangle\,. \qquad (A.3)$$

When the complete state vectors of $D$ and $A$ containing electronic and sublevels from equations 4.26 and 4.27 are inserted to the above equations

$$\mu^{\text{full}}(D) = \langle D_{\text{el}}| \hat{\mu}(D) |D^*_{\text{el}}\rangle \langle \varphi_D^{(r)} | \varphi_{D^*}^{(n)} \rangle = \mu_D \langle \varphi_D^{(r)} | \varphi_{D^*}^{(n)} \rangle \tag{A.4}$$

$$\mu^{\text{full}}(A) = \langle A^*_{\text{el}}| \hat{\mu}(A) |A_{\text{el}}\rangle \langle \varphi_{A^*}^{(p)} | \varphi_A^{(m)} \rangle = \mu_A \langle \varphi_{A^*}^{(p)} | \varphi_A^{(m)} \rangle \ , \tag{A.5}$$

where, the dipole operators are assumed not to depend on the vibrational degrees according to the Frank-Condon principle, $\mu_A$ and $\mu_D$ being the proper electronic parts of the transition matrix. The one photon states corresponding to value $q = 2$ are calculated in similar fashion, and they are

$$\langle F| H_{\text{int}} |M_2\rangle = -i \sum_{\mathbf{k},\lambda} \left( \frac{\hbar c k}{2\epsilon_0 V} \right)^{1/2} \mu_j^{\text{full}}(D) \hat{e}_{j,\mathbf{k},\lambda} e^{-i\mathbf{k}\cdot\mathbf{R_D}} \tag{A.6}$$

$$\langle M_2| H_{\text{int}} |I\rangle = i \sum_{\mathbf{k},\lambda} \left( \frac{\hbar c k}{2\epsilon_0 V} \right)^{1/2} \mu_i^{\text{full}}(A) \hat{e}^-_{i,\mathbf{k},\lambda} e^{i\mathbf{k}\cdot\mathbf{R_A}} \ . \tag{A.7}$$

When these one photon states are plugged back to the equation 4.31 we obtain

$$\langle F| V |I\rangle = \frac{1}{2V\epsilon_0} \sum_{\mathbf{k},\lambda} k \hat{e}^-_{i,\mathbf{k},\lambda} \hat{e}_{j,\mathbf{k},\lambda} \left( \frac{\mu_i^{\text{full}}(D) \mu_j^{\text{full}}(A) e^{i\mathbf{k}\cdot\mathbf{R}}}{K - k} + \frac{\mu_j^{\text{full}}(D) \mu_i^{\text{full}}(A) e^{-i\mathbf{k}\cdot\mathbf{R}}}{-K - k} \right) \ , \tag{A.8}$$

where $\mathbf{R} = \mathbf{R_A} - \mathbf{R_D}$ is the separation vector of A and D. The wave-vector and polarization summations can be calculated by the techniques developed in [65]. The wave-vector sum can be transformed into integral by extending the quantization volume

$$\frac{1}{V} \sum_{\mathbf{k}} \Rightarrow \int_V \frac{d^3\mathbf{k}}{(2\pi)^3} \, , \tag{A.9}$$

where $\int_V$ is shorthand notation for $\int_0^\infty \int_\Omega$. The polarization sum can be expressed as

$$\sum_{\lambda} \hat{e}_{i,\mathbf{k},\lambda} \hat{e}^-_{j,\mathbf{k},\lambda} = \delta_{ij} - \vec{k}_i \vec{k}_j \, , \tag{A.10}$$

where $\vec{k} = \mathbf{k}/k$ is the unit vector along $\mathbf{k}$. Now $\langle F|\, V\, |I\rangle$ can be written

$$\begin{aligned}\langle F|\, V\, |I\rangle &= \frac{\mu_i^{\text{full}}(D)\mu_j^{\text{full}}(A)}{16\pi^3\epsilon_0}\int_V k(\delta_{ij}-\vec{k}_i\vec{k}_j)\left(\frac{e^{i\mathbf{k}\cdot\mathbf{R}}}{K-k}+\frac{e^{-i\mathbf{k}\cdot\mathbf{R}}}{-K-k}\right)d^3\mathbf{k}\\ &= \frac{\mu_i^{\text{full}}(D)\mu_j^{\text{full}}(A)}{16\pi^3\epsilon_0}\int_0^\infty k(\delta_{ij}-\vec{k}_i\vec{k}_j)\int_\Omega\left(\frac{e^{i\mathbf{k}\cdot\mathbf{R}}}{K-k}+\frac{e^{-i\mathbf{k}\cdot\mathbf{R}}}{-K-k}\right)k^2 dk d\Omega\,.\end{aligned} \tag{A.11}$$

Using twice the relation

$$\frac{1}{k}\nabla_j\int_V e^{\pm i\mathbf{k}\cdot\mathbf{R}}d^3\mathbf{k} = \pm i\int_V \underbrace{\frac{\mathbf{k_j}}{k}}_{\vec{k}_j} e^{\pm i\mathbf{k}\cdot\mathbf{R}}d^3\mathbf{k}\,, \tag{A.12}$$

one obtains

$$\int_V \vec{k}_i\vec{k}_j e^{\pm i\mathbf{k}\cdot\mathbf{R}}d^3\mathbf{k} = -\frac{1}{k^2}\nabla_i\nabla_j\int_V e^{\pm i\mathbf{k}\cdot\mathbf{R}}d^3\mathbf{k}\,. \tag{A.13}$$

Now performing the angular integration yields and remembering that ($\mathbf{k}\cdot\mathbf{R} = kR\cos\theta$)

$$\int_0^{2\pi}\int_{-1}^{1} e^{\pm ikR\cos\theta}d(\cos\theta)d\phi = \frac{4\pi}{kR}\sin(kR) \tag{A.14}$$

gives

$$\langle F|\, V\, |I\rangle = \frac{\mu_i^{\text{full}}(D)\mu_j^{\text{full}}(A)}{4\pi^2\epsilon_0}(-\nabla^2\delta_{ij}+\nabla_i\nabla_j)G(K,R)\,, \tag{A.15}$$

where $G(K,R)$ is the Green's function

$$\begin{aligned}G(K,R) &= \int_0^\infty \frac{\sin(kR)}{R}\left(\frac{1}{K-k}+\frac{1}{-K-k}\right)dk\\ &= \int_{-\infty}^\infty \frac{e^{ikR}}{2iR}\left(\frac{1}{K-k}+\frac{1}{-K-k}\right)dk\,,\end{aligned} \tag{A.16}$$

which can be solved by residue theorem, as in [65, 70]. Calculation of the Green's function yields

$$G(K,R) = -\frac{\pi}{R}e^{iKR}\,. \tag{A.17}$$

Completing the vector calculus in A.15 results in an expression

$$\begin{aligned}\langle F|\, V\, |I\rangle &= \mu_i^{\text{full}}(D) V_{ij}(K,\mathbf{R}) \mu_j^{\text{full}}(A) \\ &= \mu_i^{\text{full}}(D)\mu_j^{\text{full}}(A)\frac{K^3 e^{iKR}}{4\pi\epsilon_0}\left[\left(\delta_{ij}-3\vec{R}_i\vec{R}_j\right)\left(\frac{1}{K^3R^3}-\frac{i}{K^2R^2}\right)-(\delta_{ij}-\vec{R}_i\vec{R}_j)\frac{1}{KR}\right].\end{aligned} \tag{A.18}$$

# References


[1] A.M. Humphrey. *Chlorophyll.* Food Chemistry, Vol. 5, Issue 1, pp. 57-67, 1980.

[2] B. Grimm, R. J. Porra, W. Rüdiger and H. Scheer. *Chlorophylls and Bacteriochlorophylls.* Netherlands, Springer, 2006.

[3] T. Markvart and L. Castañer. *Practical Handbook of Photovoltaics: Fundamentals and Applications.* United Kingdom, Elsevier, 2003.

[4] W. S. Steed and J. L. Atwood. *Supramolecular Chemistry.* United Kingdom, Wiley, 2000.

[5] B. O'Regan and M. Grätzel. *A low-cost, high-efficiency solar cell based on dye-sensitized colloidal TiO2 films.* Nature, Vol. 353, pp. 737-740, 1991.

[6] P. Bhattacharya. *Semiconductor Optoelectronic Devices.* United States, Prentice-Hall Inc., 2nd. Edition, 1997.

[7] I. L. Medintz, A. R. Clapp, H. Mattoussi, E. L. Goldman, B. Fisher and J. M. Mauro. *Self-assembled nanoscale biosensors based on quantum dot FRET donors.* Nature, Vol. 2, pp. 630-638, 2003.

[8] M. Achermann, M. A. Petruska, S. Kos, D. L. Smith, D. D. Koleske and V. Klimov. *Energy-Transfer pumping of nanocrystals using an epitaxial quantum well.* Nature, Vol. 429, pp. 642-646, 2004.

[9] P. Atkins and J. de Paula. *Atkins' Physical Chemistry.* United Kingdom, Oxford University Press, 8th. Edition 2006.

[10] A. Sharma and S. G. Schulman. *Introduction to fluorescence spectroscopy.* United States, Wiley, 1999.

[11] J. M. Hollas. *Modern Spectroscopy.* United Kingdom, Wiley, 4th. Edition, 2003.

[12] B. Valeur. *Molecular Fluorescence - Principles and Applications.* Germany, Wiley, 2002.

[13] W. Schnabel. *Polymers and light.* Germany, Wiley, 2007.

[14] M. Warren and A. Smith. *Tetrapyrroles: Birth, Life and Death.* United Kingdom, Springer, 2009.

[15] F. Salisbury and C. Ross. *Plant Physiology.* United Kingdom, Brooks Cole, 4th. Edition, 1991.

[16] H. Scheer, *Chlorophylls.* CRC Press, Boca Raton, 1991

[17] J. Deisenhofer, O. Epp, K. Miki, R. Huber and H. Michel. *Structure of the protein subunits in the photosynthetic reaction centre of Rhodopseudomonas viridis at 3 Å resolution.* Nature, Vol. 318, pp. 618-624, 1985.

[18] J. Helaja, K. Hyvärinen, S. Heikkinen, I. Kilpelainen and P. H. Hynninen. *Solution structures of 132-methoxychlorophyll a epimers.* Journal of Molecular Structure, Vol. 354, Issue 1, pp. 71,74-75,78, 1995.

[19] J. Helaja, A. Y. Tauber, I. Kilpeläinen and P. H. Hynninen. *Novel Model Compounds for Photoinduced Electron Transfer; Structures of the Folded Conformers of Zinc(II)-Pyropheophytin-Anthraquinone Dyads.* Magnetic Resonance in Chemistry, Vol. 35, pp. 619-628, 1997.

[20] L. P. Vernon and G. R. Seely. *The Chlorophylls.* New York, Academic Press, 1966.

[21] C. B. Storm and Y. Teklu. *Nitrogen-hydrogen tautomerism in porphyrines and chlorines.* Journal of American Chemical Society, Vol. 94, Issue 5, pp. 1745-1747, 1972.

[22] J. Jusélius and D. Sundholm. *The aromatic pathways of porphins, chlorins and bacteriochlorins*. Physical Chemistry Chemical Physics, Vol. 2, pp. 2145-2151, 2000.

[23] M. Gouterman. *Spectra of porphyrins.* Journal of Molecular Spectroscopy, Vol. 6, pp. 138-163, 1961.

[24] M. Gouterman. *Spectra of porphyrins: Part III. Self-consistent molecular orbital calculations of porphyrin and related ring systems.* Journal of Molecular Spectroscopy, Vol. 16, Issue 2, pp. 415-450, 1965.

[25] D. Sundholm. *Density functional theory calculations of the visible spectrum of chlorophyll a.* Chemical Physics Letters, Vol. 302, Issues 5-6, pp. 480-484, 1999.

[26] J. Hasegawa, Y. Ozeki, K. Ohkawa, M. Hada and H. Nakatsuji. *Theoretical Study of the Excited States of Chlorin, Bacteriochlorin, Pheophytin a, and Chlorophyll a by the SAC/SAC-CI Method.* The Journal of Physical Chemistry B, Vol. 102 (7), pp. 1320-1326, 1998.

[27] L. R. Milgrom. *The Colours of Life: An Introduction to the Chemistry of Porphyrins and Related Compounds.* United Staes, Oxford University Press, 1997.

[28] D. Dolphin. *The Porphyrins III, Physical Chemistry, Part A.* New York, Academic Press, 1978.

[29] D. Vavilin, H. Xu, S. Lin and W. Vermaas. *Energy and electron transfer in photosystem II of a chlorophyll b-containing Synechocystis sp. PCC 6803 mutant.*. Biochemistry, Vol. 42, pp. 1731-1746, 2003.

[30] H. Tamiaki, T. Miyatake, R. Tanikaga, A. R. Holzwarth and K. Schaffner. *Self-Assembly of an Artificial Light-Harvesting Antenna: Energy Transfer from a Zinc Chlorin to a Bacteriochlorin in a Supramolecular Aggregate.* Angewandte Chemie International, Vol. 35, Issue 7, pp. 772-774, 2003.

[31] R. Blankenship, M. T. Madigan and C. E. Bauer. *Anoxygenic Photosynthetic Bacteria.* Dordrecht, Kluwer Academic Publishers, 1995.

[32] G. Blauer and H. Sund. *Optical Properties and Structure of Tetrapyrrols.* London, De Gruyter, 1985.

[33] J. P. Allen, G. Feher, T. O. Yeates, H. Komiya and D. C. Rees. *Structure of the reaction center from Rhodobacter sphaeroides R-26: The protein subunits.* PNAS, Vol. 84, pp. 6162-6166, 1987.

[34] A. W.D. Larkum and M. Kühl. *Chlorophyll d: the puzzle resolved.* Trends in Plant Science, Vol. 10, Issue 8, pp. 355-357, 2005.

[35] S. S. Brody and E. Rabinowitch. *Excitation Lifetime of Photosynthetic Pigments in vitro and in vivo.* Science, Vol. 125, pp. 555-557, 1957.

[36] H. Van Amerongen, L. Valkunas and R. Van Grondelle. *Photosynthetic Excitons.* Singapore, World Scientific Publishing, 2000.

[37] K. N. Solovyov and E. A. Borisevich. *Intramolecular heavy-atom effect in the photophysics of organic molecules.* Physics-Uspekhi, Vol. 48 (3), pp. 231-253, 2005.

[38] L. L. Shipman, J. R. Norris and J. J. Katz. *Quantum mechanical formalism for computation of the electronic spectral properties of chlorophyll aggregates.* Journal of Phyrical Chemistry, Vol. 80, pp. 877-882, 1976.

[39] G. C. Papageorgiou and R. Van Govindjee. *Chlorophyll a Fluorescence.* Netherlands, Springer, 2004.

[40] J. C. de Paula, J. H. Robblee and R. F. Pasternacka. *Aggregation of chlorophyll a probed by resonance light scattering spectroscopy.* Biophysical Journal, Vol. 68, Issue 1, pp. 335-341, 1995.

[41] T. S. Balaban, H. Tamiaki, A. R. Holzwarth. *Chlorins Programmed for Self-Assembly.* Topics in Current Chemistry, Vol. 258, pp. 1-38, 2005.

[42] V. Huber, S. Sengupta and F. Würhner. *Structure-Property Relationships for Self-Assembled Zinc Chlorin Light-Harvesting Dye Aggregates.* Chemistry - A European Journal, Vol. 14, Issue 26, pp. 7791-7807, 2008.

[43] J. Standfuss, A. C. Terwisscha van Scheltinga, M. Lamborghini and W. Kühlbrandt. *Mechanisms of photoprotection and nonphotochemical quenching in pea lightharvesting complex at 2.5 Å resolution.* European Molecular Biology Organization (EMBO) Journal, Vol. 24, pp. 919-928, 2005.

[44] J. Matysik, C. Soede-Huijbregts, M. Baldus, J. Raap, J. Lugtenburg, P. Gast, H. J.. van Gorkom, A. J. Hoff and H. J. M. de Groot. *Ultrahigh Field MAS*

*NMR Dipolar Correlation Spectroscopy of the Histidine Residues in Light-Harvesting Complex II from Photosynthetic Bacteria Reveals Partial Internal Charge Transfer in the B850/His Complex.* Journal of American Chemical Society, Vol. 123, Issue 20, pp. 4803-4809, 2001.

[45] H. Kirchoff. H.-J. Hinz and J. Rösgen. *Aggregation and fluorescence quenching of chlorophyll a of the light-harvesting complex II from spinach in vitro.* Biochimica et Biophysica Acta (BBA) - Bioenergetics, Vol. 1606, Issues 1-3, pp. 105-116, 2003.

[46] T. S. Balaban, J. Leitich, A. R. Holzwarth and K. Schaffner. *Autocatalyzed Self-Aggregation of ($3^1R$)-[Et,Et]Bacteriochlorophyll $c_F$ Molecules in Nonpolar Solvents. Analysis of the Kinetics.* Journal of Physical Chemistry B, Vol. 104, pp. 1362-1372, 2000.

[47] A. S. Davydov. *The theory of molecular excitons.* Soviet Physics Uspekhi, Vol. 82, pp. 393-448, 1964.

[48] M. Kasha, H. R. Rawls and M. A. El-Bayoumi. *The exciton model in molecular spectroscopy.* Pure and Applied Chemistry, Vol. 11, No. 3-4, pp. 371-392, 1965.

[49] D. Möbius. *Scheibe aggregates.* Advanced Materials, Vol. 7, Issue 5, pp. 437-444, 1995.

[50] F. Perrin. *Théorie quantique des transferts d'activation entre molécules de même espèce. Cas des solutions fluorescentes.* Ann. Phys., Vol. 17, pp. 283-314, 1932.

[51] T. Förster. *Energiewanderung und Fluoreszenz (Energy transfer and fluorescence).* Naturwissenschaffen, Vol. 6, pp. 166-175, 1946.

[52] T. Förster. *Zwischenmolekulare Energiewanderung und Fluoreszenz (Intermolecular energy migration and fluorescence).* Ann. Phys., Vol. 2, pp. 55-75, 1948.

[53] T. Förster. *Experimentelle und theoretische Untersuchung des zwischenmolekularen Übergangs von Elektronenanregunngsenergie (Experimental and theoretical study of the intermolecular transfer of excitation energy).* Z. Naturforsch, Vol. 4A, pp. 321-327, 1949.

[54] Y. P. Ho, H. H. Chen, K. W. Leong and T-H. Wang. *Evaluating the intracellular stability and unpacking of DNA nanocomplexes by quantum dots-FRET.* Journal of Controlled Release, Vol. 116, Issue 1, pp. 83-89, 2006.

[55] B. Tang, L. Cao, K. Xu, L. Zhuo, J. Ge, Q. Li and L. Yu. *A New Nanobiosensor for Glucose with High Sensitivity and Selectivity in Serum Based on Fluorescence Resonance Energy Transfer (FRET) between CdTe Quantum Dots and Au Nanoparticles.* Chemistry - A European Journal, Vol. 14, Issue 12, pp. 3637-3644, 2008.

[56] P. I. Bastiaens and T. M. Jovin. *Microspectroscopic imaging tracks the intracellular processing of a signal transduction protein: fluorescent-labeled protein kinase C beta I.* PNAS, Vol. 93, no. 16, pp. 8407-8412, 1996.

[57] C. S. Yun, A. Yavier, T. Jennings, M. Fisher, S. Hira, S. Peterson B. Hopkins, N. O. Reich, and G. F. Strouse. *Nanometal Surface Energy Transfer in Optical Rulers, Breaking the FRET Barrier.* Journal of American Chemical Society, Vol. 127, pp. 3115-3119, 2005.

[58] T. Franzl, T. A. Klar, S. Schietinger, A. L. Rogach and J. Feldmann. *Exciton Recycling in Graded Gap Nanocrystal Structures.* Nano Letters, Vol. 4, pp. 1599-1603, 2004.

[59] D. L. Andrews and A. A. Demidov. *Resonance Energy Transfer.* United Kingdom, Wiley, 1999.

[60] P. G. Wu and L. Brand. *Resonance Energy Transfer: Methods and Applications.* Analytical Biochemistry, Vol. 218, no. 1, pp. 1-13, 1994.

[61] T. Förster. *Fluoreszenz organischer Verbindungen (Fluorescence of organic compounds).* Göttingen: Vandenhoeck & Ruprecht, pp. 312, 1951.

[62] L. Novotny and B. Hecht. *Principles of Nano-Optics.* United Kingdom, Cambridge University Press, 2006.

[63] R. M. Clegg. *Fluorescence resonance energy transfer.* Current Opinion in Biotechnology, Vol. 6, Issue 1, pp. 103-110, 1995.

[64] B. W. Van Der Meer, G. I. Coker and S.-Y. Chen. *Resonance Energy Transfer, Theory and Data.* New York, Wiley, 1994.

[65] D. P. Craig and T. Thirunamachandran. *Molecular Quantum Electrodynamics.* United Kingdom, Dover Publications, 1998.

[66] F. Schwabl. *Quantum Mechanics.* The Netherlands, Springer, 3rd. Edition, 2002.

[67] A. Salam. *A General Formula for the Rate of Resonant Transfer of Energy Between two Electric Multipole Moments of Arbitrary Order Using Molecular Quantum Electrodynamics.* Journal of Chemical Physics, Vol. 122, 044112, 2005.

[68] D. L. Andrews and J. M. Leeder. *Resonance Energy Transfer: When a Dipole Fails.* Journal of Chemical Physics, Vol. 130, 184504, 2009.

[69] F. Schwabl. *Advanced Quantum Mechanics.* Germany, Springer, 2nd. Edition, 2000.

[70] G. J. Daniels, R. D. Jenkins, D. S. Bradshaw and D. L. Andrews. *Resonance Energy Transfer: The Unified Theory Revisited.* Journal of Chemical Physics, Vol. 119, Number 4, 2003.

[71] M. D. Galaninin. *Luminescence of molecules and crystals.* United Kingdom, Cambridge International Science Publishing, 1996.

[72] R. E. Dale, J. Eisinger and W. E. Blumberg. *The orientational freedom of molecular probes. The orientation factor in intramolecular energy transfer.* Biophysical Journal, Vol. 26, pp.161-193, 1979.

[73] D. A. Allwood, R. T. Carlineb, N. J. Masona, C. Pickeringb, B. K. Tannerc and P. J. Walkera. *Characterization of oxide layers on GaAs substrates.* Thin Solid Films, Vol. 364, Issues 1-2, pp. 33-39, 2000.

[74] C. J. Sandroff, R. N. Nottenburg. J.-C. Bischoff and R. Bhat. *Dramatic enhancement in the gain of a GaAs/AlGaAs heterostructure bipolar transistor by surface chemical passivation.* Applied Physics Letters, Vol. 51, Issue 1, pp. 33-35, 1987.

[75] V. Bessolova, M. Lebedeva, A. Ivankovb, W. Bauhoferb and D. Zahnc. *Electronic properties of GaAs(100) surface passivated in alcoholic sulfide solutions.* Applied Surface Science, Vol. 133, Issues 1-2, pp. 17-22, 1998.

[76] A. Dreas-Wlodarczak, M. Müllneritsch, T. Juffmann, C. Cioffi, M. Arndt and M. Mayor. *Immobilization of Zinc Porphyrin Complexes on Pyridine-Functionalized Glass Surfaces.* Langmuir, Vol. 26 (13), pp. 10822-10826, 2010.

[77] J. J. Dubowski, R. Voznyy and G. M. Mashall. *Molecular self-assembly and passivation of GaAs (0 0 1) with alkanethiol monolayers: A view towards biofunctionalization.* Applied Surface Science, Vol. 256, Issue 19, pp. 5714-5721, 2010.

[78] D. K. Schoder. *Semiconductor Material and Device Characterization.* New Jersey, Wiley, 3rd. Edition, 2006.

[79] S. Balslev, A. Mironov, D. Nilsson and A. Kristensen. *Micro-fabricated single mode polymer dye laser.* Optics Express, Vol. 4, Issue 6, pp. 2170-2177, 2006.

[80] T. Voss, D. Scheel and W. Schade. *A microchip-laser-pumped DFB-polymer-dye laser.* Applied Physics B: Lasers and Optics, Vol. 73, Number 2, pp. 105-109, 2001.